IPP-Report

IPP Max-Planck-Institut für Plasmaphysik

Simon Pinches

Nonlinear Interaction of Fast Particles with Alfvén Waves in Tokamaks

IPP 5/81
August 1998

Nonlinear Interaction of Fast Particles with Alfvén Waves in Tokamaks

Simon David Pinches, B.Sc.

Thesis submitted to the University of Nottingham for
the degree of Doctor of Philosophy, November 1996.

To the memory of my father

Roy Samuel Pinches

1942 – 1984

v. 3.1

Contents

List of Figures

List of Tables

Abstract

Concern surrounds Alfvén instabilities driven by super-Alfvénic fusion-born α-particles and their possible consequences for α-particle transport in fusion tokamak reactors. This has motivated work upon the self-consistent calculation of the power transfer from a highly energetic α-particle population to Alfvén waves and the ensuing nonlinear wave evolution.

A Monte-Carlo approach has been developed which allows fast ions to be studied in the presence of low-frequency ($\omega \ll \omega_{ci}$) electromagnetic perturbations in a toroidal plasma. Fast particle motion is treated using a guiding centre Hamiltonian description in straight magnetic field line coordinates. The electromagnetic field is modelled as the superposition of an axisymmetric magnetic field and a spectrum of time dependent Alfvén Eigenmodes (AE), with the perturbed fields accorded two degrees of freedom corresponding to their amplitudes and phase shifts.

The model accounts for nonlinear wave-particle interactions but ignores MHD fluid nonlinearities which are small for typical AE amplitudes. Hence both the spatial structure and eigenfrequencies of the AEs are taken directly from linear MHD eigenfunctions.

Numerical noise in the system is reduced by considering only those 'particles' present in the system that constitute the change in the fast particle distribution function, this being the so-called δf technique. Such an approach allows studies to be focused upon an accurate description of those resonant particles which provide a transfer of fast-ion free energy to the unstable AE. The growth in AE amplitude eventually leads to a modification of resonant α-particle orbits and ultimately to the wave itself saturating.

Results identify mechanisms of α-particle redistribution and loss in the presence of fixed and self-consistently varying amplitude AEs in large tokamaks such as JET and ITER.

The Author

The author was born on the 20th February 1972 in Barnstaple, (England), and was educated at Monkwearmouth College, Sunderland and Oxclose Community School, Washington. He gained a first class honours degree in Mathematical Physics from the University of Manchester Institute of Science and Technology in 1993 and has accepted a research post at the Max-Planck-Institut für Plasmaphysik in Garching, Munich.

Acknowledgements

I am indebted to a great number of people for help and advice throughout my time as a PhD student. I especially thank my supervisor Keith Hopcraft for providing guidance and support whenever required and Sergei Sharapov for acting beyond the call of duty to help fill the numerous gaps in my knowledge. I thank Jeff Candy for always making time to answer my questions and for doing so with efficiency and clarity. I express my gratitude to Tim Hender, my external supervisor at Culham and Wolfgang Kerner. As well as to Lynton Appel, Duarte Borba, Richard Buttery, Guido Huysmans and my numerous other colleagues at Culham Laboratory and JET, for providing help and advice on many subjects including fast particles and Alfvén waves.

I express my gratitude to my parents, for without whom (as the cliché goes) none of this would have been possible, as well as to my fiancée Veronica for enduring all stages of this thesis!

Finally, I gratefully acknowledge financial assistance from UKAEA Fusion and JET without which I wouldn't have been able to undertake this most enjoyable stage in my life.

Chapter 1

Introduction

1.1 General Introduction

The controlled nuclear fusion of hydrogen isotopes in a plasma promises a practically inexhaustible source of energy and high environmental safety as compared to nuclear fission. However, in order to reach the 'ignition' conditions (when the fusion born particles heat the plasma and compensate for the heat losses) even for the most favourable fusion reaction between deuterium and tritium

$$\mathrm{D} + \mathrm{T} \longrightarrow {}^4\mathrm{He} + \mathrm{n} + 17.6\ \mathrm{MeV}, \tag{1.1}$$

the D-T plasma must be heated to a temperature of $T \geq 20$ keV (230 million K) and must be confined for long enough to satisfy the Lawson criterion [1]:

$$n\tau_E > 1.5 \times 10^{20} \mathrm{m}^{-3}\mathrm{s},$$

where τ_E is the energy confinement time, the ratio of the energy stored in the plasma to the heat loss rate, and n is the D-T fuel density.

The most advanced approach towards the achievement of the relevant fusion reactor parameters is the confinement of a plasma within a magnetic field in a so-called tokamak[1] configuration [2, 3] as shown in Fig. 1.1. The tokamak is an axisymmetric toroidal device characterized by a large magnetic field in the toroidal direction and a smaller poloidal field. The toroidal field is produced by large external field coils and the poloidal field by a large toroidal current in the plasma. The latter current is induced by a transformer, with the plasma forming the secondary winding.

To reach the ignition conditions described above the tokamak plasma is heated by the ohmic dissipation of the induced current and by additional heating schemes such as the injection of high energy neutral beams, or by launching electromagnetic waves into

[1] From the Russian toroidalnaya kamera s magnitnym polem (toroidal chamber with magnetic field).

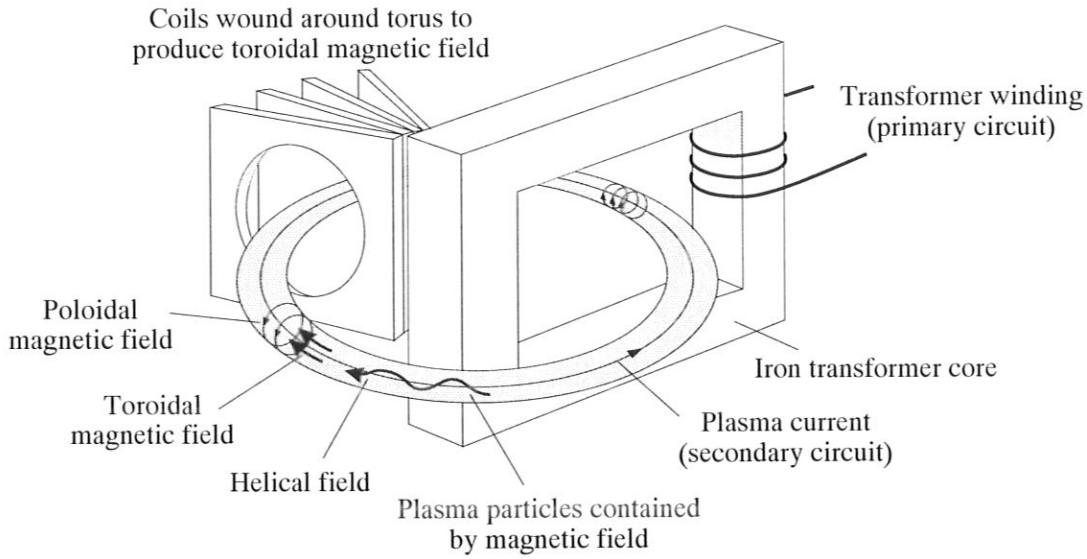

Figure 1.1: Schematic drawing of a tokamak.

the plasma [3]. Once ignited the plasma is intended to become entirely self-heating through the fusion-born α-particles (He^4 nuclei of energy 3.52 MeV). The transport properties of these highly energetic α-particles is therefore of crucial importance since they will determine the plasma heating profiles, the plasma dilution due to the 'helium ash' accumulation and the power loading upon the first wall in an ignited tokamak-reactor.

During the α-particle slowing-down time the classical cross-field transport of α-particles is generally negligible. However, significant anomalous transport and losses of supra-thermal particles may take place in the presence of Alfvén waves which resonate with them [4, 5]. For typical tokamak-reactor parameters (density $n \sim 10^{20}$ m^{-3}, magnetic field $B \sim 6$ T) of particular importance are weakly-damped Toroidal Alfvén Eigenmodes (TAE) [6, 7] with phase velocities of the order of the α-particle speeds before thermalisation.

Experiments with neutral beam injection (NBI) on tokamaks DIII-D [8] and TFTR [9] and experiments with α-particles in D-T plasmas [10] have shown that weakly damped TAE can indeed be driven by fast particles and that under certain conditions Alfvén instabilities can cause a significant loss of those particles [11, 12] causing problems for the first wall [12].

The Alfvén wave [13] describes a basic oscillation between perpendicular plasma kinetic energy and perpendicular 'line bending' magnetic energy and is analogous to the familiar case of waves travelling along a taut string. These waves propagate along

the magnetic field lines at the Alfvén speed,

$$v_A = \frac{B}{\sqrt{\mu_0 \rho}},$$

where ρ is the plasma mass density and B the magnetic field strength. Due to their relatively high phase velocity, $v_A \sim 5 \times 10^6$ m/s, Alfvén waves mainly resonate with highly energetic particles. To analyse this resonant wave-particle interaction in a fusion reactor it is appropriate to decompose the total particle distribution into two parts: A thermal (generally non-Maxwellian) background component forming the bulk of the plasma, and a smaller, but more energetic, super-Alfvénic distribution of hot α-particles. The collective motion of the low energy background component which is frozen in the magnetic field is suitably described by the well developed magnetohydrodynamic (MHD) approach, but this is not the case for the energetic particles whose motion is decoupled from the magnetic field lines. Their dynamics are best described using the guiding centre approach in which their rapid gyration and resulting helical path is approximated by a smooth drifting trajectory.

The unperturbed magnetic field structure is responsible for determining both the particle orbits and the spatial structure of the Alfvén eigenmodes (AE) that the system can support. Consequently the careful choice of coordinate system is of crucial importance for simplifying the problem, since a suitable choice allows both the field structure itself and the particle motion to be easily described. The total field structure will be represented as the superposition of an axisymmetric equilibrium magnetic field generated from a consideration of force balance, and a small electromagnetic perturbation representing the AE. The spatial structure of the AE is found from an MHD description of the waves that the thermal background plasma and equilibrium field can support. In toroidal geometry due to the periodicity in the poloidal and toroidal directions each eigenmode can be naturally decomposed into Fourier components with each of the distinct AE allowed two degrees of freedom: amplitude and phase-shift. The radial structure of the AE present is assumed invariant since it is determined by the background plasma distribution and equilibrium field parameters which remain unperturbed. The evolution equations for each AE are derived from a Lagrangian formulation in which the full wave-particle interactions are included whilst wave-wave nonlinearities are ignored in accordance with previous findings [14].

It is apparent that the problem that this thesis addresses, namely that of studying the interaction of fast particles with Alfvén eigenmodes, is in general nonlinear, since both the waves and particles evolve in response to the collective motion of the other, necessitating a self-consistent treatment. To enable the problem to become mathematically and computationally tractable several simplifying assumptions have been made, consistent with the underlying physical processes. The equations governing the evolution of the system that results from these assumptions can be set up in the form of a Monte-Carlo model. Recent developments [15, 16] have suggested an enhanced algorithm for performing such simulations that has come to be known as the δf method. This method produces superior results without the need to use excessive numbers of

Monte-Carlo points by only modelling the change in the particle distribution function rather than the whole ensemble. The inclusion of the δf technique into the model suggests many other potential developments such as the inclusion of an energetic ion source and sink and also possibly a complete treatment of the energetic ion collisional evolution in terms of the Fokker-Planck equation [17, 18].

The goal of this thesis is to develop a self-consistent δf model and to apply it to study a particular class of kinetic instabilities of Toroidal Alfvén Eigenmodes (TAE) that exist in toroidal geometry and may be excited by energetic particles. Due to the high α-particle pressure in future machines such as the proposed International Thermonuclear Experimental Reactor (ITER), it is feared that TAE could grow to amplitudes sufficient to cause an anomalous radial transport/losses of energetic particles. Estimates for ITER indicate that α-particle losses greater than 5% being repeated from shot to shot may be sufficient to cause damage to the first wall, whilst higher losses may even lead to the quench of ignition [19]. In this thesis the effect of various fast particle distributions upon the growth rates and saturation amplitudes of AE instabilities are demonstrated for a number of experimental conditions in large tokamaks.

The thesis is organised as follows: Chapter 2 presents a review of the MHD model for AE and describes particle motion in a tokamak. Chapter 3 begins by introducing the specific coordinate system defined by the magnetic field structure that is used in the model before deriving the dynamical equations governing the fast particle motion and the wave evolution. It closes with a presentation of the novel δf scheme employed in the model. Chapter 4 describes the details concerning the model's computational implementation and subsequent validation. Chapter 5 presents and discusses the results of applying the model to the AE problem in tokamaks. Conclusions are drawn in Chapter 6 with indications for further work.

Chapter 2

Theoretical Review

2.1 MHD Description of Alfvén Eigenmodes

One of the most useful models for describing plasma behaviour is that formed by taking velocity moments of the kinetic equation for ion and electron distribution functions. It respects the main physical conservation laws and permits analysis in the complicated magnetic configurations required for the confinement of plasmas. The moment equations have a form similar to the equations which describe the behaviour of a conducting fluid immersed in a magnetic field, consequently the moment approach in plasma studies is known as the magnetohydrodynamic (MHD) approach. By only considering scale lengths greater than the Debye length, a plasma may be considered quasi-neutral with $n_e = Zn_i$. In the approximation of infinite plasma conductivity the moment equations take the following form of 'ideal MHD':

$$\left.\begin{aligned} \frac{\partial \rho}{\partial t} + \nabla \cdot (\rho \mathbf{v}) &= 0 \quad \text{(Mass continuity)} \\ \rho \frac{\partial \mathbf{v}}{\partial t} + \rho \mathbf{v} \cdot \nabla \mathbf{v} + \nabla P - \mathbf{j} \wedge \mathbf{B} &= 0 \quad \text{(Momentum balance)} \\ \frac{\partial P}{\partial t} + \mathbf{v} \cdot \nabla P + \gamma P \nabla \cdot \mathbf{v} &= 0 \quad \text{(Adiabatic equation of state)} \\ \mathbf{E} + \mathbf{v} \wedge \mathbf{B} &= 0 \quad \text{(Ohm's Law)} \end{aligned}\right\} \text{Moment equations}$$

$$\left.\begin{aligned} \nabla \cdot \mathbf{B} &= 0 \quad \text{(No magnetic monopoles)} \\ \nabla \wedge \mathbf{B} - \mu_0 \mathbf{j} &= 0 \quad \text{(Ampère's Law)} \\ \frac{\partial \mathbf{B}}{\partial t} + \nabla \wedge \mathbf{E} &= 0 \quad \text{(Faraday's Law)} \end{aligned}\right\} \text{(Pre-) Maxwell's equations}$$

where ρ is the mass density of the plasma, $\mathbf{j}$ is the current density, $\mathbf{v}$ is the plasma velocity, P is the plasma pressure and γ is the adiabaticity index. The electric and magnetic fields, $\mathbf{E}$ and $\mathbf{B}$, that appear in these expressions consist of the externally applied fields and the averaged internal fields arising from long-range inter-particle interactions.

An important consequence of ideal MHD is that the plasma fluid is 'frozen' to the magnetic field lines. Consequently, it follows that the plasma motion is intricately linked to the magnetic field configuration and that a simple field description is tantamount to obtaining a simple description of the plasma motion.

The MHD model is usually applied to three problems: determining a realistic equilibrium configuration, investigating the stability of that equilibrium, and examining the different waves which the equilibrium can support. The last two of these are closely linked and are necessary for practical purposes such as examining methods of plasma heating and diagnosing the plasma by launching waves which aid the understanding of observed plasma instabilities.

2.1.1 Stability and Waves

Normal Mode Approach

The equations of ideal MHD are nonlinear but can be made more amenable to analysis in the first instance by linearizing them to identify classes of waves and instabilities. The justification for linearising is the observation that the bulk plasma remains essentially static whilst experiencing only small magnitude perturbations when examined over timescales that are long compared with those associated with the small scale dynamics. All quantities can thus be written as the sum of an equilibrium time-independent term and a small first-order time-dependent perturbation:

$$Q(\mathbf{r},t) = Q_0(\mathbf{r}) + \tilde{Q}_1(\mathbf{r},t)$$

Higher order terms describing the perturbations are neglected since $\tilde{Q}_1/Q_0 \ll 1$. Neglecting plasma motion by assuming that $\mathbf{v}_0 = 0$ the linearized equations of ideal MHD become:

$$\frac{\partial \rho_1}{\partial t} + \nabla \cdot (\rho_0 \mathbf{v}_1) = 0 \tag{2.1a}$$

$$\rho_0 \frac{\partial \mathbf{v}_1}{\partial t} + \nabla P_1 - \mathbf{j}_1 \wedge \mathbf{B}_0 - \mathbf{j}_0 \wedge \mathbf{B}_1 = 0 \tag{2.1b}$$

$$\frac{\partial P_1}{\partial t} + \mathbf{v}_1 \cdot \nabla P_0 + \gamma P_0 \nabla \cdot \mathbf{v}_1 = 0 \tag{2.1c}$$

$$\nabla \cdot \mathbf{B}_1 = 0 \tag{2.1d}$$

$$\frac{\partial \mathbf{B}_1}{\partial t} + \nabla \wedge \mathbf{E}_1 = 0 \tag{2.1e}$$

$$\nabla \wedge \mathbf{B}_1 - \mu_0 \mathbf{j}_1 = 0 \tag{2.1f}$$

$$\mathbf{E}_1 + \mathbf{v}_1 \wedge \mathbf{B}_0 = 0 \tag{2.1g}$$

Introducing the fluid displacement vector $\boldsymbol{\xi}(\mathbf{r},t)$ such that

$$\mathbf{v}_1 = \frac{\partial \boldsymbol{\xi}}{\partial t} \tag{2.2}$$

and eliminating $\mathbf{j}_1$ and $\mathbf{E}_1$ from equations (2.1) leads to the condensed set of equations:

$$\rho_0 \frac{\partial^2 \boldsymbol{\xi}}{\partial t^2} + \nabla P_1 + \frac{1}{\mu_0}(\mathbf{B}_1 \wedge (\nabla \wedge \mathbf{B}_0) + \mathbf{B}_0 \wedge (\nabla \wedge \mathbf{B}_1)) = 0$$
$$P_1 + \boldsymbol{\xi} \cdot \nabla P_0 + \gamma P_0 \nabla \cdot \boldsymbol{\xi} = 0$$
$$\mathbf{B}_1 + \nabla \wedge (\mathbf{B}_0 \wedge \boldsymbol{\xi}) = 0$$

The first of these equations is the linearized momentum balance equation, which upon using the other two equations to eliminate P_1 and $\mathbf{B}_1$, reduces to the force-operator equation of linearized MHD:

$$\rho_0 \frac{\partial^2 \boldsymbol{\xi}}{\partial t^2} = \mathbf{F}(\boldsymbol{\xi}), \tag{2.3}$$

with,

$$\mathbf{F}(\boldsymbol{\xi}) \equiv \nabla(\boldsymbol{\xi}\cdot\nabla P_0 + \gamma P_0 \nabla\cdot\boldsymbol{\xi}) + \frac{1}{\mu_0}\left[(\nabla \wedge \nabla \wedge (\boldsymbol{\xi} \wedge \mathbf{B}_0)) \wedge \mathbf{B}_0 + (\nabla \wedge \mathbf{B}_0) \wedge (\nabla \wedge (\boldsymbol{\xi} \wedge \mathbf{B}_0))\right].$$

One approach in studying linear stability and waves is to reformulate equation (2.3) as a normal mode problem. In this case the time variation of all the perturbed quantities is taken to be of the form $\tilde{Q}(\mathbf{r}, t) = Q(\mathbf{r})e^{-i\omega t}$ representing disturbances that have always been present and not requiring any initial conditions. With this formulation solutions of equation (2.3) can be written as

$$-\omega^2 \boldsymbol{\xi} = \frac{1}{\rho_0}\mathbf{F}(\boldsymbol{\xi}) \tag{2.4}$$

with $\boldsymbol{\xi}$ no longer an explicit function of time. Equation (2.4) together with appropriate boundary conditions on $\boldsymbol{\xi}$ represents an eigenvalue problem for the eigenvalue ω^2.

The force-operator $\mathbf{F}(\boldsymbol{\xi})$ is self-adjoint, or Hermitian [20], and as a consequence the eigenvalues of ω^2 are real, so that the spectrum of the operator $\rho_0^{-1}\mathbf{F}$ considered in the complex ω-plane is confined to the real and imaginary axes. This is important since it implies that within the ideal MHD model either exponentially growing modes ($\omega^2 < 0$) or oscillatory waves ($\omega^2 > 0$) are obtained as indicated in Fig. 2.1. A further

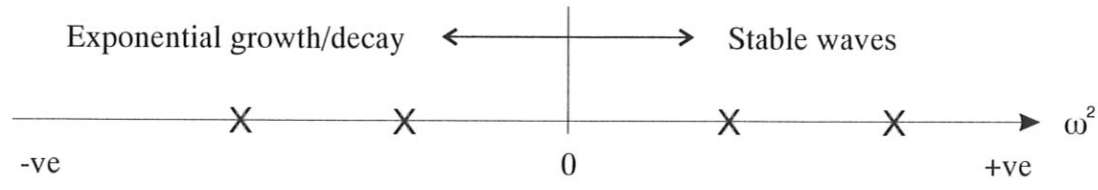

Figure 2.1: Spectrum of frequency eigenvalues ω^2 in ideal MHD

consequence of the operator $\rho_0^{-1}\mathbf{F}$ being Hermitian is that the discrete modes present are orthogonal and can therefore be used as a set of basis functions to describe any small

disturbance in a perturbative approach. The addition of a fast particle distribution upon a steady-state background plasma may perturb the stable eigenvalues of the system so that weakly growing or decaying oscillatory waves are obtained as illustrated in Fig. 2.2.

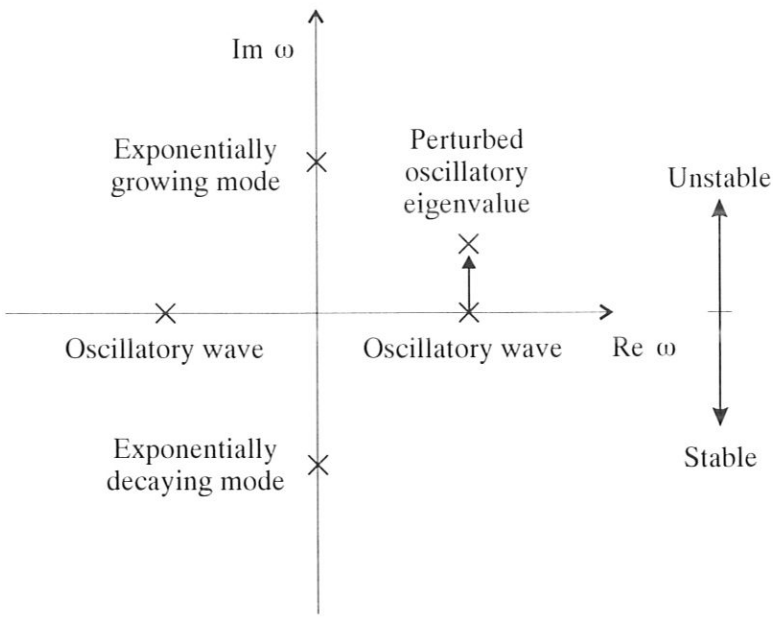

Figure 2.2: Spectrum of frequency eigenvalues in the presence of a fast particle distribution

2.1.2 Homogeneous Plasma

In this section the waves that occur in a infinite, homogeneous, and stationary slab of plasma are analysed. Since the equilibrium quantities are constant, it is helpful to Fourier transform the force operator equation (2.3) in both space and time:

$$\omega^2 \rho_o \boldsymbol{\xi} + \gamma P_0 (\mathbf{k} \cdot \boldsymbol{\xi}) \mathbf{k} + \frac{1}{\mu_0} \{\mathbf{k} \wedge [\mathbf{k} \wedge (\boldsymbol{\xi} \wedge \mathbf{B}_0)]\} \wedge \mathbf{B}_0 = 0, \tag{2.5}$$

where ω is the frequency and $\mathbf{k}$ is the wave vector. In so doing the system of differential equations is transformed to a set of algebraic equations. Further assuming with no loss of generality that $\mathbf{B}_0 = B_0 \hat{\mathbf{z}}$ and $\mathbf{k} = k_\perp \hat{\mathbf{y}} + k_\parallel \hat{\mathbf{z}}$ allows equation (2.5) to be written as

$$\begin{pmatrix} \omega^2 - k_\parallel^2 v_A^2 & 0 & 0 \\ 0 & \omega^2 - k_\perp^2 v_S^2 - k^2 v_A^2 & -k_\perp k_\parallel v_S^2 \\ 0 & -k_\perp k_\parallel v_S^2 & \omega^2 - k_\parallel^2 v_S^2 \end{pmatrix} \begin{pmatrix} \xi_x \\ \xi_y \\ \xi_z \end{pmatrix} = 0,$$

where $v_A = \sqrt{B_0^2/\mu_0\rho_0}$ is the Alfvén speed and $v_S = \sqrt{\gamma P_0/\rho_0}$ is the adiabatic sound speed. Non-trivial solutions of these equations follow by demanding that the determinant of the matrix be zero, giving the dispersion relation,

$$\left(\omega^2 - k_{\|}^2 v_A^2\right)\left[\omega^4 - (v_S^2 + v_A^2)k^2\omega^2 + (kk_{\|}v_S v_A)^2\right] = 0, \tag{2.6}$$

Each solution of this equation represents a mode of oscillation of the plasma and since it is a cubic polynomial in ω^2 three modes are expected.

The first solution,

$$\omega^2 = k_{\|}^2 v_A^2, \tag{2.7}$$

corresponds to the Alfvén branch and is independent of $k_\perp$, even when $k_\perp \gg k_{\|}$. These are incompressible ($\rho_1 = P_1 = 0$) transverse waves with both $\mathbf{v}_1$ and $\mathbf{B}_1$ perpendicular to $\mathbf{B}_0$. They represent a balance between plasma inertia and field line tension, with the field line tension understood by noting that the $\mathbf{j} \wedge \mathbf{B}$ force in a plasma is equivalent to an isotropic pressure $P = B^2/2\mu_0$ together with a tension $T = B^2/\mu_0$ per m^2. The plasma is carried along with these waves by the $(\mathbf{E} \wedge \mathbf{B})/B^2$ drift velocity which is in the same direction as the Poynting flux.

The quadratic term for ω^2 in equation (2.6) gives rise to two further branches, the fast and slow magnetosonic waves, which arise from the coupling between magnetic compression (Alfvénic) and fluid compression (sonic). The solutions are

$$\omega^2 = \frac{1}{2}k^2\left(v_S^2 + v_A^2\right)\left[1 \pm \sqrt{1 - 4\frac{k_{\|}^2}{k^2}\frac{v_A^2 v_S^2}{(v_A^2 + v_S^2)^2}}\right]. \tag{2.8}$$

By inspection it is easily seen that the square root term is always positive and less than unity, implying that the homogeneous magnetic field configuration is exponentially stable. This is consistent with the observation that the system is in thermodynamic equilibrium and there are no sources of free energy available to drive instabilities.

The positive sign in equation (2.8) corresponds to the fast magnetosonic or magnetoacoustic wave and always oscillates at frequencies greater than the Alfvén wave. This is a compressional wave, and so $\nabla \cdot \mathbf{v}_1$ and P_1 are non-zero, with $\mathbf{B}_1$ having components both parallel and perpendicular to the equilibrium field $\mathbf{B}_0$. A useful parameter characterising the equilibrium is the plasma β. The plasma is in equilibrium when the force balance condition $\mathbf{j} \wedge \mathbf{B} = \nabla P$ holds everywhere. Since this equation is linear in the plasma pressure, but quadratic in the field strength by Ampère's law, it is the ratio

$$\beta = \frac{P}{B^2/2\mu_0},$$

that characterizes the equilibrium. Following on from the observation above that the plasma fluid is frozen to the magnetic field lines, it becomes apparent that in a high-β situation, such as that where the solar wind encounters the Earth's magnetic field,

the magnetic field lines follow the plasma motion, whilst in a low-β situation such as a typical tokamak equilibrium, the reverse is true. Physically, β is a measure of the plasma energy density compared to the magnetic field energy density. It is also convenient to relate β to the characteristic wave speeds in the plasma through

$$\beta = \frac{2}{\gamma}\frac{v_S^2}{v_A^2}.$$

In the low-β limit, $\beta \sim v_S^2/v_A^2 \ll 1$, the fast magnetosonic wave reduces to the compressional Alfvén wave, or fast wave, with

$$\omega^2 = (k_\parallel^2 + k_\perp^2)v_A^2 = k^2 v_A^2 \tag{2.9}$$

and propagates isotropically with speed v_A. A further consequence of the low-β limit is that $\mu_0 P_1/B_0 B_1 \sim \beta \ll 1$, indicating that most of the compression involves the magnetic field and not the plasma. Waves of this type describe the interchange between the energy needed to compress and bend the magnetic field with perpendicular plasma kinetic energy. Since the parallel velocity is of order β compared with the perpendicular energy the plasma motion is nearly transverse.

The negative sign in equation (2.8) corresponds to the slow magnetosonic wave with this wave always oscillating at frequencies below that of the Alfvén wave. As for the fast branch, the wave is polarized so that the plasma pressure and the magnetic field are compressed. In the low-β limit the slow wave reduces to the familiar ion sound wave in the parallel direction, $\omega^2 \approx k_\parallel^2 v_s^2$, and does not propagate in the perpendicular direction. In this case the mode is almost longitudinal since $\mathbf{k}_\perp \cdot \mathbf{v}_1 \approx 0$. The sound wave describes a basic oscillation between the parallel plasma kinetic energy and the plasma internal energy.

The ideal MHD waves display a strong anisotropy as is clear from a consideration of the phase velocity of plane waves. All three MHD wave modes have constant phase velocities given by equations (2.7) and (2.8) for all frequencies and hence there is no wave dispersion. The phase velocity surfaces, or wave normal surfaces, for each of these waves are shown in Figs. 2.3 and 2.4 for the cases when $v_A > v_S$ and $v_A < v_S$. In these diagrams the magnitude of a vector drawn from the origin to a point on the curve represents the phase velocity of a plane wave propagating in that direction relative to $\mathbf{B}_0$.

2.1.3 Inhomogeneous Plasma

The plasma waves described by the ideal MHD equation (2.5) are stable in homogeneous equilibria. An important result concerning the general instability problem in inhomogeneous geometry is that the most unstable perturbations (such as pressure driven flute-like modes and current driven modes) are almost always coupled with the shear Alfvén wave. The reason for this can be seen by examining the dispersion relations in

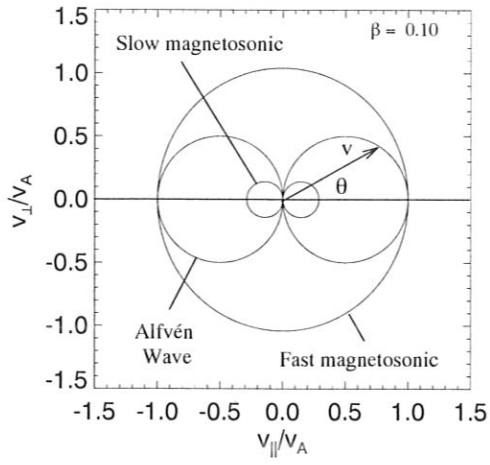

Figure 2.3: Phase velocities of ideal MHD plasma waves for $v_A > v_S$

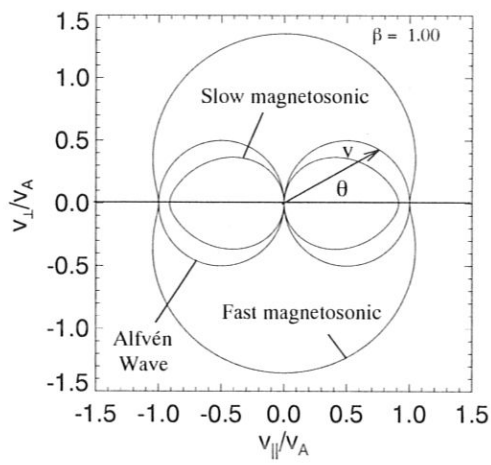

Figure 2.4: Phase velocities of ideal MHD plasma waves for $v_A < v_S$

equations (2.7) and (2.9) and viewing the wave numbers as effective spring constants. The larger the spring constant the greater the plasma is able to maintain its state under the influence of external perturbations. Consequently the shear Alfvén waves are more likely to go unstable in comparison with the compressional waves since $k_\parallel \leq \sqrt{k_\parallel^2 + k_\perp^2}$. From a consideration of typical dimensions in tokamak plasmas $k_\perp > k_\parallel$, further tipping the instability balance towards the shear Alfvén wave. In this thesis only the effects associated with the shear Alfvén branch are considered.

To begin a description of the Alfvén instabilities driven by super-Alfvénic energetic particles it is first noted that the presence of inhomogeneities in the plasma density and magnetic fields strongly affects the character of the Alfvén waves described above [21]. Particularly, it is easy to see that no wave packet of finite size across the magnetic field can persist for a long time, since the requirement that each 'slice' along the wave packet satisfies the local dispersion relation

$$\omega = k_\parallel(r) v_A(r)$$

implies that each slice moves with a different velocity and in a different direction. This effect, known as phase mixing [22], effectively leads to the damping of any initial Alfvén perturbation in an inhomogeneous plasma at the rate

$$\gamma_d \sim -\left| \frac{d}{dr} k_\parallel(r) v_A(r) \right|.$$

It was mainly for this reason that Alfvén instabilities driven by energetic ions were not considered a threat to future tokamak reactors. However, the discovery of weakly

damped Global Alfvén Eigenmodes (GAE) [23, 24] and weakly damped Toroidal Alfvén Eigenmodes (TAE) [6, 7] has changed this perspective.

2.1.4 The Alfvén Wave Resonant Absorption in Cylindrical Inhomogeneous Plasma

A description of the specific properties of the weakly-damped GAE and TAE which distinguishes them from the local Alfvén wave may be obtained from an initial consideration of the effect of Alfvén wave resonant absorption (see for example [25]) in more realistic cylindrical plasmas. Allowing the plasma density to depend on the radius introduces some new physical effects which are important for the consideration of tokamaks since in some respects a torus can be approximated by a bent cylinder upon applying periodic boundary conditions at the ends.

To begin with, consider the radial penetration of an externally applied wave with frequency ω and axial and azimuthal mode numbers k_z and m into a cylindrical inhomogeneous plasma immersed in a homogeneous magnetic field B_0. Using the ideal MHD approach and describing the radial component of the perturbed plasma displacement in the form,

$$\tilde{\xi}_r(r,\theta,z,t) = \sum_m \xi_m(r) e^{i(m\theta + k_z z + \omega t)},$$

the equation which describes radial penetration of an externally applied electromagnetic wave of the Alfvén frequency wave range may be written [23, 24],

$$\frac{d}{dr} r^3 \left(\frac{\omega^2}{v_A^2} - k_{||}^2 \right) \frac{d\xi_r}{dr} - (m^2 - 1) r \left(\frac{\omega^2}{v_A^2} - k_{||}^2 \right) \xi_r = 0, \tag{2.10}$$

where it is recalled that the Alfvén speed is determined by the local plasma density and is therefore generally a function of radius, $v_A = v_A(r)$; rising at the plasma edge as the density decreases.

In order to obtain the radial structure of the electromagnetic wave it is noted that the displacement ξ_r has a singularity centered upon the surface $r = r_0$ where the wave frequency coincides with the frequency of the local Alfvén continuum,

$$\omega = k_{||} v_A(r),$$

as illustrated in Fig. 2.5. The singularity appears because of the fact that ideal MHD does not permit the propagation of the shear Alfvén wave across the magnetic field. To solve the wave equation on both sides of the resonant point r_0 in term of ideal MHD one should use the analytic continuation of the solutions in the ranges $r < r_0$ and $r > r_0$ to obtain an imaginary contribution to the solution [21]. This imaginary part represents the resonant absorption of the external perturbation at $r = r_0$ where the applied frequency resonates with the local Alfvén wave. This resonant absorption

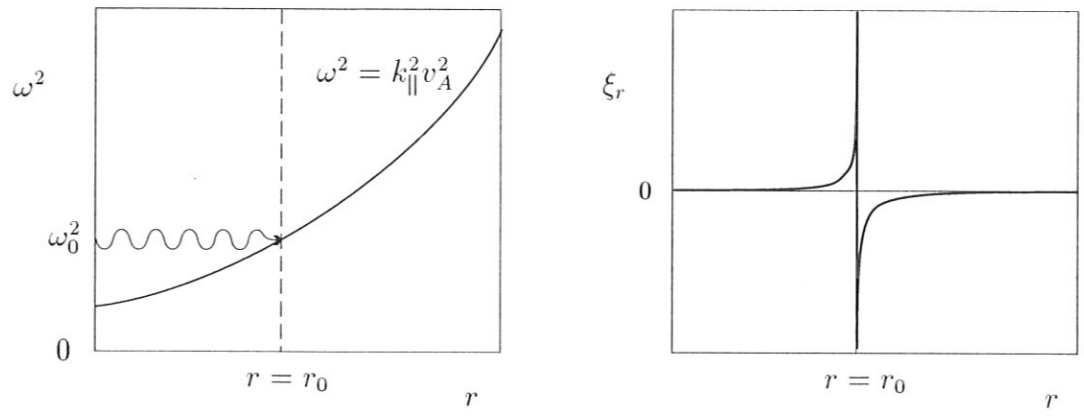

Figure 2.5: Cylindrical frequency continuum and continuum mode eigenfunction excited by externally applied wave with frequency ω_0.

(also known as 'continuum damping') can be shown [25] to be almost complete if r/m is chosen to be of the order of the plasma non-uniformity scale length.

Solutions such as these are referred to as continuum modes since they form a bounded frequency continuum. The restricted frequency range arises from the bounded range of v_A which generally has a maximum at the plasma edge as the density drops and a minimum at some radius, not necessarily the axis. Hence the plasma will only support shear Alfvén waves over a restricted frequency range, with each cylindrical surface oscillating at its own local frequency for a given $k_{||}$.

For a detailed description of the electromagnetic wave absorption in a high-temperature plasma in terms of the wave interaction with ions and electrons, one should go beyond the ideal MHD model and take into account finite Larmor radius effects (FLR). This introduces additional higher-order derivatives into equation (2.10) in the vicinity of the resonance and ultimately resolves the singularities.

Above it was demonstrated that the ideal MHD shear Alfvén wave is not dispersive,

$$\frac{\partial \omega}{\partial k_\perp} = 0.$$

However, in the vicinity of a local Alfvén resonant surface where $v_A = \omega/k_{||}$ the perpendicular wavelength $2\pi/k_\perp$ becomes comparable with the ion gyroradius ρ_i so that the ideal MHD description breaks down and finite Larmor radius (FLR) effects become important. In these circumstances the ions need no longer follow the magnetic field lines, whereas the electrons do because of their smaller Larmor radius. This effect produces charge separation and coupling to the Kinetic Alfvén Waves (KAW) having a dispersion relation for oblique propagation to the magnetic field lines:

$$\frac{\partial \omega}{\partial k_\perp} = v_g \neq 0.$$

The inclusion of these kinetic effects in the dispersion relation yields the modification

$$\omega^2 = \left\{1 + \left(\frac{3}{4} + \frac{T_e}{T_i}\right)(1 - i\delta_e)\, k_\perp^2 \rho_i^2\right\} k_\parallel^2 v_A^2,$$

with the dispersive behaviour controlled by the ion gyroradius, ρ_i. T_e and T_i are the ion and electron temperatures respectively and δ_e characterises the electron damping of the kinetic Alfvén waves by introducing a small imaginary term.

2.1.5 Cylinder With Axial Current

The addition of an axial current to the cylindrical model results in the magnetic field lines becoming helical in nature and $k_\parallel$ gaining a radial dependence, $k_\parallel = k_\parallel(r)$. Whenever

$$\frac{k_\parallel'}{k_\parallel} = -\frac{v_A'}{v_A}$$

the Alfvén continuum branch has a minimum off axis as shown in Fig. 2.6. Applying an

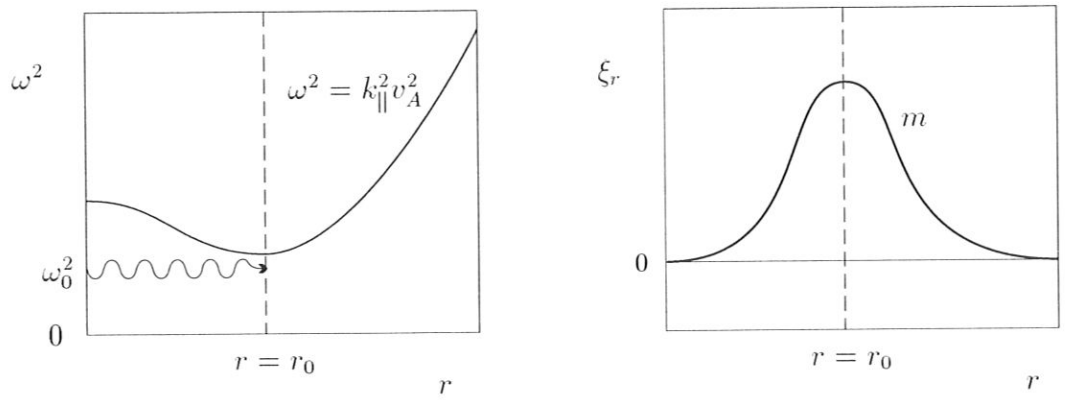

Figure 2.6: Frequency continuum in a current carrying cylinder and the corresponding discrete global eigenmode with poloidal harmonic number m excited by an externally applied wave of frequency ω_0.

external wave with a frequency just below the minimum of ω_A^2 the authors [23, 24] have found a surprising new discrete solution, the so-called weakly damped Global Alfvén Eigenmode (GAE). This result can be explained by reformulating equation (2.10) and including the effects of the additional current [23, 24],

$$\frac{d}{dr} r^3 \left(\frac{\omega^2}{v_A^2} - k_{\parallel m}^2\right) \frac{d\xi_r}{dr} - (m^2 - 1) r \left(\frac{\omega^2}{v_A^2} - k_{\parallel m}^2\right) \xi_r + \underbrace{\left(\frac{\omega^2}{v_A^2}\right)' r^2 \xi_r}_{\text{Current dependent term}} = 0. \qquad (2.11)$$

Qualitatively it is seen from equation (2.11) that if ω is just below the frequency continuum minimum such that $\omega^2 \approx \omega_A^2$, then there exists a region where the second term may be neglected and it is possible to integrate the resulting equation as before. However, the singularity in the eigenfunction no longer occurs at $r \simeq r_0$ due to the inclusion of the current dependent terms. The weakly damped nature of the GAE is a consequence of a specific property of this AE: It does not satisfy the local Alfvén resonance condition at any point across the plasma. Physically, this solution may be understood by drawing an analogy with a fibre-optic filament: Moving away from the minimum point at $r = r_0$, the local Alfvén frequency grows and the effective perpendicular refractive index $N_\perp = ck_\perp/\omega$ decreases from its maximum at $r = r_0$. Consequently electromagnetic waves are reflected by the decreasing $N_\perp$ and are localised around this point.

Summarizing the structure of the Alfvén spectrum in an inhomogeneous cylindrical plasma with longitudinal current, it is seen that under certain conditions the spectrum consists of the usual shear Alfvén continuum and weakly damped discrete global eigenmodes.

2.1.6 Toroidal Plasma

In a torus, by virtue of the periodicity in the poloidal and toroidal directions, a wave field perturbation may be described by a Fourier decomposition in poloidal and toroidal harmonics as

$$\xi(r,\theta,\varphi) = \sum_{m,n} \xi_{m,n}(r) e^{i(n\varphi - m\theta - \omega t)} \tag{2.12}$$

where n is the toroidal mode number. Since the equilibrium magnetic field $B \approx B_0(1 - r/R_0 \cos\theta)$ is a function of θ, a coupling of the different poloidal harmonics arises in ξ. For a particular toroidal mode number, and to the lowest order in the expansion parameter $\varepsilon = a/R_0$, each poloidal harmonic ξ_m only couples to its nearest neighbouring sidebands, $\xi_{m\pm1}$.

Neglecting kinetic effects, the force-operator equation (2.3) can be written as a set of coupled equations in the form [26]

$$\begin{pmatrix} P_m & Q \\ Q & P_{m+1} \end{pmatrix} \begin{pmatrix} \xi_m \\ \xi_{m+1} \end{pmatrix} = 0 \tag{2.13}$$

where

$$\begin{aligned} P_m &= \frac{d}{dr} r^3 \left(\frac{\omega^2}{v_A^2} - k_{\|m}^2 \right) \frac{d}{dr} - (m^2 - 1) r \left(\frac{\omega^2}{v_A^2} - k_{\|m}^2 \right) + \left(\frac{\omega^2}{v_A^2} \right)' r^2 \\ Q &= \frac{5}{2} \varepsilon \frac{d}{dr} \frac{\omega^2}{v_A^2} \frac{r^4}{a} \frac{d}{dr} \end{aligned}$$

and the subscripts m and $m+1$ denote the two dominant poloidal mode numbers present. The quantities $k_{\|}$ and q are approximately given by

$$k_{\|m} = \frac{1}{R}\left(n - \frac{m}{q(r)}\right), \qquad q(r) = \varepsilon \frac{B_{tor}}{B_{pol}}$$

where $\varepsilon = r/R_0$. In the cylindrical limit ($\varepsilon = 0$) the two poloidal harmonics decouple and the cylindrical equation discussed above is recovered.

At each surface non-trivial solutions still exist corresponding to a set of eigenvalues of ω^2 which form a continuous spectrum for the equilibrium as in the cylindrical and homogeneous cases considered above. However, since the parallel component of the wave vector now also depends on m and θ, curves of the form $\omega^2 = k_{\|m}^2 v_A^2$ can be expected to cross. Toroidicity resolves this degeneracy at the points of intersection to produce gaps in the frequency continuum as shown in Fig. 2.7. In the cylindrical case

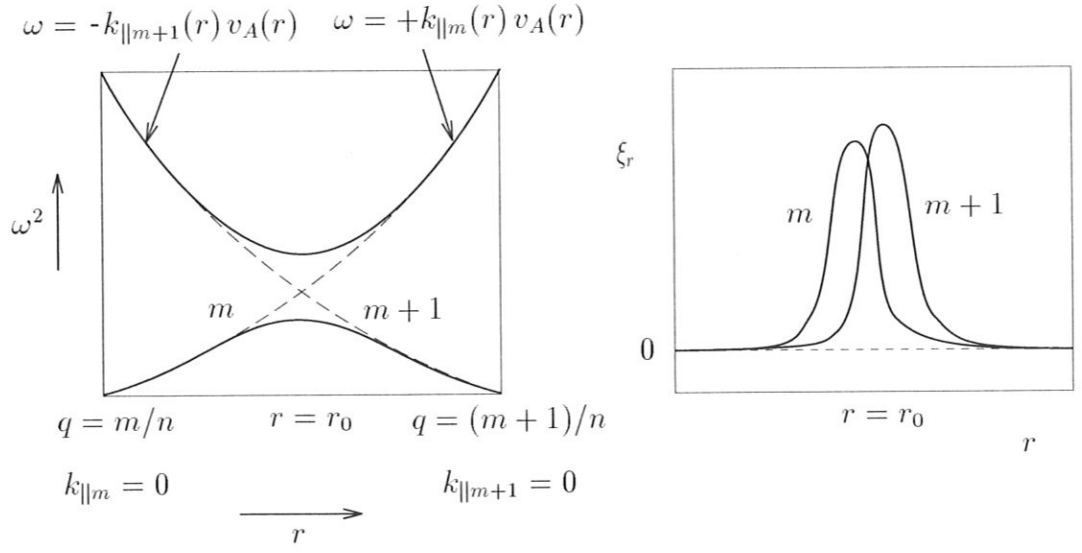

Figure 2.7: Coupling of poloidal harmonics in a torus and the corresponding TAE eigenfunctions

it was the occurrence of an off-axis minimum in the profile of ω^2 which permitted GAE to exist. In the toroidal case the Alfvén continuum already contains a minimum at the surface where $r \approx r_0$ with r_0 determined by the condition

$$k_{\|m}(r_0) = -k_{\|m+1}(r_0)$$

which is approximately equivalent to the position where

$$q(r_0) = \frac{m + \frac{1}{2}}{n}$$

as seen from Fig. 2.7. Consequently, global Alfvén solutions of equation (2.13) may be expected to exist by analogy to the GAE case described above. These weakly damped Alfvén eigenmodes were discovered in references [6, 7] where they were called Toroidal Alfvén Eigenmodes (TAE).

Like the cylindrical GAE, the TAE eigenfrequency does not satisfy the local Alfvén resonance condition since it lies in the gap in the frequency continuum. Consequently the TAE does not experience heavy continuum damping and is therefore weakly damped. The global eigenfunctions are mainly located around the region of the minimum of ω^2 as for the GAE and as indicated in Figs. 2.6 and 2.7, but every TAE consists of two poloidal harmonics in contrast to the GAE. Since the toroidal minimum is the result of the interaction between neighbouring harmonics there are primarily two poloidal global eigenfunctions associated with each toroidal frequency gap.

It is also possible to obtain GAE in toroidal geometry as in the cylindrical case if ω^2 has an off-axis minimum due to the plasma density and field profiles. It can be shown that a GAE oscillating at a frequency ω just below the continuum minimum will intersect the continuum since $k_{||}$ goes to zero on the rational q surfaces. At these locations the global mode will resonate with the local continuum mode which results in strong continuum damping of the GAE [27].

2.2 Growth and Damping Mechanisms of AE

The following discussion introduces the dominant damping mechanisms experienced by Alfvén Eigenmodes. The particular plasma parameters of the system under consideration determine which particular mechanisms act as the strongest energy source and strongest sink.

Consider an AE instability driven by super-Alfvénic ions whose energy content is small in comparison with the bulk energy content. In this case a perturbative approach may be used where the zeroth order solution is determined by the bulk plasma and the energetic particles produce only a small imaginary contribution to the eigenfrequency — the growth rate of the wave. Such a perturbative approach requires that

$$\gamma \ll \omega.$$

Considering an exponentially growing wave amplitude such that

$$A = A_0 e^{\gamma t}$$

allows the growth rate to be easily described by considering the power transfer from particles to wave. The energy possessed by each wave is proportional to the square of its amplitude and so

$$E = E_0 e^{2\gamma t}$$

$$\Rightarrow \quad \frac{\partial E}{\partial t} = 2\gamma E$$
$$\Rightarrow \quad \gamma = \frac{1}{2E}\frac{\partial E}{\partial t} = \frac{P}{2E}$$

where $P = P_f - P_d$ is the sum of the power transfers to the wave from the energetic particles P_f and the bulk plasma P_d. Thus the total linear growth rate arising from the contributions from the fast particles present and any damping mechanisms may be written

$$\gamma = \gamma_f - \gamma_d = \frac{P_f - P_d}{2E} = \frac{\text{Power transfer to wave}}{2 \times \text{Wave Energy}}.$$

The remainder of this section provides a brief qualitative description of the principal damping mechanisms experienced by AE within tokamak plasmas.

2.2.1 Damping Mechanisms due to the Bulk Plasma

Continuum Damping

It was mentioned above that the main reason that toroidal Alfvén eigenmodes are weakly damped is the absence of continuum damping in the region where the mode is localised. However it is possible for the tail of the eigenfunction to spread up to a local Alfvén resonance surface where it can experience a small residual amount of continuum damping. For low-n TAE this continuum damping was considered in the paper [28] and for high-n in [29, 30].

Ion Landau Damping

For typical tokamak plasma parameters a Maxwellian distribution of thermal ions contains a negligibly small number of ions capable of resonating with the AE at the $v_{||} = v_A$ resonance. However it was shown in [4, 5] that the magnetic field curvature modifies the resonant condition such that it becomes

$$\omega - k_{||}v_{||} - \mathbf{k}_\perp \cdot \mathbf{v}_{di} = 0,$$

where $\mathbf{v}_{di}$ is the magnetic drift velocity,

$$\mathbf{v}_{di} = \frac{v_{||}^2 + v_\perp^2}{\omega_{ci}}[\hat{\mathbf{B}} \wedge \boldsymbol{\nabla}(\ln B)].$$

The $\mathbf{k}_\perp \cdot \mathbf{v}_{di}$ term in this expression effectively reduces the frequency of the eigenmode and allows the wave to resonate with sub-Alfvénic particles through a $v_{||} = v_A/3$ resonance. The resonant contribution of the ions at $v_A/3$ can be estimated for a D-T plasma as [32, 33]

$$\frac{\gamma_i}{\omega} \approx -\frac{1}{243\sqrt{\pi}}\, q^2 \sum_{i=D,T} \beta_i^{-\frac{3}{2}} \exp\left(-\frac{1}{9\beta_i}\right),$$

where q is the safety factor and $\beta_i = 2T_i/m_i v_A^2$ is the ion beta.

The ion Landau damping is one of the most important stabilizing effects in ignited tokamak plasmas. Note however, that this damping mechanism is exponentially sensitive with respect to β_i so that it can be difficult to predict the level of damping with a high degree of reliability.

Electron Collisional Damping

For typical tokamak reactor parameters, the characteristic electron thermal velocity v_{Te} is much greater than the Alfvén velocity. Thus only electrons with $v_{\|e} \ll v_{\perp e}$ can move longitudinally with the Alfvén velocity. All these electrons are trapped[1] however and cannot contribute significantly to electron Landau damping [4, 34]. An alternative electron damping mechanism has been proposed in [31, 35]. The effect arises from the transitions of the electrons from trapped to passing orbits due to collisions.

Radiative Damping of TAE

The small but finite coupling of the ideal MHD TAE with a kinetic Alfvén wave can be described by the dispersion relation:

$$\omega = \pm \underbrace{k_{\|m} v_A}_{\partial\omega/\partial k_\perp = 0} \underbrace{\left[1 + \left(\frac{3}{4} + \frac{T_e}{T_i}\right)(k_\perp \rho_i)^2\right]}_{\partial\omega/\partial k_\perp \neq 0}$$

The inclusion of FLR corrections reveals a finite radial group velocity which carries energy away from the localisation of the TAE eigenfunction in the form of an outgoing radiative kinetic Alfvén wave (KAW). This effect is known as the 'radiative damping' of TAE [36]. It has also been shown [33, 36, 37, 38, 39] that kinetic Alfvén waves with frequencies above the toroidicity induced gap can form weakly-damped AE called kinetic TAE (KTAE).

2.3 Energetic Particle Drive For Weakly Damped AE

2.3.1 Linear Theory

Before going on to discuss particle motion in detail it is possible to gain a qualitative understanding of the principle effects arising from wave-particle interaction by considering the interaction of a single wave with a solitary passing particle. Denoting the phase of the wave by Θ it is observed that the Θ seen by the particle will in general be

[1] See Fig. 2.14 and the preceding discussion for an explanation of this term.

continuously changing and the forces exerted by the wave upon the particle will average to zero. However if on average Θ is almost constant, then these forces will allow the particle to resonately exchange energy with the wave. The resonance condition is thus

$$\langle \dot{\Theta} \rangle \simeq 0. \tag{2.14}$$

Upon assuming that passing particles approximately follow magnetic field lines with an orbit deviation of the order of

$$\Delta_{b\alpha} = \left(v_{\|}^2 + \frac{v_{\perp}^2}{2} \right) \frac{q}{v_{\|} \omega_{B\alpha}}$$

accounted for through a Fourier expansion in $l\theta$ harmonics, the resonance condition becomes

$$\frac{n}{R} v_{\|} - \frac{m+l}{qR} v_{\|} - \omega = 0.$$

This may be rearranged to give

$$v_{\|} = \frac{qR\omega}{nq - m - l},$$

which is the condition on the particle's parallel velocity for it to experience a nearly constant phase of a particular wave whose wave vector is described through the mode numbers m and n. For TAE modes the global eigenfunction associated with the poloidal harmonics m and $m+1$ is primarily localised in the region $q = (2m+1)/2n$, as can be seen from Fig. 2.7. Thus it is expected that the strongest wave-particle interaction will occur in this region. Evaluating the above expression for $v_{\|}$ at this location gives

$$v_{\|} = \frac{v_A}{|2l - 1|}$$

where $l = 0$ corresponds to the primary resonance $v_{\|} = v_A$, and other values of l correspond to sideband resonances at lower velocities. In JET, fusion α-particles are born nearly isotropically with a velocity $v \simeq 2.2\, v_A$ allowing them to resonate with the v_A primary resonance and all other sidebands. The NBI system in JET however injects particles with an energy of 140 keV corresponding to $v = 0.56\, v_A$. These particles are thus only capable of resonating with the $v_A/3$ resonance and lower.

In contrast to the bulk ion Landau damping, the interaction of α-particles and Alfvén waves must include the principle $v_{\|} = v_A$ resonance. For a typical slowing-down distribution of α-particles the wave-particle interaction can be estimated as [26]

$$\frac{\gamma}{\omega} = \frac{9}{4} \beta_f \left(\frac{\omega_{*\alpha}}{\omega} - \frac{1}{2} \right) F \left(\frac{v_A}{v_\alpha} \right), \tag{2.15}$$

where

$$\omega_{*\alpha} = -k_\theta \frac{T_\alpha}{e_\alpha B_0} \frac{d \ln \beta_f}{dr}$$

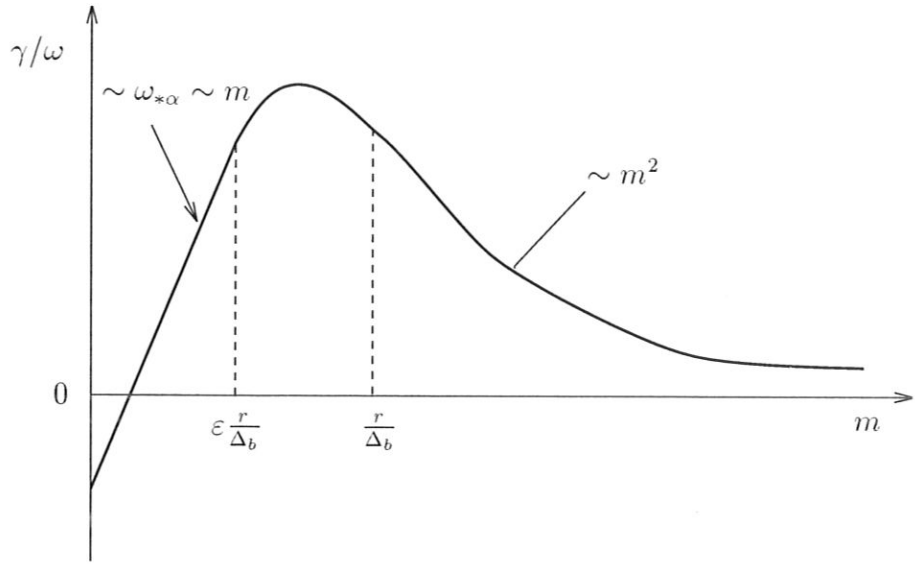

Figure 2.8: Scaling of linear growth rate with ratio of orbit width to radial scale length of eigenmode for passing particles

is the drift frequency associated with the spatial gradient of α-particles, ω is the AE frequency and

$$F(x) = x(1 + 2x^2 + 2x^4)e^{-2x^2}.$$

The first term in equation (2.15) represents the free energy source associated with the radial α-particle pressure gradient and the second term is due to the negative gradient of α-particle energy, $\partial F/\partial \mathcal{E} < 0$. The second term is therefore responsible for the damping due to the energetic particles. For highly centrally peaked α-particle pressure profiles, the first term can lead to an instability of AE, releasing the free energy due to the radial gradient in the form of a growing AE through the resonant interaction between particles and wave. Note here that the expression above has been obtained in the limit of small particle orbits. However, for particle orbit widths comparable with the radial scale length of the AE, the growth rate was found to saturate [43] at $\Delta_b \sim \mathcal{O}(\frac{\varepsilon r}{m})$ and then decay at a rate proportional to m^{-2} [39] for Δ_b larger than r/m as shown in Fig. 2.8. The problem of calculating the linear growth rate in the case of arbitrary magnetic field geometry and general particle orbits is much more complicated than for simple passing particles and a more numerical treatment is needed in this case.

2.3.2 Nonlinear Modelling of Resonant Wave-Particle Interaction

To the extent that the source of free energy driving an AE comes from the radial gradient of the fast particle population, the nonlinear stage of the eigenmodes' evolution (in the absence of sources and sinks) corresponds to the plateau formation on the

distribution function. The plateau being centered around the flux surfaces where the AE is localised. Numerous efforts [14, 40, 41, 42] have previously been devoted to numerically modelling this effect for TAE and for the more simple (1-D) problem of the bump-on-tail instability.

In the early studies of the problem, without the δf formalism, the main results were obtained for the bump-on-tail instability [40] and for the TAE with enormous strains upon computing resources. As mentioned above, the δf formalism was found to be the most efficient method for the Monte-Carlo modelling of wave-particle resonant interactions.

The first successful results for the nonlinear evolution of TAE instabilities were obtained by Fu and Park [14] using 200,000 particles without using the δf technique. In this work the contribution of the energetic particles was taken into account in the form of the pressure-stress tensor. However, such an approach does not allow the finite orbit geometry effects to be taken into account. One of the important results of this work was an explicit demonstration that the main saturation mechanism is wave-particle trapping and that wave-wave nonlinearities may be neglected up to wave amplitudes of $\delta B/B \simeq 2 \times 10^{-3}$ at least.

In the mid-1980's White and Chance at Princeton developed a Hamiltonian guiding centre code, ORBIT [54], to examine particle trajectories in the presence of a spectrum of fixed amplitude AE [55]. This code was recently successfully used to model the nonlinear interaction of energetic particles and a single AE using a δf approach [42]. However, by choosing to update the wave amplitude from a consideration of energy conservation the treatment of systems with more than one AE becomes difficult. In our code we use a differential equation to continuously update the amplitude and phase of each AE. In particular, this allows us to analyse the behaviour of several AE.

Another advanced approach has recently been used by Berk, Breizman and Pekker [41] to analyse the nonlinear interaction of the resonant particles and an AE using a mapping technique to rapidly describe the particle motion. However, generating the matrix elements for the mapping requires detailed information about both the particle orbits and the wave structure *a-priori*.

In this thesis a numerical model is developed based upon the δf formalism for arbitrary particle orbits, arbitrary eigenmode structure and arbitrary toroidally symmetric field geometries. Although this thesis does not consider the effects arising from the inclusion of particle sources and sinks, the δf formalism promises to allow these effects to be included in a very natural way.

2.4 Particle Motion in Toroidal Magnetic Devices

In approaching any problem, the solution generally begins with some form of kinematic analysis: the analysis of how the system *can* move, as opposed to how it actually *does* move under the influence of a particular set of forces. In this first stage, the essential step is the introduction of an independent coordinate system which labels all the possible configurations of the system. Since the case being dealt with here is the complex problem of the interaction of energetic particles with a perturbed magnetic field, a representation is chosen that simplifies the equilibrium magnetic field description and exploits any symmetry properties of the field. This simplifies the equations of motion for the particles but means employing a non-orthogonal coordinate system, and hence a tensor description requiring the language of covariant and contravariant representations.

The second stage, the dynamical part of the problem, uses Newton's second law to determine the actual motion: to find out how the coordinates evolve as functions of time when the system is subjected to given forces. The Hamiltonian approach simplifies this second stage by providing techniques for finding the dynamical equations of the system, isolating the constants of the motion and exploiting them to solve for the particle trajectories.

2.4.1 Reference Frames

Since the fields and equilibria must ultimately be described in terms of a convenient laboratory coordinate system the coordinates used are taken to be functions of the familiar Cartesian system $\mathbf{x} = (x, y, z)$ or (x^1, x^2, x^3) by giving a set of three functions $\xi^i(\mathbf{x}) = \xi^i(x, y, z)$ for $i = 1, 2, 3$, where by convention, coordinates are denoted with a superscript. The ξ^i form a non-degenerate coordinate system if, and only if, the Jacobian,

$$\mathcal{J} \equiv \frac{1}{\nabla\xi^1 \cdot \nabla\xi^2 \wedge \nabla\xi^3},$$

is well behaved. The coordinate system is right-handed when $\mathcal{J} > 0$.

More general bases can be written in terms of a set of three vector fields that span the set of directions at every point in space. Any vector can be described in two forms namely the covariant form, [2]

$$\mathbf{A} = A_i \nabla\xi^i,$$

and the contravariant form,

$$\mathbf{A} = \frac{\varepsilon_{ijk}\mathcal{J}}{2} A^i \nabla\xi^j \wedge \nabla\xi^k \equiv A^i \frac{\partial \mathbf{x}}{\partial \xi^i},$$

where ε_{ijk} denotes the completely antisymmetric Levi-Civita symbol.

[2] Summation is henceforth assumed on repeated indices.

Magnetic Flux Coordinates

Due to the solenoidal nature of the magnetic field, a torus is the simplest topological configuration that can be assumed having no field lines exiting from it's bounded surface. A tokamak is such a configuration and in studying tokamak plasmas and fields it naturally makes sense to adopt a set of toroidal coordinates such as (ψ, θ, ζ) shown in Fig 2.9.

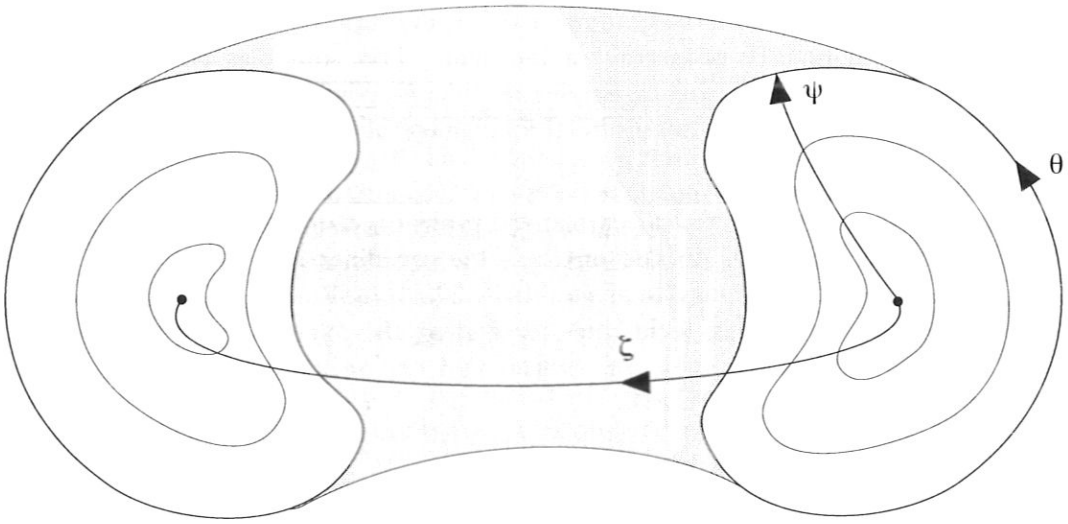

Figure 2.9: A general set of toroidal coordinates.

For an equilibrium with a scalar pressure the pressure gradient is balanced by the Lorentz force, $\mathbf{j} \wedge \mathbf{B} = \nabla P$, and it is seen that $\mathbf{j}$ and $\mathbf{B}$ lie in surfaces of constant pressure. These are usually referred to as magnetic surfaces since the field lines must lie in them, or as flux surfaces since the magnetic flux within each surface is necessarily constant through any cross-section. In such cases it is common to use so-called flux coordinates. These are curvilinear coordinate systems in which one of the coordinates, usually denoted by ψ, is constant over each flux surface. The other two coordinates form a grid within each surface such that they close upon themselves once around the torus in each direction. With such a definition, $\psi = \textit{constant}$ then defines a sequence of nested tori and $\mathbf{B} \cdot \nabla \psi = 0$.

The ultimate aim is to obtain a simple form for the Hamiltonian description of the particle motion. To realise this goal, the coordinate system must be chosen carefully. The trajectories of charged particles in a magnetic field are strongly tied to the field lines, so flux coordinates form a natural system because they allow the rapid particle motion along the field lines to be separated from the slow drift across the flux surfaces. Further, it is convenient to choose a set of flux coordinates such that as many of the relevant vector components as possible are constant within a flux surface. This enables

the description to be characterized by the flux label ψ.

Any unique labelling of the flux surfaces may be used for the radial coordinate ψ, although clearly it must be a monotonic function. Suitable labels include the volume inside a flux surface [44] and the toroidal or poloidal flux within the flux surface. Any function f that is constant on flux surfaces is referred to as a flux label and obviously $\mathbf{B} \cdot \nabla f = 0$. Any radial coordinate that vanishes on the magnetic axis, increases monotonically outwards, and has the dimensions of length, can loosely be identified with the minor radius.

Since the magnetic field lines lie on the flux surfaces, the contravariant component in the radial direction vanishes $\mathbf{B} \cdot \nabla\psi = B^{\psi} = 0$. The divergence-free nature of the magnetic field then implies that

$$\nabla \cdot \mathbf{B} = \frac{1}{\mathcal{J}} \left[\frac{\partial}{\partial\theta}(\mathcal{J}B^{\theta}) + \frac{\partial}{\partial\zeta}(\mathcal{J}B^{\zeta}) \right] = 0,$$

from which it follows that the magnetic field may be defined in terms of a stream function ν such that

$$\mathcal{J}B^{\theta} = -\frac{\partial\nu}{\partial\zeta}, \qquad \mathcal{J}B^{\zeta} = \frac{\partial\nu}{\partial\theta}, \tag{2.16}$$

where $\nu(\psi, \theta, \zeta)$ may be multi-valued in the angles θ and ζ. To ensure that the field itself is single-valued ν must be the sum of terms that are linear or periodic in θ and ζ:

$$\nu = u(\psi)\theta + v(\psi)\zeta + \lambda(\psi, \theta, \zeta), \tag{2.17}$$

where λ is a periodic function in θ and ζ. Functions such as ν are known as surface potentials, with the name reflecting the fact that it is the gradient of ν that is ultimately of physical significance.

Using the contravariant form for $\mathbf{B}$ and equation (2.16) it is seen that

$$\mathbf{B} = \frac{\partial\nu}{\partial\zeta}\nabla\psi \wedge \nabla\zeta + \frac{\partial\nu}{\partial\theta}\nabla\psi \wedge \nabla\theta, \tag{2.18}$$

but since

$$\nabla\nu = \frac{\partial\nu}{\partial\psi}\nabla\psi + \frac{\partial\nu}{\partial\theta}\nabla\theta + \frac{\partial\nu}{\partial\zeta}\nabla\zeta,$$

this implies that

$$\mathbf{B} = \nabla\psi \wedge \nabla\nu, \tag{2.19}$$

where ψ represents an arbitrary flux label, and ν a surface potential. Obviously, this form is only applicable when nested flux surfaces exist, however it is possible to characterize any toroidal magnetic field by writing

$$\mathbf{B} = \nabla\alpha \wedge \nabla\beta,$$

for some suitable functions α and β [46]. The functions α and β form part of what is known as close-line flux coordinates and can be used to describe any divergence-free vector field [45].

It is expected that the functions $u(\psi)$ and $v(\psi)$ that appear in the definition of ν are uniquely related to the toroidal and poloidal fluxes, ψ_t and ψ_p respectively. Therefore consider the fluxes between the adjacent surfaces, ψ and $\psi + d\psi$,[3]

$$\begin{aligned} d\psi_t &= \frac{1}{2\pi}\int_{\psi}^{\psi+d\psi} \mathbf{B}\cdot\nabla\zeta\, dx^3 \\ &= d\psi \int_0^{2\pi}\int_0^{2\pi} B^{\zeta}\,\mathcal{J}\, d\theta\, d\zeta \\ &= d\psi \int_0^{2\pi}\int_0^{2\pi} \frac{\partial\nu}{\partial\theta}\, d\theta\, d\zeta \\ &= d\psi \int_0^{2\pi}\int_0^{2\pi} \left(u(\psi) + \frac{\partial\lambda}{\partial\theta}\right) d\theta\, d\zeta \\ \Rightarrow \qquad d\psi_t &= u(\psi)\, d\psi. \end{aligned}$$

Similarly for the poloidal flux,

$$d\psi_p = -v(\psi)\, d\psi.$$

Thus

$$u(\psi) = \frac{d\psi_t}{d\psi}, \quad \text{and} \quad v(\psi) = -\frac{d\psi_p}{d\psi}.$$

By inspection it is easily seen from equation (2.19) that $\mathbf{B}$ is perpendicular to $\nabla\nu$ everywhere, implying that field lines lie on surfaces of constant ν, whence the equation of a field line on a flux surface is defined by the integral

$$\nu(\psi,\theta,\zeta) = \textit{constant}, \qquad \psi = \textit{constant}. \tag{2.20}$$

Straight Field Line Coordinates

Since the form of the 'angle' coordinates θ and ζ has not been specified, they may be deformed at will provided that they close upon themselves once around the torus in each direction. This makes it possible to construct either orthogonal coordinates, or coordinates in which the magnetic field lines appear as straight lines, as in Fig. 2.10. Such straight field lines will result on a flux surface when a representation is obtained in which the equation of a field line (2.20) is linear in the angular coordinates θ and ζ. Consequently it is seen from equation (2.17) that this form will occur when λ is eliminated from ν. This may be achieved by either deforming θ or ζ individually,

$$\theta_{new} = \theta_{old} - \frac{\lambda}{u(\psi)}, \qquad \zeta_{new} = \zeta_{old},$$

or,

$$\theta_{new} = \theta_{old}, \qquad \zeta_{new} = \zeta_{old} - \frac{\lambda}{v(\psi)},$$

[3] It is assumed here that θ and ζ have periodicities of 2π.

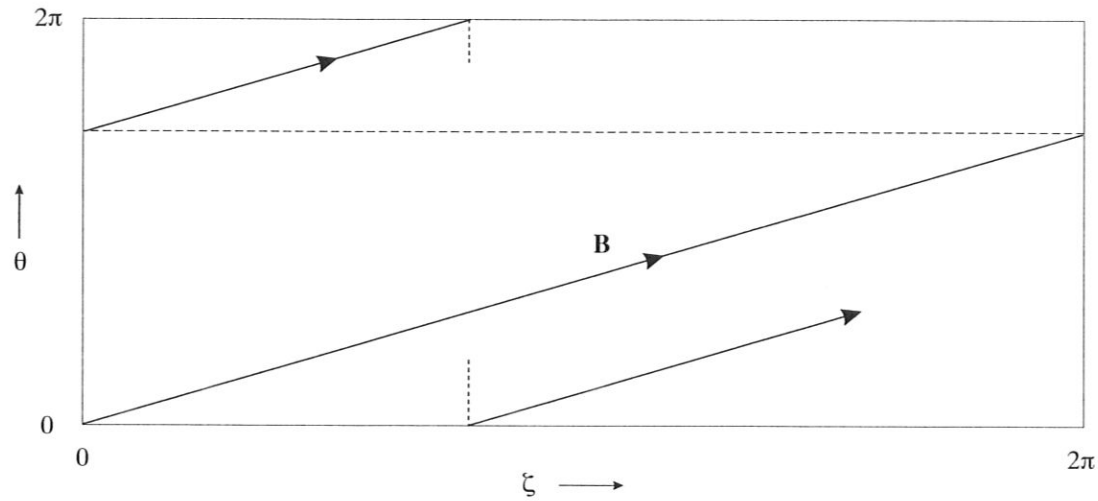

Figure 2.10: Toroidal flux surface showing straight magnetic field lines in the appropriate θ-ζ coordinates.

or by some linear combination of these two transformations, the choice is not unique, from which it follows that

$$\begin{aligned} \nu &= u(\psi)\theta + v(\psi)\zeta, \\ \Rightarrow \qquad \nabla\nu &= u(\psi)\nabla\theta + \theta\frac{\partial u}{\partial\psi}\nabla\psi + v(\psi)\nabla\zeta + \zeta\frac{\partial v}{\partial\psi}\nabla\psi, \end{aligned}$$

and hence from equation (2.19),

$$\mathbf{B} = u(\psi)\nabla\psi \wedge \nabla\theta - v(\psi)\nabla\zeta \wedge \nabla\psi.$$

Using the expressions for u and v this can be written as

$$\mathbf{B} = \frac{d\psi_t}{d\psi}\nabla\psi \wedge \nabla\theta + \frac{d\psi_p}{d\psi}\nabla\zeta \wedge \nabla\psi, \tag{2.21}$$

which by inspection can be seen to be consistent with a vector potential of the form,

$$\mathbf{A} = \psi_t\nabla\theta - \psi_p\nabla\zeta.$$

It is notable that the covariant components of the vector potential in straight field line coordinates are flux functions. All variation of $\mathbf{A}$, and therefore $\mathbf{B}$, upon a flux surface is hidden in the definitions of the basis vectors, $\nabla\theta$ and $\nabla\zeta$.

Selecting a particular flux label ψ and constraining θ and ζ to produce straight field lines still leaves one remaining degree of freedom that can be exploited in the specification of the coordinate triplet ψ, θ, ζ. This freedom may be used to obtain a specific form for the Jacobian. For numerical calculations this choice can be relevant,

as it determines the nature of the spacing of grid points in the discrete coordinate mesh. Hamada [47] used this freedom to produce a magnetic coordinate system with a Jacobian that is constant on a flux surface. By specifically choosing the Jacobian to be unity throughout the field, the physical volume element is simply given by $d\xi^1\, d\xi^2\, d\xi^3$. For example, a Jacobian of $\mathcal{J} \propto R^2$ is used in the MHD stability code CASTOR [49], and in the equilibrium code HELENA [48]. This choice is made so that the toroidal angle coordinate is equal to the familiar azimuthal angle, φ. Boozer [50] has also demonstrated that this freedom can be used to simplify the covariant representation of the field such that the angular components become flux surface quantities.

Above it was demonstrated that the use of flux coordinates implies that field lines are described by the contours of constant ν on a flux surface. In a straight field line representation the description becomes trivial since ν is now linear:

$$\zeta - q(\psi)\theta = constant, \qquad \psi = constant.$$

where q is the so-called safety factor,[4] and corresponds to the reciprocal of the gradient of the field line in Fig. 2.10. It is clear from this that q is just the ratio of the contravariant components of $\mathbf{B}$, $q = B^\zeta / B^\theta$, which from equation (2.21) means that

$$q = \frac{d\psi_t}{d\psi_p}.$$

Thus in any straight field line coordinates it is seen that the ratio of the angular contravariant components of the magnetic field is constant within a flux surface.

2.4.2 Guiding Centre Motion

Much insight into the macroscopic behaviour of a plasma can be obtained from a consideration of single particle motion. The equation of motion of a non-relativistic particle of charge q in an electric field, $\mathbf{E}$, magnetic induction field, $\mathbf{B}$, and external force $\mathbf{F}$ is

$$m\frac{d\mathbf{v}}{dt} = \mathbf{F} + e\,(\mathbf{E} + \mathbf{v} \wedge \mathbf{B}) \tag{2.22}$$

For tokamaks, external fields such as gravity are negligible in comparison with the electromagnetic forces present.

Energy Conservation

By only considering the effect of the $\mathbf{B}$ field upon a particle the equation of motion (2.22) reduces to

$$m\frac{d\mathbf{v}}{dt} = e\mathbf{v} \wedge \mathbf{B}. \tag{2.23}$$

[4] q is known as the safety factor because of the important rôle it plays in plasma stability. In particular, rational values of q correspond to surfaces with closed field lines that are especially vulnerable to electromagnetic perturbations.

Since the magnetic force is perpendicular to $\mathbf{v}$ it does no work on the particle and taking the dot product of (2.23) with $\mathbf{v}$ gives

$$m\frac{d\mathbf{v}}{dt}\cdot\mathbf{v} = \frac{d}{dt}\left(\frac{1}{2}mv^2\right) = 0$$

which shows that the particle kinetic energy ($\frac{1}{2}mv^2$) and speed are both constants. This result is valid for any spatial dependence of $\mathbf{B}$, provided it doesn't vary with time. If it does depend on time then Faraday's Law implies that an electric field will also be present which can do work on the particle thereby changing it's kinetic energy.

When both magnetostatic and electrostatic fields are present, then from (2.22)

$$\frac{d}{dt}\left(\frac{1}{2}mv^2\right) = e\mathbf{E}\cdot\mathbf{v}.$$

In this case $\nabla\wedge\mathbf{E} = 0$ so the electric field may be expressed in terms of the electrostatic potential according to $\mathbf{E} = -\nabla\phi$ giving

$$\frac{d}{dt}\left(\frac{1}{2}mv^2\right) = -e\nabla\phi\cdot\mathbf{v} = -e\frac{d\phi}{dt}.$$

Rearranging the result gives the following conservation law

$$\frac{d}{dt}\left(\frac{1}{2}mv^2 + e\phi\right) = 0,$$

which reveals that the sum of the particle's kinetic and electric potential energies remains constant in the presence of static electromagnetic fields.

It was assumed above that the particle energy changes only as a result of the work done by the external fields. This assumption is not strictly true since an accelerating charged particle radiates energy in the form of electromagnetic waves [51]. However, this effect is very small and will be neglected in this thesis.

Uniform Magnetic Field

The relevant equation of motion is

$$m\frac{d\mathbf{v}}{dt} = e\mathbf{v}\wedge\mathbf{B}$$

which by considering components parallel and perpendicular to $\mathbf{B}$ becomes

$$\frac{d\mathbf{v}_{\|}}{dt} = 0 \tag{2.24a}$$

$$\frac{d\mathbf{v}_{\perp}}{dt} = \frac{e}{m}(\mathbf{v}_{\perp}\wedge\mathbf{B}) \tag{2.24b}$$

Thus the particle's velocity parallel to **B** does not change, in accordance with equation (2.24a), and remains equal to it's initial value. For motion in the plane perpendicular to **B** equation (2.24b) can be written in the form

$$\frac{d\mathbf{v}_\perp}{dt} = \mathbf{v}_\perp \wedge \boldsymbol{\omega}_c, \tag{2.25}$$

where the vector $\boldsymbol{\omega}_c$ is defined by

$$\boldsymbol{\omega}_c = \frac{e\mathbf{B}}{m}.$$

The motion described by equation (2.25) is that of rotation with constant angular velocity ω_c, and can be directly integrated, noting that $\boldsymbol{\omega}_c$ is constant and taking $\mathbf{v}_\perp = d\boldsymbol{\rho}_c/dt$, to obtain

$$\mathbf{v}_\perp = \rho_c \wedge \boldsymbol{\omega}_c$$

where $\boldsymbol{\rho}_c$ is interpreted as the particle position vector with respect to the centre of gyration in the plane perpendicular to **B** which contains the particle. Thus the trajectory of the particle is given by a superposition of a uniform motion parallel to **B** and a circular motion in the plane perpendicular to **B** resulting in a helical trajectory.

The magnitude of the angular velocity vector, $\boldsymbol{\omega}_c$, is known as the cyclotron frequency or gyro-frequency. Table 2.1 gives values for the cyclotron frequency ω_c and $f_c(= |\omega_c|/2\pi)$ for electrons and protons.

Frequency	Magnetic field		
	1 Tesla	3 Tesla	5 Tesla
$\lvert\omega_{ce}\rvert$ ($\times 10^9$ rads/s)	176	528	879
ω_{ci} ($\times 10^6$ rads/s)	95.8	287	479
f_{ce} (GHz)	28.0	84.0	140
f_{ci} (MHz)	15.2	45.7	76.2

Table 2.1: Cyclotron frequency for electrons and protons in various magnetic fields.

The radius of the circular orbit is given by

$$\rho_c = \frac{v_\perp}{\omega_c} = \frac{mv_\perp}{|e|B}$$

and is referred to as the gyroradius or Larmor radius. Typical values for electrons and protons are shown in Table 2.2 for various plasma temperatures (in eV), where it is observed that $v_\perp$ contains two degrees of freedom with each contributing an energy of $\frac{1}{2}T$ giving $\frac{1}{2}mv_\perp^2 = T$.

E ∧ B Drift

Now consider a charged particle in a uniform magnetic field **B** and a perpendicular electric field **E**. (The situation where **E** is parallel to **B** is trivial.)

Magnetic field	Larmor radius	Temperature			
		10 eV	100 eV	1 keV	10 keV
3	ρ_e (μm)	3.55	11.2	35.5	112
Teslas	ρ_p (mm)	0.152	0.482	1.52	4.82
5	ρ_e (μm)	2.13	6.74	21.3	67.4
Teslas	ρ_p (mm)	0.0914	0.289	0.914	2.89

Table 2.2: Larmor radius for electrons and protons in plasmas of various temperatures.

In the absence of an electric field it was demonstrated above that the motion resolves itself into a gyratory motion around the field lines and a uniform drift along the field lines. Qualitatively it is seen that for a positive ion the effect of the perpendicular electric field is to accelerate the ion whilst travelling in the same direction as the field and to decelerate it when travelling in the opposite direction. From above it is also seen that the radius of gyration depends on the perpendicular speed of the particle, thus as the ion is accelerated it's Larmor radius increases, and conversely decreases as it is decelerated. The effect of this changing radius is to produce a drift of the centre of gyration, or guiding centre, that is perpendicular to both the magnetic and electric fields as indicated in Fig. 2.11. This drift may be quantified by returning to the

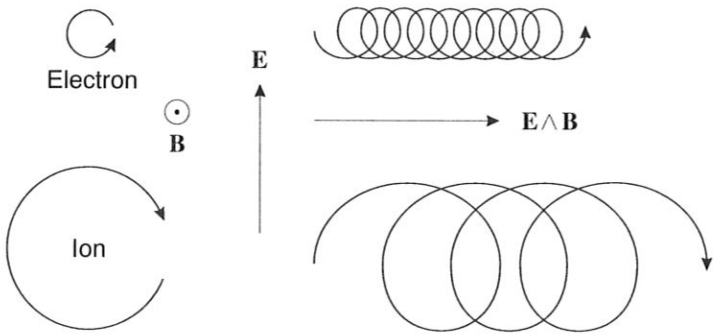

Figure 2.11: $\mathbf{E} \wedge \mathbf{B}$ drift for ions and electrons.

equation of motion, equation (2.22), and neglecting all other external fields $\mathbf{F}$. Taking the cross product with $\mathbf{B}$ gives

$$m\frac{d\mathbf{v}}{dt} \wedge \mathbf{B} = e\left[\mathbf{E} \wedge \mathbf{B} + (\mathbf{v} \cdot \mathbf{B})\,\mathbf{B} - B^2\mathbf{v}\right],$$

and averaging over one complete period gives

$$0 = e\left[\mathbf{E} \wedge \mathbf{B} - B^2\mathbf{v}_{\perp \text{ave}}\right],$$

giving

$$\mathbf{v}_{\perp \text{ave}} = \mathbf{v}_{\mathbf{E}} = \frac{\mathbf{E} \wedge \mathbf{B}}{B^2}.$$

It is interesting to note that this drift is the same for all particles, independent of mass, charge, or velocity.

Drift with External Force F

The effect of an external force $\mathbf{F}$ may be simply calculated by replacing $\mathbf{E}$ in the above derivation of the $\mathbf{E} \wedge \mathbf{B}$ drift to give

$$\mathbf{v_F} = \frac{\mathbf{F} \wedge \mathbf{B}}{eB^2}. \tag{2.26}$$

In this case it is observed that the drift depends on the charge, e, and thus ions and electrons in the plasma drift in opposite directions and give rise to a net current. A simple calculation shows however that the $\mathbf{j} \wedge \mathbf{B}$ force that this current gives rise to exactly cancels with $\mathbf{F}$.

Magnetic Moment

Due to the circular motion of a charged particle in a magnetic field there is associated with it a circulating electric current, I. The magnetic field generated by this ring current at distances much larger than the Larmor radius, ρ_c, is similar to that of a magnetic dipole. For a given magnetic field direction the ring currents of both ions and electrons flow in the same direction, even though the actual particles orbit in opposite directions. The magnetic fields generated by these currents oppose the external $\mathbf{B}$ field inside the orbits. A plasma therefore possesses diamagnetic properties. The magnetic moment of a charged particle is defined as [52]

$$\begin{aligned} \boldsymbol{\mu} &= \frac{1}{2}\int (\mathbf{r} \wedge \mathbf{j})\, d^3x = \frac{I}{2}\oint \mathbf{r} \wedge d\mathbf{l} = -\frac{1}{2} e \rho_c v_\perp \hat{\mathbf{B}} \\ &= -\frac{\frac{1}{2}mv_\perp^2}{B}\hat{\mathbf{B}} = -\frac{\mathcal{E}_\perp}{B}\hat{\mathbf{B}} \end{aligned}$$

Conservation of Magnetic Moment

The magnetic moment remains almost constant during the motion with it's invariance depending upon the slowness of the variation of B on the time scale of the particle orbit. Consider the situation of a time varying magnetic field. Faraday's law implies that this will lead to an induced electric field which can do work on the particle and change it's energy. The change in energy over one cyclotron orbit, $T = 2\pi/\omega_c$ is

$$\Delta\mathcal{E}_\perp = e\oint \mathbf{E} \cdot d\mathbf{l} = -e\int \frac{\partial \mathbf{B}}{\partial t} \cdot d\mathbf{s}.$$

If the variation is slow enough such that B is effectively constant over one orbit, then

$$\begin{aligned}\Delta\mathcal{E}_\perp &= e\pi\rho_c^2\frac{\partial \mathbf{B}}{\partial t} = \frac{\mathcal{E}_\perp}{B}T\frac{\partial \mathbf{B}}{\partial t} \\ &= \frac{\mathcal{E}_\perp}{B}\Delta B.\end{aligned}$$

This implies that

$$\Delta\left(\frac{\mathcal{E}_\perp}{B}\right) = 0 = \Delta\mu,$$

and thus the magnetic moment remains invariant as B changes. As the field strength increases, the particle moves faster in a smaller orbit and gives rise to the corollary that the magnetic flux through a gyro-orbit remains constant as the field changes. μ is said to be an adiabatic invariant.

Mirror Force

The forces and torques acting on a magnetic moment may be considered to be derived from a potential of the form [51]

$$V = -\left(\boldsymbol{\mu}\cdot\mathbf{B}\right).$$

For an individual charged particle in a plasma this implies a force of the form

$$\mathbf{F} = -\mu\nabla B$$

since it has already been remarked that μ is an adiabatic invariant and anti-parallel to $\mathbf{B}$. Inserting this force into the expression for the drift due to an external force, equation (2.26), produces the expression

$$\mathbf{v_F} = -\mu\frac{\nabla B\wedge\mathbf{B}}{eB^2} = -\mathcal{E}_\perp\frac{\nabla B\wedge\mathbf{B}}{eB^3},$$

known as the grad-B drift.

Thus as a consequence of the adiabatic invariance of μ, as a particle moves into a region of increased field strength (i.e. converging field lines) it's perpendicular velocity increases whilst it's parallel velocity decreases in order to keep μ and $\mathcal{E}$, the particle energy, constant as depicted in Fig. 2.12. If the $\mathbf{B}$ field becomes strong enough then ultimately the parallel velocity may reduce to zero and then be reversed, before the particle is accelerated in the direction of the weaker field.

Curvature Drift

In terms of the straight field line coordinates introduced in §2.4.1, there is no magnetic field curvature (by definition) and the drift which this section discusses is hidden in

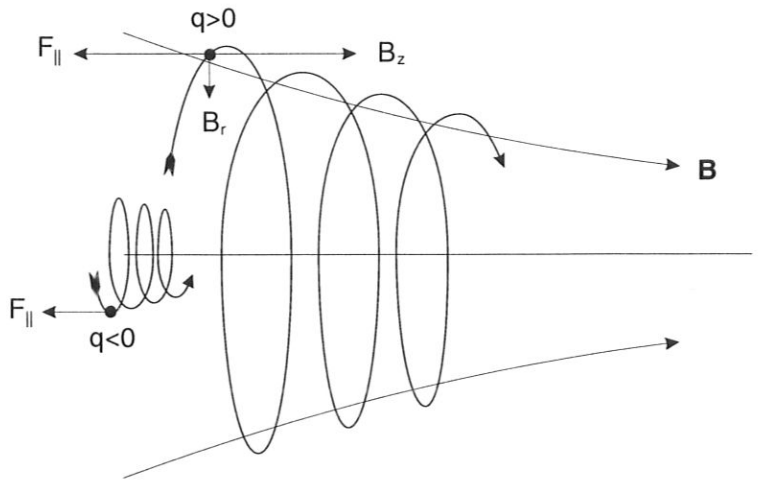

Figure 2.12: Particle reflection due to an increasing field strength.

the transformation back to a convenient laboratory reference frame. However, to understand the physical nature of particle motion in real space arising from the effects of curved magnetic field lines a local coordinate system, gliding along the magnetic field line with the same parallel velocity as the particle, is introduced. This is not an inertial coordinate system because of the curvature of the field lines which gives rise to a centripetal force of the form

$$\mathbf{F}_c = -\frac{mv_{\parallel}^2}{R^2}\mathbf{R},$$

where $\mathbf{R}$ is a vector from the instantaneous centre of curvature to the particle location. From equation (2.26) the curvature drift associated with this force is given by

$$\mathbf{v}_c = -\frac{mv_{\parallel}^2}{eB^2R^2}\mathbf{R} \wedge \mathbf{B}.$$

When currents can be neglected within the plasma, such as in a vacuum field $\nabla \wedge \mathbf{B} = 0$, the drifts due to curvature and field gradients can be combined to give a total drift of the form,

$$\mathbf{v} = \frac{4}{3}\frac{\mathcal{E}}{e}\frac{\mathbf{R} \wedge \mathbf{B}}{B^2R^2},$$

where an isotropic velocity distribution has been assumed and $\mathcal{E} = \frac{1}{2}mv^2$.

Guiding Centre Approximation

Above it was shown that the Lorentz force experienced by a charged particle moving in a magnetic field causes it to gyrate about an axis parallel to the local magnetic field

whilst the centre of gyration, or guiding centre, undergoes various drifts. If the radius of gyration, or Larmor radius, ρ, is much smaller than the scale length of any field inhomogeneity and the gyro (or Larmor) frequency is much higher than any characteristic field frequency then the guiding centre drift approximation applies. In this approach the helical trajectory of the particle in a magnetic field is approximated by a smooth drift motion as depicted in Fig. 2.13. The guiding-centre equations of motion which describe this drift motion were first developed by Alfvén in 1940 [13]. From the point of view of computationally treating the motion of a particle as an initial value problem and evolving it's position in time, this transition allows significantly larger time steps to be used since the fine scale motion associated with the particle's gyration is not explicitly followed.

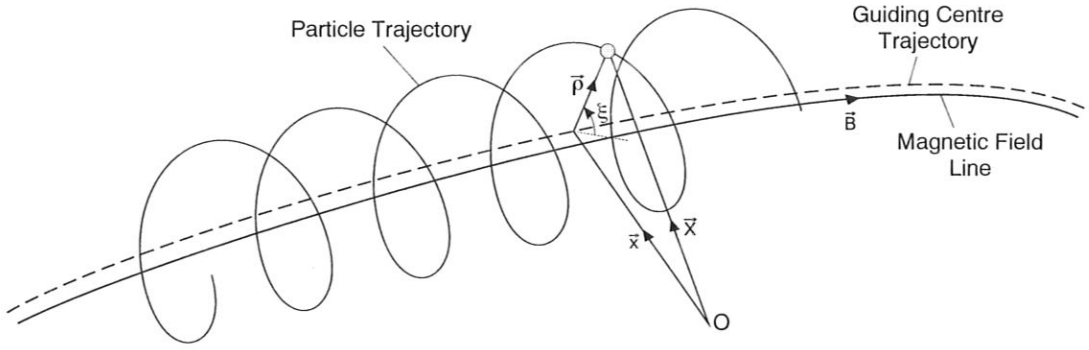

Figure 2.13: Helical trajectory of a charged particle around a field line with guiding centre trajectory indicated.

Collecting together the various drift mechanisms described above, Morozov and Solov'ev [53] have shown that the guiding centre drift velocity can be written as

$$\mathbf{v} = v_{\parallel}\hat{\mathbf{B}} + \frac{\hat{\mathbf{B}}}{eB} \wedge (mv_{\parallel}^2(\hat{\mathbf{B}} \cdot \nabla)\hat{\mathbf{B}} + \mu\nabla B + e\nabla\Phi). \tag{2.27}$$

The first term in this expression clearly represents the parallel velocity of the guiding centre along a field line, whilst the second term describes the perpendicular drift away from it. This second term may be considered to be made up of three separate parts, the first of which describes the perpendicular drift motion due to the curvature of the field lines. Particles following a curved field line experience a centripetal force which gives rise to a drift motion perpendicular to the instantaneous curvature vector and the magnetic field. The next term describes the so-called ∇B drift which occurs whenever the field strength varies. As the particle moves into a region of stronger or weaker field its Larmor radius changes and its guiding centre drifts accordingly. The final term in the above expression represents the so-called $\mathbf{E} \wedge \mathbf{B}$ drift. This is the drift away from the magnetic field lines due to the perpendicular component of the electric field.

Typical Particle Trajectories in a Tokamak

This section describes the types of particle orbit that arise in a tokamak as a result of the various drifts discussed above.

A simple application of Ampère's law indicates that the stronger toroidal field, $\mathbf{B}_t$, varies in inverse proportion to the distance from the axis of symmetry,

$$B_t = \frac{\mu_0 I_{tf}}{2\pi R},$$

where I_{tf} is the sum of the currents in the toroidal field coils. As has already been observed in §2.4.1 the magnetic field lines lie on nested surfaces of constant flux, ψ, and slowly spiral around these surface. Without the smaller poloidal field, a vertical drift would occur in opposite directions for the ions and electrons. This leads to charge separation and subsequently a vertical electric field giving rise to an $\mathbf{E} \wedge \mathbf{B}$ drift in the radial direction. This would then lead to an unacceptable loss of particles from the confinement system. By adding a small poloidal field the particles still primarily follow the field lines, but they now traverse the entire poloidal cross section before returning close to where they started. Each species still has a vertical drift associated with it but this now cancels in the upper and lower halves of the torus with the effect that there is no net drift.

The curvature of the field lines and the variation in the field strength leads to various distinct classes of particles which can be divided into two main classes; trapped and passing particles, as shown in Fig. 2.14.

The trapped particles have insufficient parallel kinetic energy compared with their perpendicular energy to penetrate into the high-field side of the torus and are consequently located in the outer low-field side of the tokamak. They bounce backwards and forwards between their mirror points experiencing a continual vertical drift due to the combined effects of field curvature and gradient. When projected into a poloidal plane the trajectories traced out by these particles earn them the appropriate name of banana orbits.

Passing particles are not reflected anywhere and spiral around the torus following the helical path of the field lines. Like the trapped particles they also experience a continual vertical ∇B and curvature drift independent of their direction of travel around the tokamak. This results in co-passing and counter-passing (particles travelling with and against the field) appearing to drift radially inwards or outwards depending on the direction of the plasma current.

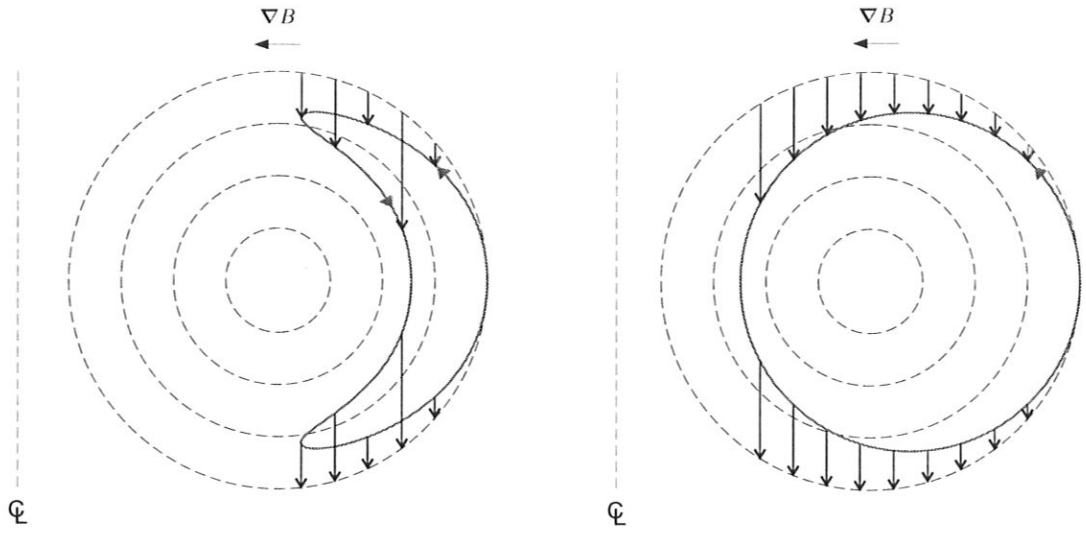

Figure 2.14: Poloidal projection of typical charged particle orbits in a tokamak. The particles experience a vertical drift dependent upon their velocity parallel to the magnetic field.

Chapter 3

Development of Model

The theoretical background material presented in the previous chapter enables a numerical model to be developed to examine the interaction of fast particles with Alfvén eigenmodes supported by the system. A schematic overview of the problem is presented in Fig. 3.1. As can be seen the plasma equilibrium is responsible for determining the AE supported, as well as the specifics of the particle trajectories which may be simplified through the adoption of a guiding centre approach. The wave-particle interactions that take place lead to a modification of the fast particle distribution function which in turn affects the wave-particle interactions that occur.

The task of obtaining the guiding centre equations of motion can be simplified by adopting a Hamiltonian formalism as indicated in §2.4. The specific form of the Hamiltonian, and therefore the equations of motion to which it gives rise, depends upon the canonical coordinates used. The crux for finding simple canonical variables lies in the proper choice of the spatial coordinates which should be suited to the geometry of the magnetic field. From the point of view of describing the waves present, all that is needed is the adoption of a set of flux coordinates since it is natural to decompose the waves into Fourier harmonics in the toroidal and poloidal directions.

Littlejohn [56] has shown that the guiding centre Lagrangian may be written as,

$$\mathcal{L} = e\left(\mathbf{A} + \frac{v_{\parallel}}{\omega_c}\mathbf{B}\right)\cdot\dot{\mathbf{x}} + \frac{m}{e}\mu\dot{\xi} - \mathcal{H},$$

where $\mathcal{H}$ is the guiding centre Hamiltonian and $\mathbf{x}$ and ξ are the guiding centre position and gyro-phase respectively as shown in Fig: 2.13. This implies that the canonical variables satisfy the relation,

$$p_i\dot{q}_i = e\left(\mathbf{A} + \frac{v_{\parallel}}{\omega_c}\mathbf{B}\right)\cdot\dot{\mathbf{x}} + \frac{m}{e}\mu\dot{\xi}.$$

Due to the Lagrangian's scalar nature it guarantees general covariance and allows any coordinate system to be used. The easiest way to express the velocity term in this

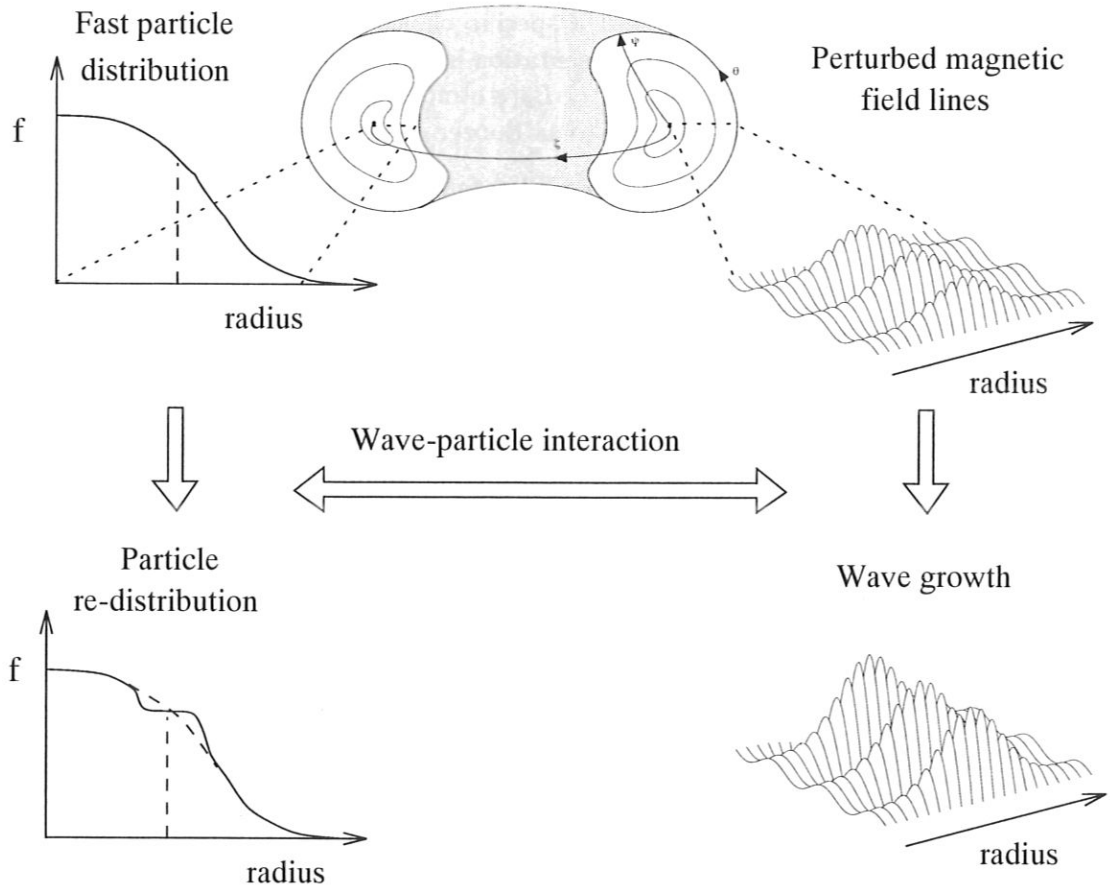

Figure 3.1: Schematic diagram showing an overview of the model. The plasma equilibrium determines the AE supported by the system as well as the topology of the particle orbits. The distribution of fast particles interacts with the waves changing their amplitudes and phases whilst causing a re-distribution of the fast particles.

equation is in contravariant form,

$$\dot{\mathbf{x}} = \dot{\xi}^i \frac{\partial \mathbf{x}}{\partial \xi^i},$$

then by expressing $\mathbf{A}$ and $\mathbf{B}$ in covariant form any components of the metric tensor arising from the dot product with $\dot{\mathbf{x}}$ are avoided. It has already been demonstrated in §2.4.1 that for any straight field line coordinates the covariant components of $\mathbf{A}$ are flux functions. Thus by seeking a specific straight field line coordinate system that allows $\mathbf{B}$ to be expressed in covariant form, with as many components as possible being flux functions, enables the description to be characterized by the flux label ψ.

3.1 Boozer Coordinates

In the early 1980s Boozer [50, 57] used a specific choice of Jacobian to successfully obtain a covariant straight field line representation in which the angular covariant field components were flux functions. ie. $B_\theta = B_\theta(\psi)$ and $B_\zeta = B_\zeta(\psi)$. In the literature such coordinates are sometimes referred to as Boozer coordinates.

When introducing straight field line coordinate systems in §2.4.1 it was assumed that the system under consideration was in scalar pressure equilibrium and from this the existence of nested flux surfaces was postulated. This assumption may be re-examined by noting that due to it's solenoidal nature the magnetic field line flow is incompressible, resembling the flow in phase-space of a Hamiltonian system. If the magnetic field has a continuous symmetry such as toroidal symmetry ($\partial\mathbf{B}/\partial\zeta = 0$ with ζ the toroidal angle), the field lines reduce to an integrable Hamiltonian form. In the absence of any such ignorable coordinates Yoshida [58] has shown that the flux coordinate form for representing a magnetic field in scalar pressure equilibrium, such as that developed above, can be generalized to represent any solenoidal field in a toroidal domain by writing it in the form

$$\mathbf{B} = \nabla\psi \wedge \nabla\theta + \nabla\zeta \wedge \nabla\Psi_p(\psi, \theta, \zeta). \tag{3.1}$$

It is in this form that Boozer represents an arbitrary magnetic field $\mathbf{B}(\mathbf{x})$. In the case of a field with perfect surfaces one can choose ψ, θ, and ζ so that Ψ_p is a function of ψ alone and thereby recover the flux coordinate representation. However for a field with a complex topology such that it cannot be described by a set of nested flux surfaces no such ψ, θ, and ζ exist and Ψ_p must be considered a function of all three coordinates [57].

The field lines are defined by the equations

$$\frac{d\psi}{d\zeta} = \frac{\mathbf{B}\cdot\nabla\psi}{\mathbf{B}\cdot\nabla\zeta}, \qquad \frac{d\theta}{d\zeta} = \frac{\mathbf{B}\cdot\nabla\theta}{\mathbf{B}\cdot\nabla\zeta}, \tag{3.2}$$

which upon substituting for equation (3.1) become

$$\frac{d\psi}{d\zeta} = -\frac{\partial\Psi_p}{\partial\theta}, \qquad \frac{d\theta}{d\zeta} = \frac{\partial\Psi_p}{\partial\psi},$$

where the poloidal flux function $\Psi_p(\psi, \theta, \zeta)$ is identified as the field-line Hamiltonian, with θ, ψ and ζ playing the rôles of position, momentum and time, respectively.

The existence of exact surfaces is equivalent to the Hamiltonian Ψ_p having a non-trivial constant of the motion. If the Hamiltonian is independent of θ it's canonically conjugate momentum ψ is a constant of the motion.

$$\Psi_p = \mathcal{H}(\psi) \Rightarrow \frac{\partial\Psi_p}{\partial\theta} = 0 \Rightarrow \Psi_p = const. \text{ along a field line.}$$

In the absence of a constant of the motion one cannot choose ψ, θ, ζ to make Ψ_p a function of ψ alone. However if there is a nearby field with good surfaces one can choose Ψ_p so that

$$\Psi_p(\psi, \theta, \zeta) = \psi_p(\psi) + \hat{\psi}(\psi, \theta, \zeta),$$

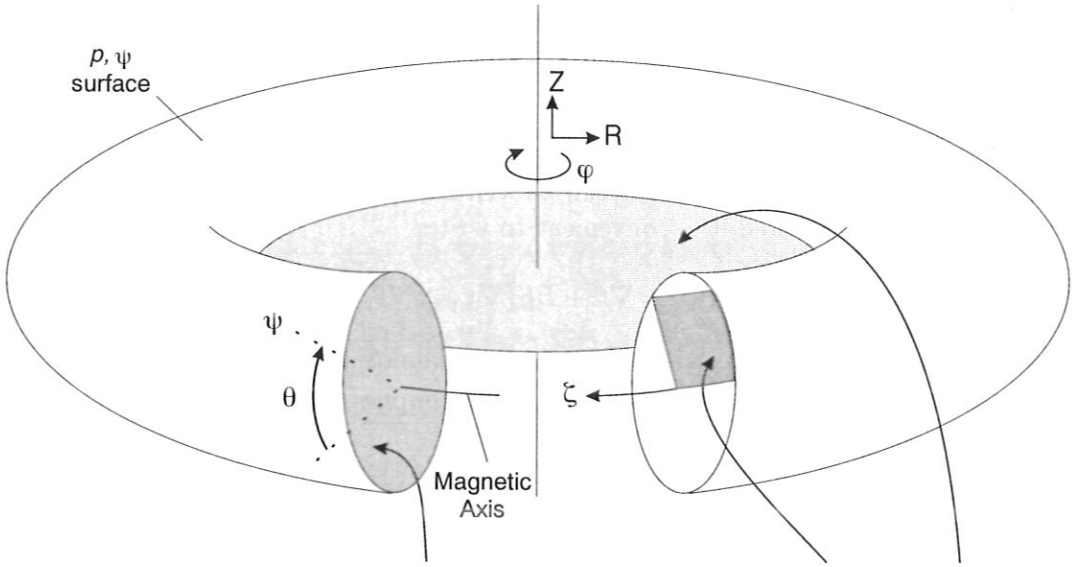

$$2\pi\psi = \int \mathbf{B}\cdot d\mathbf{s}_t \qquad 2\pi\psi_p = \int \mathbf{B}\cdot d\mathbf{s}_r = -\int \mathbf{B}\cdot d\mathbf{s}_p$$
$$2\pi I = \int (\nabla\wedge\mathbf{B})\cdot d\mathbf{s}_t \qquad 2\pi g = -\int (\nabla\wedge\mathbf{B})\cdot d\mathbf{s}_p$$

Figure 3.2: The toroidal flux ψ, the poloidal flux ψ_p, the toroidal current I, and the poloidal current g, are defined by integrals over the two enclosed areas of the torus.

with $|\hat{\psi}| \ll |\psi_p|$.

By only considering systems for which it is assumed that good magnetic surfaces exist, $\Psi_p(\psi,\theta,\zeta)$ can be replaced by $\psi_p(\psi)$ and ψ,θ,ζ, and ψ_p can be interpreted as given in Fig. 3.2. The coordinate ψ represents the toroidal flux inside a magnetic surface and ψ_p can be interpreted as the poloidal flux outside a magnetic surface, or poloidal flux through a closed ribbon-like surface bounded by the magnetic axis and a magnetic surface. These two interpretations are equivalent, with the two definitions of ψ_p differing only by a constant.

In the discussion of tokamak field representations in this section it has been possible to progress from completely general field representations to those possessing nested flux surfaces by assuming that a nearby field configuration with good surfaces exists. Making the further assumption that this adjacent representation is toroidally symmetric allows the adoption of the Boozer coordinate system used by White & Chance [54]. This combines the advantages of using a straight field line representation, enabling the fast streaming of particles along the field lines to be separated from the slow perpendicular drift, with the property that the magnetic field components required to describe the particle motion are functions of ψ_p alone. The coordinate system takes ψ_p as the radial coordinate and deforms the toroidal angle coordinate ζ to obtain straight field lines. The general poloidal angle is chosen by selecting a specific form for the Jacobian

to obtain a covariant representation of the magnetic field in which the angular components are functions of the poloidal flux alone. Toroidal symmetry implies that all equilibrium quantities such as the metric tensor and field components are independent of the azimuthal angle ζ.

By observing that $\mathbf{B}\cdot\nabla\psi_p = 0$, $\mathbf{B}$ can be written using any two vectors orthogonal to $\nabla\psi_p$, Greene [59] showed it is convenient to write

$$\mathbf{B} = B_H\nabla\psi_p\wedge\nabla\theta + B_O(\nabla\psi_p\wedge\nabla\theta)\wedge\nabla\psi_p, \tag{3.3}$$

where B_H and B_O are functions of ψ_p and θ to be determined. From $\nabla\cdot\mathbf{B} = 0$, it is found that $\nabla\cdot[B_O(\nabla\psi_p\wedge\nabla\theta)\wedge\nabla\psi_p] = 0$, which implies

$$\frac{\partial}{\partial\theta}\left[\mathcal{J}B_O(\nabla\psi_p\wedge\nabla\theta)^2\right] = 0, \quad \Rightarrow \quad B_O = \frac{\Gamma(\psi_p)}{\mathcal{J}(\nabla\psi_p\wedge\nabla\theta)^2}, \tag{3.4}$$

for some flux label $\Gamma(\psi_p)$.

Equilibrium force balance implies that the plasma current flows in a magnetic surface since $\mathbf{j}\cdot\nabla\psi_p = 0$ provided $p'\neq 0$. Using $(\nabla\wedge\mathbf{B})\cdot\nabla\psi_p = \nabla\cdot(\mathbf{B}\wedge\nabla\psi_p) = 0$ it is found on substituting for $\mathbf{B}$ from equation (3.3) that

$$\frac{\partial}{\partial\theta}\left[\mathcal{J}B_H(\nabla\psi_p\wedge\nabla\theta)^2\right] = 0, \quad \Rightarrow \quad B_H = \frac{g(\psi_p)}{\mathcal{J}(\nabla\psi_p\wedge\nabla\theta)^2}, \tag{3.5}$$

for some flux label $g(\psi_p)$.

Equations (3.4) and (3.5) allow equation (3.3) to be rewritten as

$$\mathbf{B} = \frac{1}{\mathcal{J}(\nabla\psi_p\wedge\nabla\theta)^2}\left[g(\psi_p)(\nabla\psi_p\wedge\nabla\theta) + \Gamma(\psi_p)(\nabla\psi_p\wedge\nabla\theta)\wedge\nabla\psi_p\right]. \tag{3.6}$$

Choosing $2\pi\psi_p$ to be the poloidal flux inside the surface labelled by ψ_p implies that

$$2\pi\psi_p = \frac{1}{2\pi}\iiint(\mathbf{B}\cdot\nabla\theta)\,\mathcal{J}\,d\psi_p\,d\theta\,d\zeta.$$

But from equation (3.6),

$$\mathbf{B}\cdot\nabla\theta = \frac{\Gamma(\psi_p)}{\mathcal{J}},$$

so

$$\begin{aligned} 2\pi\psi_p &= \frac{1}{2\pi}\iiint\Gamma(\psi_p)\,d\psi_p\,d\theta\,d\zeta, \\ &= 2\pi\int\Gamma(\psi_p)\,d\psi_p, \end{aligned}$$

and hence $\Gamma(\psi_p) = 1$.

Using the usual notation, the covariant form for $\mathbf{B}$ can be written

$$\mathbf{B} = B_{\psi_p}\nabla\psi_p + B_\theta\nabla\theta + B_\zeta\nabla\zeta,$$

where the covariant components are found by taking the scalar product of equation (3.6) with the appropriate contravariant basis vectors to give,

$$B_{\psi_p} = \frac{1}{(\nabla\psi_p\wedge\nabla\theta)^2}\left[g(\nabla\psi_p\wedge\nabla\theta)\cdot(\nabla\theta\wedge\nabla\zeta) - \frac{(\nabla\psi_p\cdot\nabla\theta)}{\mathcal{J}}\right], \quad (3.7a)$$

$$B_\theta = \frac{1}{(\nabla\psi_p\wedge\nabla\theta)^2}\left[g(\nabla\psi_p\wedge\nabla\theta)\cdot(\nabla\zeta\wedge\nabla\psi_p) + \frac{(\nabla\psi_p)^2}{\mathcal{J}}\right], \quad (3.7b)$$

$$B_\zeta = g. \quad (3.7c)$$

The coordinate ζ is chosen so that the field lines are straight in the θ,ζ plane, ie. the local helicity $(\mathbf{B}\cdot\nabla\zeta)/(\mathbf{B}\cdot\nabla\theta) \equiv B^\zeta/B^\theta \equiv q(\psi_p)$ is taken to be independent of θ. Calculating the ζ and θ contravariant components of the field it is found that

$$B^\zeta = \mathbf{B}\cdot\nabla\zeta = \frac{1}{\mathcal{J}(\nabla\psi_p\wedge\nabla\theta)^2}\left[\frac{g}{\mathcal{J}} + \{(\nabla\psi_p\wedge\nabla\theta)\wedge\nabla\psi_p\}\cdot\nabla\zeta\right],$$

$$B^\theta = \mathbf{B}\cdot\nabla\theta = \frac{1}{\mathcal{J}}.$$

Thus in coordinates in which the field lines are straight,

$$(\nabla\psi_p\wedge\nabla\theta)\cdot(\nabla\zeta\wedge\nabla\psi_p) = \frac{g}{\mathcal{J}} - q(\nabla\psi_p\wedge\nabla\theta)^2. \quad (3.8)$$

Now, $B^2 = B_{\psi_p}B^{\psi_p} + B_\theta B^\theta + B_\zeta B^\zeta$ which gives,

$$B^2 = \frac{1}{\mathcal{J}^2(\nabla\psi_p\wedge\nabla\theta)^2}\left[(\nabla\psi_p)^2 + g^2\right]. \quad (3.9)$$

Substituting equation (3.9) into equation (3.7b), and using equation (3.8) gives,

$$B_\theta = \mathcal{J}B^2 - gq.$$

Calculating the toroidal flux within the flux surface ψ_p, it is found that

$$2\pi\psi = \frac{1}{2\pi}\iiint(\mathbf{B}\cdot\nabla\zeta)\,\mathcal{J}\,d\psi_p\,d\theta\,d\zeta,$$

$$= \frac{1}{2\pi}\iiint q(\psi_p)\,d\psi_p\,d\theta\,d\zeta,$$

giving $\psi = \int q(\psi_p)\,d\psi_p$, or $d\psi/d\psi_p = q(\psi_p)$. Thus in a coordinate system with straight field lines ψ is a function of ψ_p alone, both being constant on a magnetic surface.

The contravariant form of $\mathbf{B}$ may now be written as

$$\mathbf{B} = \nabla\zeta\wedge\nabla\psi_p + q\nabla\psi_p\wedge\nabla\theta, \quad (3.10a)$$

$$= \nabla(\zeta - q(\psi_p)\theta)\wedge\nabla\psi_p, \quad (3.10b)$$

from which it follows that the vector potential $\mathbf{A}$ can be written as

$$\mathbf{A} = \psi \nabla\theta - \psi_p \nabla\zeta. \tag{3.11}$$

This contravariant form for $\mathbf{B}$ is seen to be the same as that given in equation (2.21), with $u(\psi) = d\psi_t/d\psi_p = q$, and $v(\psi) = d\psi_p/d\psi_p = 1$.

Introducing δ to represent the radial covariant component of $\mathbf{B}$, the covariant representation becomes,

$$\mathbf{B} = \delta(\psi_p, \theta)\nabla\psi_p + (\mathcal{J}B^2 - qg)\nabla\theta + g(\psi_p)\nabla\zeta,$$

which if the Jacobian is chosen to be of the form $\mathcal{J} = \mathcal{F}(\psi_p)/B^2$, ensures that B_θ is a flux function since $B_\theta = \mathcal{F}(\psi_p) - g(\psi_p)q(\psi_p) \equiv I(\psi_p)$. The final covariant form thus becomes,

$$\mathbf{B} = \delta(\psi_p, \theta)\nabla\psi_p + I(\psi_p)\nabla\theta + g(\psi_p)\nabla\zeta, \tag{3.12}$$

with

$$\mathcal{J} = \frac{I + gq}{B^2}. \tag{3.13}$$

The dependence of the angular covariant components I and g on ψ_p alone arises from the choice of Jacobian and is an important ingredient in the development of the Hamiltonian formulation. The radial covariant component δ can be found from $\mathbf{B} \cdot \nabla\psi_p = 0$ giving

$$\delta(\psi_p, \theta) = -\frac{I\nabla\theta \cdot \nabla\psi_p + g\nabla\zeta \cdot \nabla\psi_p}{|\nabla\psi_p|^2} = -\frac{I\mathrm{g}^{12} + g\mathrm{g}^{13}}{\mathrm{g}^{11}},$$

where the superscripted terms g^{ij} represent the contravariant components of the metric tensor $\overleftrightarrow{\mathbf{g}}$ and the triplet ordering is (ψ_p, θ, ζ). As may be seen, δ is related to the degree of non-orthogonality of the system and is very small for equilibria with nearly circular cross-section.

Simple physical interpretations can be found for the functions $I(\psi_p)$ and $g(\psi_p)$ in terms of the currents flowing in the device. Using the covariant expression for $\mathbf{B}$ allows the current density $\mathbf{j}$ to be written as,

$$\mathbf{j} = \frac{1}{\mu_0}\left(\frac{\partial\delta}{\partial\theta}\nabla\theta \wedge \nabla\psi_p + \frac{\partial I}{\partial\psi_p}\nabla\psi_p \wedge \nabla\theta + \frac{\partial g}{\partial\psi_p}\nabla\psi_p \wedge \nabla\zeta\right).$$

Integrating this expression separately over the poloidal and toroidal areas as defined in Fig. 3.2 reveals that $2\pi I/\mu_0$ is the total toroidal current inside the flux surface ψ_p and that $2\pi g/\mu_0$ is the poloidal current.

3.2 Guiding Centre Equations

In this section the steps leading up to the derivation of the guiding centre equations of motion are outlined. The guiding centre Lagrangian is obtained from that for a free charged particle in an electromagnetic field through a gyro-averaging procedure [56] and the canonical variables identified. As a consequence of the gyro-averaging process the phase-space of the problem is reduced, lowering the number of variables that must be evolved. The equations of motion follow by differentiating the guiding centre Hamiltonian with respect to these canonical variables.

The Boozer coordinate system introduced in the last section may in general form a non-inertial reference frame since it is defined with respect to the magnetic field structure which may be time dependent. Using a Lagrangian approach allows a transformation from an inertial laboratory reference frame to a set of non-inertial coordinates describing a time dependent magnetic field. Consider the exact particle Lagrangian in a stationary reference frame,

$$\mathcal{L} = \frac{1}{2}mV^2 + e\mathbf{V}\cdot\mathbf{A}_S - e\Phi_S, \tag{3.14}$$

where $\mathbf{V}$, Φ_S, and $\mathbf{A}_S$, represent the exact particle velocity, $\mathbf{V} = d\mathbf{x}/dt$, and the scalar and vector potentials in this reference frame.

If the magnetic field is time dependent the exact particle velocity can be written as

$$\mathbf{V} = \frac{\partial \mathbf{x}}{\partial t} + \frac{\partial \mathbf{x}}{\partial \xi^i}\dot{\xi}^i$$

using the transformation equations $\mathbf{x}(\psi, \theta, \zeta, t)$ where $\xi^1 = \psi$, $\xi^2 = \theta$, and $\xi^3 = \zeta$. The first term in this expression represents the velocity of the magnetic field, $\mathbf{V}_B$ say, and the second term is the velocity of the particle relative to the magnetic field in contravariant form, $\mathbf{v}$ say. The exact Lagrangian in terms of the particle's velocity may be written in the same form as that given in equation (3.14) by defining,

$$\mathbf{A} = \mathbf{A}_S + \left(\frac{m}{e}\right)\mathbf{V}_B, \quad \text{and} \quad \Phi = \Phi_S - \mathbf{A}_S\cdot\mathbf{V}_B - \frac{1}{2}\left(\frac{m}{e}\right)V_B^2,$$

to give

$$\mathcal{L} = \frac{1}{2}mv^2 + e\mathbf{A}\cdot\mathbf{v} - e\Phi.$$

Recalling that the Larmor radius may be expressed as $\rho = mv_\perp/eB$ and that $\mathbf{B} = \nabla\wedge\mathbf{A}$ implying $B \approx A/L$ where L is a typical scale length upon which the field varies, allows the relative magnitudes of the latter two terms in each of these definitions to be considered:

$$\frac{|m\mathbf{V}_B|}{|e\mathbf{A}_S|} \simeq \frac{V_B}{V}\frac{\rho}{L},$$

where V is a typical particle velocity. As a consequence of both V_B/V and ρ/L being small it can be assumed that $\mathbf{A} = \mathbf{A}_S$ and the final term in the expression for the

electric potential Φ may be neglected leaving $\Phi = \Phi_S - \mathbf{A}_S \cdot \mathbf{V}_B$. Further assuming the exact invariance of the magnetic moment, $\mu = mv_\perp^2/2B$, it effectively becomes an 'internal' process analogous to electron spin and is coupled to the external degrees of freedom by means of the mirror force, $\mathbf{F}_m = -\nabla(\mu B)$. This suggests the interpretation of μB as a potential energy term rather than a kinetic one and allows the Lagrangian to be written in the form first given by Taylor [60],

$$\mathcal{L} = \frac{1}{2}mv_\parallel^2 + e\,\mathbf{A}\cdot\mathbf{v} - \mu B - e\Phi.$$

The Euler-Lagrange equations obtained from this Lagrangian are degenerate since this Lagrangian depends only linearly on the components of the guiding centre velocity perpendicular to $\mathbf{B}$. This implies the equations of motion in these perpendicular directions are first order in time and serve merely to define the perpendicular drift velocity in terms of the guiding centre position. Attempting to construct a Hamiltonian description reveals the same degeneracy seen through the definition of the canonical momenta,

$$\mathbf{p} = \frac{\partial \mathcal{L}}{\partial \dot{\mathbf{x}}} = mv_\parallel \hat{\mathbf{B}} + e\mathbf{A},$$

where $\hat{\mathbf{B}}$ is a unit vector parallel to $\mathbf{B}$. This indicates that the two components of $\mathbf{p}$ perpendicular to $\hat{\mathbf{B}}$ are simply functions of $\mathbf{x}$ since

$$\mathbf{p}_\perp = e\mathbf{A}_\perp.$$

Thus, although the Hamiltonian

$$\mathcal{H}(\mathbf{x}, \mathbf{p}, t) = p_i \frac{dx_i}{dt} - \mathcal{L}(\mathbf{x}, \dot{\mathbf{x}}, t),$$

appears to depend on six phase-space coordinates, only four are independent. This four-dimensional phase-space of independent coordinates is called the 'reduced' phase-space and consists of the parallel velocity $v_\parallel$ and the three components of the spatial position of the guiding centre $\mathbf{x}$. The dependence on only four variables instead of six has arisen because the magnetic moment μ, which is determined by $v_\perp$, has been assumed to be conserved. The gyro-phase, which is the coordinate conjugate to μ and rotates at the gyro-frequency, is irrelevant to the guiding centre motion.

Suitable canonical variables were initially found [54, 61] by a rather laborious procedure involving trying to find the time variation of a particular coordinate, q_i say, whilst following the guiding centre position. This meant demonstrating that $\dot{q}_i = \mathbf{v}\cdot\nabla q_i = \partial\mathcal{H}/\partial p_i$, where the Hamiltonian $\mathcal{H}$ is the total energy of the system expressed in terms of the canonical variables and $\mathbf{v}$ is the guiding centre drift velocity given in equation (2.27). By adopting a Lagrangian approach, Littlejohn [56] was able to considerably reduce the labour involved in finding a reduced set of guiding centre canonical variables. The procedure used is based upon Hamilton's variational principle which may be written as

$$\delta\int \mathcal{L}\,dt = 0,$$

with the guiding centre Lagrangian, $\mathcal{L}$, given by [56]

$$\mathcal{L} = e\mathbf{A}^* \cdot \dot{\mathbf{x}} + \frac{m}{e}\mu\dot{\xi} - \mathcal{H}, \tag{3.15}$$

where ξ is the gyro-phase and $\dot{\mathbf{x}}$ is the guiding centre velocity and represents the total time derivative of the guiding centre location, $\mathbf{x}$. The term $\mathbf{A}^* = \mathbf{A} + \rho_{\|}\mathbf{B}$ is known as the 'modified vector potential' and was first used by Morozov & Solov'ev in 1963 [53]. It makes use of $\rho_{\|} = v_{\|}/\omega_{ci}$ which is referred to as the parallel gyroradius, with the Hamiltonian given by

$$\mathcal{H} = \frac{1}{2}mv_{\|}^2 + \mu B + e\Phi. \tag{3.16}$$

It is convenient to choose units based around characteristic system quantities. Since the case being examined is the interaction of a distribution of fast particles with a perturbed magnetic field it is appropriate to express all masses and charges in terms of those of the fast particles and to express all lengths in terms of the toroidal major radius at the magnetic axis. Time units are specified in terms of the inverse fast particle cyclotron time at the magnetic axis, $1/\Omega_0 = 1/B_0$ in these units. Since we only consider a single species of fast particle we may subsequently omit all occurrences of charge and mass in the following formulae. Physical formulae consequently result by restoring these physical factors.

Canonical variables are obtained by substituting expressions for $\mathbf{A}$ and $\mathbf{B}$ into equation (3.15) and rewriting it as

$$\mathcal{L} = \sum_i p_i\dot{q}_i - \mathcal{H}.$$

Once this form is obtained, the canonical momenta and coordinates can immediately be identified. Substituting equations (3.11) and (3.12) for $\mathbf{A}$ and $\mathbf{B}$ into the Lagrangian gives

$$\mathcal{L} = \left(\rho_{\|}I + \psi\right)\dot{\theta} + \left(\rho_{\|}g - \psi_p\right)\dot{\zeta} + \mu\dot{\xi} - \mathcal{H} + \delta\rho_{\|}\dot{\psi}_p \tag{3.17}$$

As already noted any coordinate system may be used, provided it labels all configurations of the system. It is thus natural to select the Boozer coordinates introduced in §3.1 to form the canonical coordinates, enabling the canonically conjugate momentum variables to be read straight from equation (3.17). Upon closer inspection however there are seen to be four terms of the form $p_i\dot{q}_i$. To resolve this, ψ_p is viewed as a momentum term and consequently the final term interferes with this interpretation and must be removed.

One method of achieving this involves the observation that the equations of motion remain invariant under the addition of exact differentials to the Lagrangian [52]. Thus terms such as $d(\delta\rho_{\|}\psi)/dt$ may be safely subtracted from equation (3.17) with no effect and the remaining terms absorbed into the canonical coordinates θ and ζ through their redefinition, or neglected if they are higher order in ρ [54, 62]. This approach

is unsatisfactory however, since the resulting canonical coordinates no longer coincide with the Boozer magnetic coordinates derived above and also since the equations of motion that ensue do not exactly conserve $\mathcal{H}$. A more desirable approach is one that whilst only reproducing particle motion to second order in ρ, exactly conserves the Hamiltonian. This is achievable by a modification of the guiding centre velocity $\dot{\mathbf{x}} = \mathbf{v}$, so that $\mathbf{v} \longrightarrow \mathbf{v} + \mathbf{w}$. This adds an additional term to equation (3.17) of the form $\mathbf{A}^* \cdot \mathbf{w}$, where $\mathbf{w}$ may be chosen such that

$$\mathbf{A}^* \cdot \mathbf{w} = -\delta\rho_{\|}\dot{\psi}_p. \tag{3.18}$$

With this choice the reduced set of canonical coordinates are θ, ζ and ξ, with the corresponding canonical momenta given by

$$\begin{aligned} P_\theta &= \rho_{\|} I + \psi, \\ P_\zeta &= \rho_{\|} g - \psi_p, \\ P_\xi &= \mu, \end{aligned}$$

and the equations of motion following from the Hamiltonian in the usual manner,

$$\begin{aligned} \dot{\theta} &= \frac{\partial \mathcal{H}}{\partial P_\theta}, & \dot{P}_\theta &= -\frac{\partial \mathcal{H}}{\partial \theta}, \\ \dot{\zeta} &= \frac{\partial \mathcal{H}}{\partial P_\zeta}, & \dot{P}_\zeta &= -\frac{\partial \mathcal{H}}{\partial \zeta}, \\ \dot{\xi} &= \frac{\partial \mathcal{H}}{\partial P_\xi}, & \dot{P}_\xi &= -\frac{\partial \mathcal{H}}{\partial \xi}. \end{aligned} \tag{3.19}$$

Before proceeding to derive the equations of motion that follow from equations (3.19) consider the inclusion of a general electromagnetic perturbation described by the vector and scalar potentials,

$$\tilde{\mathbf{A}}(\mathbf{x}, t) = \tilde{A}_{\psi_p} \nabla\psi_p + \tilde{A}_\theta \nabla\theta + \tilde{A}_\zeta \nabla\zeta, \quad \text{and} \quad \tilde{\Phi}(\mathbf{x}, t).$$

Replacing $\mathbf{A}$ with $\mathbf{A} + \tilde{\mathbf{A}}$, and Φ with $\Phi + \tilde{\Phi}$, means that the Lagrangian now becomes,

$$\mathcal{L} = \left(\rho_{\|} I + \psi + \tilde{A}_\theta\right)\dot{\theta} + \left(\rho_{\|} g - \psi_p + \tilde{A}_\zeta\right)\dot{\zeta} + \mu\dot{\xi} - \mathcal{H} + \left(\delta\rho_{\|} + \tilde{A}_{\psi_p}\right)\dot{\psi}_p. \tag{3.20}$$

The final term in this Lagrangian is treated as before and the canonical variables are now modified such that the canonical momenta are,

$$P_\theta = \rho_{\|} I + \psi + \tilde{A}_\theta, \tag{3.21a}$$

$$P_\zeta = \rho_{\|} g - \psi_p + \tilde{A}_\zeta, \tag{3.21b}$$

$$P_\xi = \mu. \tag{3.21c}$$

Examining these equations it is reassuring to observe that they are of the same structure as a free particle in classical electrodynamics for which the canonical momenta $\mathbf{P} = \mathbf{p} + \mathbf{A}$, where $\mathbf{p}$ is the familiar mechanical momentum. This is seen from equation (3.11) where it is observed that ψ and $-\psi_p$ are the θ and ζ covariant components of $\mathbf{A}$. Noting that $\rho_{||}\mathbf{B}$ is the parallel momentum it follows from equation (3.12) that the particle momenta corresponding to θ and ζ are $\rho_{||}I$ and $\rho_{||}g$.

The Hamiltonian for this system is the total energy and is therefore given by equation (3.16). Interpreting $\rho_{||}$ as the normalised parallel velocity (since $m = e = 1$ in the units adopted here) the Hamiltonian can be re-written as

$$\mathcal{H} = \frac{1}{2}\rho_{||}^2 B^2 + \mu B + \tilde{\Phi}.$$

where the possibility of an equilibrium electrostatic potential $\Phi(\mathbf{x})$ has been excluded since it would immediately be shorted out by the very mobile electrons present.

The equations of motion may now be evaluated in accordance with equations (3.19). Since $\mathcal{H}$ is not written in terms of the canonical momenta this first involves evaluating the partial derivatives of ψ_p and $\rho_{||}$ with respect to the canonical variables. Recalling that g, I, and ψ are all functions of ψ_p alone, equations (3.21) give that $\psi_p = \psi_p(\theta, \zeta, P_\theta, P_\zeta)$ and that $\rho_{||} = \rho_{||}(\theta, \zeta, P_\theta, P_\zeta)$. Eliminating $\rho_{||}$ from the first two of these equations gives

$$g\left(P_\theta - \psi - \tilde{A}_\theta\right) = I\left(P_\zeta + \psi_p - \tilde{A}_\zeta\right).$$

Differentiating this expression with respect to θ, ζ, P_θ and P_ζ gives

$$\frac{\partial \psi_p}{\partial \theta} = \frac{1}{D}\left[I\frac{\partial \tilde{A}_\zeta}{\partial \theta} - g\frac{\partial \tilde{A}_\theta}{\partial \theta}\right], \tag{3.22a}$$

$$\frac{\partial \psi_p}{\partial \zeta} = \frac{1}{D}\left[I\frac{\partial \tilde{A}_\zeta}{\partial \zeta} - g\frac{\partial \tilde{A}_\theta}{\partial \zeta}\right], \tag{3.22b}$$

$$\frac{\partial \psi_p}{\partial P_\theta} = \frac{g}{D}, \tag{3.22c}$$

$$\frac{\partial \psi_p}{\partial P_\zeta} = -\frac{I}{D}, \tag{3.22d}$$

where

$$D = \rho_{||}[gI' - g'I] + I + qg - I\tilde{A}'_\zeta + g\tilde{A}'_\theta,$$

with primes referring to differentiation with respect to ψ_p.

Differentiating equations (3.21a) and (3.21b) with respect to θ, ζ, P_θ and P_ζ gives

$$\frac{\partial \rho_{||}}{\partial \theta} = \frac{1}{D}\left[(\rho_{||}g' - 1 + \tilde{A}'_\zeta)\frac{\partial \tilde{A}_\theta}{\partial \theta} - (\rho_{||}I' + q + \tilde{A}'_\theta)\frac{\partial \tilde{A}_\zeta}{\partial \theta}\right], \tag{3.23a}$$

$$\frac{\partial \rho_{||}}{\partial \zeta} = \frac{1}{D}\left[(\rho_{||}g' - 1 + \tilde{A}'_\zeta)\frac{\partial \tilde{A}_\theta}{\partial \zeta} - (\rho_{||}I' + q + \tilde{A}'_\theta)\frac{\partial \tilde{A}_\zeta}{\partial \zeta}\right], \tag{3.23b}$$

$$\frac{\partial \rho_{||}}{\partial P_\theta} = \frac{1 - \rho_{||}g' - \tilde{A}'_\zeta}{D}, \tag{3.23c}$$

$$\frac{\partial \rho_{||}}{\partial P_\zeta} = \frac{q + \rho_{||}I' + \tilde{A}'_\theta}{D}. \tag{3.23d}$$

Having computed the partial derivatives of ψ_p and $\rho_{||}$ with respect to θ, ζ, P_θ and P_ζ, it is now possible to find the equations of motion from equations (3.19) by making use of the chain rule

$$\frac{\partial \mathcal{H}}{\partial x} = \frac{\partial H}{\partial \psi_p}\frac{\partial \psi_p}{\partial x} + \frac{\partial \mathcal{H}}{\partial \rho_{||}}\frac{\partial \rho_{||}}{\partial x}$$

where x represents one of the canonical variables to give,

$$\dot{\theta} = \frac{1}{D}\left[\rho_{||}B^2(1 - \rho_{||}g' - \tilde{A}'_\zeta) + g\left\{(\rho_{||}^2 B + \mu)B' + \tilde{\Phi}'\right\}\right], \tag{3.24a}$$

$$\dot{\zeta} = \frac{1}{D}\left[\rho_{||}B^2(\rho_{||}I' + q + \tilde{A}'_\theta) - I\left\{(\rho_{||}^2 B + \mu)B' + \tilde{\Phi}'\right\}\right], \tag{3.24b}$$

$$\dot{P}_\theta = -\frac{\rho_{||}B^2}{D}\left[(\rho_{||}g' - 1 + \tilde{A}'_\zeta)\frac{\partial \tilde{A}_\theta}{\partial \theta} - (\rho_{||}I' + q + \tilde{A}'_\theta)\frac{\partial \tilde{A}_\zeta}{\partial \theta}\right] - (\rho_{||}^2 B + \mu)\frac{\partial B}{\partial \theta} - \frac{\partial \tilde{\Phi}}{\partial \theta}, \tag{3.24c}$$

$$\dot{P}_\zeta = -\frac{\rho_{||}B^2}{D}\left[(\rho_{||}g' - 1 + \tilde{A}'_\zeta)\frac{\partial \tilde{A}_\theta}{\partial \zeta} - (\rho_{||}I' + q + \tilde{A}'_\theta)\frac{\partial \tilde{A}_\zeta}{\partial \zeta}\right] - \frac{\partial \tilde{\Phi}}{\partial \zeta}. \tag{3.24d}$$

Although these equations completely describe the guiding centre motion they do not represent the easiest numerical scheme to implement since it is necessary to invert P_θ and P_ζ to obtain ψ_p and $\rho_{||}$. A more practical approach is to evolve ψ_p and $\rho_{||}$ directly by means of their total time derivatives. $\dot{\psi}_p$ is simply expressed through the chain rule and equations (3.22) and once $\dot{\psi}_p$ is known, a simple expression for $\dot{\rho}_{||}$ can be formed from either of the expressions for the canonical momenta, equations (3.21a), or (3.21b).

$$\dot{\psi}_p = \frac{1}{D}\left[\left(I\frac{\partial \tilde{A}_\zeta}{\partial \theta} - g\frac{\partial \tilde{A}_\theta}{\partial \theta}\right)\dot{\theta} + \left(I\frac{\partial \tilde{A}_\zeta}{\partial \zeta} - g\frac{\partial \tilde{A}_\theta}{\partial \zeta}\right)\dot{\zeta} + g\dot{P}_\theta - I\dot{P}_\zeta\right], \tag{3.25a}$$

$$\dot{\rho}_{||} = \frac{1}{I}\left[\dot{P}_\theta - \frac{\partial \tilde{A}_\theta}{\partial \theta}\dot{\theta} - \frac{\partial \tilde{A}_\theta}{\partial \zeta}\dot{\zeta} - \frac{\partial \tilde{A}_\theta}{\partial t} - \left(q + \frac{\partial \tilde{A}_\theta}{\partial \psi_p} + \rho_{||}I'\right)\dot{\psi}_p\right]. \tag{3.25b}$$

These equations are then augmented by equations (3.24).

In deriving the above equations of motion a modification was made to the guiding centre velocity, $\mathbf{v} \to \mathbf{v} + \mathbf{w}$ such that equation (3.18) was satisfied. To obtain an expression for $\mathbf{w}$ first assume that $\mathbf{w}$ is parallel to $\mathbf{B}$. This a valid assumption since to lowest order particles follow magnetic field lines. Hence,

$$\mathbf{w} = \lambda \mathbf{B}.$$

and thus,

$$\mathbf{A}^* \cdot \mathbf{w} = \lambda \left(\mathbf{A} \cdot \mathbf{B} + \rho_{\|} B^2 \right)$$

$$\Rightarrow \qquad \mathbf{w} = -\frac{(\delta\rho_{\|} + \tilde{A}_{\psi_p})\dot{\psi}_p}{\mathbf{A} \cdot \mathbf{B} + \rho_{\|} B^2} \mathbf{B}$$

from equation (3.18).

The functions $I(\psi_p)$, $g(\psi_p)$, $q(\psi_p)$, $B(\psi_p, \theta)$, $\tilde{\mathbf{A}}(\psi_p, \theta, \zeta, t)$, and $\tilde{\Phi}(\psi_p, \theta, \zeta, t)$ define the particle trajectories through the equations (3.24a), (3.24b), (3.25a) and (3.25b). To describe the path in real space, the vector function $\mathbf{x} = \mathbf{x}(\psi_p, \theta, \zeta)$ which allows the transformation to the inertial laboratory frame of reference, must be known, as indicated in §2.4.1.

The form used above to represent the perturbed field was completely general. By choosing a particular form for the perturbed vector potential $\tilde{\mathbf{A}}$, the equations of motion may be simplified at the expense of this generality. The description of low-β shear Alfvén waves in §2.1 indicated that $\delta B_{\|} = 0$ and $E_{\|} = 0$. The first of these conditions places a constraint upon $\tilde{A}_{\perp}$ which can be encompassed by representing the perturbed magnetic field through the variable, $\tilde{\alpha}(\psi_p, \theta, \zeta, t)$ defined through the relation

$$\tilde{\mathbf{A}} = \tilde{\alpha}(\mathbf{x}, t)\mathbf{B}.$$

From this definition it can be seen that $\tilde{\alpha}$ is closely related to the parallel component of the perturbed vector potential and it follows that the resulting perturbation to the magnetic field is given by

$$\delta\mathbf{B} = \boldsymbol{\nabla} \wedge (\tilde{\alpha}\mathbf{B}_0)\,.$$

The condition that $E_{\|} = 0$ provides a relationship between $\tilde{\alpha}$ and the scalar potential $\tilde{\Phi}$:

$$E_{\|} = -\nabla_{\|}\tilde{\Phi} - \frac{\partial}{\partial t}(\tilde{\alpha}B_0) = 0.$$

Hence only one scalar field is required to describe the field perturbations arising from the AE present. Substituting for the covariant components of $\tilde{\alpha}\mathbf{B}$ into the above equations of motion produces the same expressions as used by White and Chance [54]:

$$\dot{\theta} = \frac{1}{D}\left[\rho_{\|}B^2(1 - \rho_c g' - g\tilde{\alpha}') + g\left\{(\rho_{\|}^2 B + \mu)B' + \tilde{\Phi}'\right\}\right], \tag{3.26a}$$

$$\dot{\zeta} = \frac{1}{D}\left[\rho_{\|}B^2(\rho_c I' + q + I\tilde{\alpha}') - I\left\{(\rho_{\|}^2 B + \mu)B' + \tilde{\Phi}'\right\}\right], \tag{3.26b}$$

$$\dot{\psi}_p = \frac{1}{D}\left[\rho_{\|}B^2\left(g\frac{\partial\tilde{\alpha}}{\partial\theta} - I\frac{\partial\tilde{\alpha}}{\partial\zeta}\right) - \left(g\frac{\partial\tilde{\Phi}}{\partial\theta} - I\frac{\partial\tilde{\Phi}}{\partial\zeta}\right) - g(\rho_{\|}^2 B + \mu)\frac{\partial B}{\partial\theta}\right], \tag{3.26c}$$

$$\dot{\rho}_{\|} = \frac{1}{D}\left[\left(I\frac{\partial\tilde{\alpha}}{\partial\zeta} - g\frac{\partial\tilde{\alpha}}{\partial\theta}\right)\left\{(\rho_{\|}^2 B + \mu)B' + \tilde{\Phi}'\right\} - (q + \rho_c I' + I\tilde{\alpha}')\frac{\partial\tilde{\Phi}}{\partial\zeta}\right.$$
$$\left. + (\rho_c g' - 1 + g\tilde{\alpha}')\left\{(\rho_{\|}^2 B + \mu)\frac{\partial B}{\partial\theta} + \frac{\partial\tilde{\Phi}}{\partial\theta}\right\}\right] - \frac{\partial\tilde{\alpha}}{\partial t}, \tag{3.26d}$$

where $\rho_c = \rho_{||} + \tilde{\alpha}$ and,

$$D = \rho_c[gI' - g'I] + I + qg.$$

Given the equilibrium functions, g, I, q and B, and the perturbation parameter $\tilde{\alpha}$, particle trajectories may be accurately followed in the presence of an AE. Mathematically the model allows any spatial and temporal wave structure to be imposed providing it meets the assumptions of the guiding centre approach described in §2.4.2. In this thesis the spatial structure of the waves present are determined using existing MHD codes to solve equation (2.13) with the relevant background plasma parameters.

In the next section the model is closed by specifying the waves' response to the ensemble interaction with a distribution of fast particles. In this way the model becomes self-consistent as well as nonlinear; the individual particles move in response to the wave fields, the waves evolve in response to their collective interaction with the particles which then determines the particle motion in the wave field.

3.3 Self-consistent Wave Evolution

In this section the equations governing the self-consistent response of the waves to the fast particles in the system are derived. The approximation is made that the spatial structure of the waves remain invariant with only a time-varying amplitude and phase. The method through which the perturbed electrostatic potential is calculated from the perturbed fluid velocity supplied by the MHD code CASTOR is also presented. This closes the system of equations necessary to model the interaction of fast particles with AE in tokamak plasmas.

3.3.1 Wave Equations

The wave evolution, like the particle motion, can be derived by a consideration of the system Lagrangian. The total system Lagrangian may be resolved into four components: the fast particle Lagrangian $\mathcal{L}_{fp}$ describing the motion of the energetic ions in an equilibrium field; the interaction Lagrangian $\mathcal{L}_{int}$ describing the effect of the Alfvén waves upon the particle motion; the background, or bulk, plasma contribution to the Alfvén waves $\mathcal{L}_{bulk}$; the electromagnetic wave Lagrangian $\mathcal{L}_{em}$ describing the electromagnetic component of the Alfvén waves.

$$\mathcal{L}_{sys} = \overbrace{\mathcal{L}_{fp} + \underbrace{\mathcal{L}_{int}}_{\substack{\text{Particle Lagrangian given in equation (3.15)}}}}^{\text{Particle Lagrangian given in equation (3.15)}} + \overbrace{\underbrace{\mathcal{L}_{bulk} + \mathcal{L}_{em}}_{\substack{\text{Wave Lagrangian, } \mathcal{L}_w}}}^{\text{Wave Lagrangian, } \mathcal{L}_w}$$

Wave equations

Interaction Lagrangian

The interaction Lagrangian for an ensemble of n_p particles (labelled by the subscript j) and a spectrum of n_w waves (subscript k) consists of the usual velocity dependent potential that appears in the description of a free particle in an electromagnetic field [52] and can be seen by inspection in the particle Lagrangian, equation (3.15), in the presence of a perturbed field. In it's simplest form, this may be expressed as,

$$\mathcal{L}_{int} = \sum_{j=1}^{n_p} (\tilde{\mathbf{A}}_j \cdot \mathbf{v}_j - \tilde{\Phi}_j),$$

where the subscript j refers to the fact that the corresponding quantity is to be evaluated at the spatial location of the jth particle, $(\psi_{pj}, \theta_j, \zeta_j)$, and $\mathbf{A}_j$ and Φ_j represent the sum of all the contributions from each of the waves present along the particle trajectories.

Before proceeding further the representation used to describe the perturbed fields is introduced. Each wave is characterized by a distinct toroidal eigenfunction (index k), and represented as a sum of poloidal harmonics m, so that

$$\tilde{\Phi}_k = \sum_m \tilde{\phi}_{km}(\psi) e^{i(\mathbf{k}_{mn}\cdot\mathbf{x} - \omega_k t)} = \sum_m \tilde{\phi}_{km}(\psi) e^{i(n_k\zeta - m\theta - \omega_k t)},$$

where the wave vector,

$$\mathbf{k}_{mn} = n\boldsymbol{\nabla}\zeta - m\boldsymbol{\nabla}\theta,$$

and in general $\tilde{\phi}_{km}$ may be a complex quantity containing information regarding the relative phase-shifts between neighbouring harmonics.

The inclusion of non-ideal FLR effects within the ideal MHD model to treat KTAE leads to a finite parallel electric field in a thin layer around the $q(\psi_p) = (m + 1/2)/n$ surface. Since the energetic particle orbit width is typically much larger than the width of this layer, the majority of the wave-particle power transfer occurs at surfaces away from this region [39]. It is therefore appropriate to make the assumption that $E_\parallel = 0$ everywhere thereby defining a relationship between $\tilde{\Phi}_k$ and $\tilde{\alpha}_k$:

$$\begin{aligned} E_{\parallel k} = 0 \quad &\Rightarrow \quad \nabla_\parallel \tilde{\Phi}_k + \frac{\partial}{\partial t}(\tilde{\alpha}_k B_0) = 0 \\ &\Rightarrow \quad \sum_m k_{\parallel m} \tilde{\phi}_{km} e^{i(n_k\zeta - m\theta - \omega_k t)} = \omega_k B_0 \sum_m \tilde{\alpha}_{km} e^{i(n_k\zeta - m\theta - \omega_k t)} \\ &\Rightarrow \quad \tilde{\alpha}_{km} = \frac{k_{\parallel m}}{\omega_k B_0} \tilde{\phi}_{km}. \end{aligned}$$

This relationship will be used below to eliminate $\tilde{\alpha}_{km}$ in favour of $\tilde{\phi}_{km}$.

The notation used to describe $\tilde{\Phi}_k$ can be simplified by defining the real and imaginary parts of the electrostatic scalar potential to be

$$\begin{aligned} C_{jkm} &\equiv \Re e[\tilde{\phi}_{km}(\psi_{pj}) e^{i\Theta_{jkm}}], \\ S_{jkm} &\equiv \Im m[\tilde{\phi}_{km}(\psi_{pj}) e^{i\Theta_{jkm}}], \end{aligned}$$

where

$$\Theta_{jkm} \equiv n_k\zeta_j - m\theta_j - \omega_k t.$$

Further, by including a slowly varying complex amplitude term, $A_k(t)e^{-i\sigma_k(t)}$ for each wave k, and defining $\mathcal{X}_k$ and $\mathcal{Y}_k$ such that

$$\begin{aligned}
\mathcal{X}_k &\equiv \Re e\left[A_k e^{-i\sigma_k}\right], \\
&\equiv A_k\cos(\sigma_k), \\
\mathcal{Y}_k &\equiv -\Im m\left[A_k e^{-i\sigma_k}\right], \\
&\equiv A_k\sin(\sigma_k),
\end{aligned}$$

so that

$$A_k(t)e^{-i\sigma_k(t)} = \mathcal{X}_k(t) - i\mathcal{Y}_k(t)$$

we can write the full potential at the jth particle position as

$$\tilde{\Phi}_j = \sum_{k=1}^{n_w}\sum_m \left[\mathcal{X}_k(t)C_{jkm} + \mathcal{Y}_k(t)S_{jkm}\right],$$

from which it also follows that

$$\tilde{\alpha}_j = \frac{1}{B_0}\sum_{k=1}^{n_w}\frac{1}{\omega_k}\sum_m k_{\|m}\left[\mathcal{X}_k(t)C_{jkm} + \mathcal{Y}_k(t)S_{jkm}\right].$$

The introduction of $\mathcal{X}_k$ and $\mathcal{Y}_k$ to describe the degrees of freedom of the waves rather than simply the wave amplitude, A_k, and phase-shift, σ_k, is undertaken to improve the numerical properties of the ensuing equations of motion. This change is equivalent to the change from polar to Cartesian coordinates where although both formulations are equivalent, the appearance of apparent singularities in the polar equations of motion at the axis introduces computational difficulties. Returning to the interaction Lagrangian, it is seen that it may now be written as

$$\mathcal{L}_{int} = \sum_{j=1}^{n_p}\sum_{k=1}^{n_w}\frac{1}{\omega_k}\sum_m (k_{\|m}v_{\|j} - \omega_k)\left[\mathcal{X}_k C_{jkm} + \mathcal{Y}_k S_{jkm}\right]. \tag{3.27}$$

Wave Lagrangian

In this section the wave Lagrangian for Alfvén waves is derived. As indicated in §2.1.2, Alfvén waves represent a balance between plasma inertia and field line tension and consequently the wave Lagrangian $\mathcal{L}_w$ must account for these components by including contributions from the bulk plasma particles labelled by subscript j providing the inertia, and an electromagnetic component [63] with subscript k,

$$\mathcal{L}_w = \underbrace{\sum_j \left\{\frac{1}{2}mv_j^2 + e\left(\mathbf{A}_j\cdot\mathbf{v}_j - \Phi_j\right)\right\}}_{\mathcal{L}_{bulk}} + \underbrace{\frac{1}{2\mu_0}\int_V \left\{\frac{1}{c^2}E^2 - B^2\right\}d^3x}_{\mathcal{L}_{em}}.$$

This expression may be simplified by specifying the bulk plasma's perturbed velocity in terms of the perturbed MHD fluid velocity,

$$\mathbf{v} = \frac{\mathbf{E} \wedge \mathbf{B}}{B^2},$$

and writing all quantities as the sum of an equilibrium component and small perturbed parts, $\mathbf{B} = \mathbf{B}_0 + \sum_{k=1}^{n_w} \tilde{\mathbf{B}}_k$, to give

$$\begin{aligned}
\mathcal{L}_w \;=\; & \sum_{\substack{\text{bulk}\\ \text{plasma}}} \left[\frac{1}{2} m \left\{ \mathbf{v}_0 + \sum_k \frac{\tilde{\mathbf{E}}_k \wedge \mathbf{B}_0}{B_0^2} + \sum_{k,k'} \frac{\tilde{\mathbf{E}}_k \wedge \tilde{\mathbf{B}}_{k'}}{B_0^2} \right\}^2 \right. \\
& \left. + e \left\{ \left(\mathbf{A}_0 + \sum_k \tilde{\mathbf{A}}_k \right) \cdot \left\{ \mathbf{v}_0 + \sum_k \frac{\tilde{\mathbf{E}}_k \wedge \mathbf{B}_0}{B_0^2} + \sum_{k,k'} \frac{\tilde{\mathbf{E}}_k \wedge \tilde{\mathbf{B}}_{k'}}{B_0^2} \right\} - \sum_k \tilde{\Phi}_k \right\} \right] \\
& + \frac{1}{2\mu_0} \int_V \left\{ \frac{1}{c^2} \sum_k \tilde{E}_k^2 - B_0^2 - \sum_k (2\mathbf{B}_0 \cdot \tilde{\mathbf{B}}_k + \tilde{B}_k^2) \right\} d^3x,
\end{aligned}$$

where it has been assumed that the unperturbed electric fields are identically zero everywhere within the plasma volume. The orthogonality of the MHD eigenfunctions prevents the formation of a double sum over the perturbed waves present in the final volume integral by ensuring that all of the cross terms are zero.

Proceeding to the continuum limit of an integral over the plasma volume and expanding the Lagrangian in perturbed powers gives,

$$\mathcal{L}_0 \;=\; \int_V \left\{ \frac{1}{2} n_i m v_0^2 + n_i e \mathbf{A}_0 \cdot \mathbf{v}_0 - \frac{1}{2\mu_0} B_0^2 \right\} d^3x,$$

(Equilibrium force balance $\Rightarrow \mathcal{L}_0 \equiv 0$)

$$\mathcal{L}_1 \;=\; \sum_k \int_V \left\{ n_i m \mathbf{v}_0 \cdot \frac{\mathbf{E}_k \wedge \mathbf{B}_0}{B_0^2} + n_i e \left(\mathbf{A}_0 \cdot \frac{\mathbf{E}_k \wedge \mathbf{B}_0}{B_0^2} - \Phi_k \right) - \frac{1}{\mu_0} \mathbf{B}_0 \cdot \tilde{\mathbf{B}}_k \right\} d^3x,$$

(1st order force balance $\Rightarrow \mathcal{L}_1 \equiv 0$)

$$\begin{aligned}
\mathcal{L}_2 \;=\; & \int_V \left\{ \frac{1}{2} n_i m \left(\sum_k \frac{(\mathbf{E}_k \wedge \mathbf{B}_0)^2}{B_0^4} + 2 \sum_{k,k'} \mathbf{v}_0 \cdot \frac{\mathbf{E}_k \wedge \mathbf{B}_{k'}}{B_0^2} \right) \right. \\
& \left. + n_i e \sum_{k,k'} \left(\mathbf{A}_0 \cdot \frac{\mathbf{E}_k \wedge \mathbf{B}_{k'}}{B_0^2} + \mathbf{A}_k \cdot \frac{\mathbf{E}_{k'} \wedge \mathbf{B}_0}{B_0^2} \right) - \frac{1}{2\mu_0} \sum_k \left(\frac{1}{c^2} E_k^2 - B_k^2 \right) \right\} d^3x,
\end{aligned}$$

where n_i is the ion number density. The two lowest order terms are identically zero for the reasons given and consequently the wave Lagrangian may be approximated by the next order term, $\mathcal{L}_2$. This expression may be further simplified by observing that for shear-Alfvén waves $\mathbf{B}_1$ and $\mathbf{E}_1$ are orthogonal to $\mathbf{B}_0$, so that it becomes

$$\mathcal{L}_w = \int_V \left\{ \frac{1}{2} n_i m \sum_k \frac{E_k^2}{B_0^2} + n_i e \sum_{k,k'} \mathbf{A}_0 \cdot \frac{\mathbf{E}_k \wedge \mathbf{B}_{k'}}{B_0^2} - \frac{1}{2\mu_0} \sum_k \left(\frac{1}{c^2} E_k^2 - B_k^2 \right) \right\} d^3x.$$

The observation that $E_{||} = 0$ enables the term $\mathbf{A}_0 \cdot \mathbf{E}_1 \wedge \mathbf{B}_1$ to be dropped, since choosing the equilibrium gauge $\Phi_0 \equiv 0$ ensures that $\mathbf{A}_0 = \mathbf{A}_{\perp 0}$, and $\mathbf{A}_0$, $\mathbf{E}_1$, and $\mathbf{B}_1$ become co-planar from which it follows that the Lagrangian can now be written as

$$\begin{aligned}\mathcal{L}_w &= \sum_k \int_V \left\{ \frac{1}{2}\left(\frac{n_i m}{B_0^2} + \varepsilon_0\right) E_k^2 - \frac{1}{2\mu_0} B_k^2 \right\} d^3x \\ &= \sum_k \int_V \left\{ \frac{\varepsilon_0}{2}\left(\frac{c^2}{v_A^2} + 1\right) E_k^2 - \frac{1}{2\mu_0} B_k^2 \right\} d^3x,\end{aligned}$$

where $v_A(\psi, \theta) = B/(\mu_0 n_i m)$ is the local Alfvén velocity. Typical tokamak plasma parameters ensure that $c^2/v_A^2 \gg 1$ and allow the wave Lagrangian to be written as:

$$\mathcal{L}_w = \sum_k \frac{1}{2\mu_0} \int_V \left\{ \frac{1}{v_A^2} E_k^2 - B_k^2 \right\} d^3x.$$

This may be re-written in terms of $\tilde{\Phi}$ and $\tilde{\alpha}$ by recalling that

$$\begin{aligned}\mathbf{E}_k &= -\boldsymbol{\nabla}\tilde{\Phi}_k - \frac{\partial \tilde{\alpha}_k \mathbf{B}_0}{\partial t} \\ \mathbf{B}_k &= \boldsymbol{\nabla} \wedge (\tilde{\alpha}_k \mathbf{B}_0) \\ &\simeq -\hat{\mathbf{B}}_0 \wedge \boldsymbol{\nabla}(\tilde{\alpha}_k B_0),\end{aligned}$$

where the term $\tilde{\alpha}_k \boldsymbol{\nabla} \wedge \mathbf{B}_0$ is neglected from the final expression to ensure that $\mathbf{B}_0 \cdot \mathbf{B}_1 = 0$ and the waves are transverse. By defining the 'super-potential' χ such that,

$$\tilde{\Phi}_k = \frac{\partial \chi_k}{\partial t},$$

it then follows from the $\mathbf{E}_{||k} = 0$ condition, that

$$\tilde{\alpha}_k = -\frac{1}{B_0}(\hat{\mathbf{B}}_0 \cdot \boldsymbol{\nabla})\chi_k,$$

and the wave Lagrangian may be expressed in terms of this single variable as

$$\mathcal{L}_w = \sum_k \frac{1}{4\mu_0} \int_V \left\{ \frac{1}{v_A^2} \left| \boldsymbol{\nabla}_\perp \frac{\partial \chi_k}{\partial t} \right|^2 - \left| \hat{\mathbf{B}}_0 \wedge \boldsymbol{\nabla}(\hat{\mathbf{B}}_0 \cdot \boldsymbol{\nabla})\chi_k \right|^2 \right\} d^3x.$$

If the slowly varying complex amplitude term is made explicit in the notation used to denote χ_k,

$$\chi_k \longrightarrow A_k(t)\, \chi_k\, e^{-i\omega_k t - i\sigma_k(t)},$$

then an expansion in the time variation using powers of $\dot{A}_k/(\omega_k A_k)$ and $\dot{\sigma}_k/\omega_k$ reveals that to lowest order,

$$\mathcal{L}_{w0} = \sum_k \frac{A_k^2}{4\mu_0} \int_V \left\{ \frac{\omega_k^2}{v_A^2} |\boldsymbol{\nabla}_\perp \chi_k|^2 - \left| \hat{\mathbf{B}}_0 \wedge \boldsymbol{\nabla}(\hat{\mathbf{B}}_0 \cdot \boldsymbol{\nabla})\chi_k \right|^2 \right\} d^3x.$$

This is the Lagrangian formulation of the wave equation describing shear Alfvén waves and is equivalent to equation (2.13). This equation is solved as an eigenvalue problem for ω_k^2 to obtain the spatial eigenfunction, χ_k. The assumption that this eigenfunction remains spatially invariant means that $\mathcal{L}_{w0} \equiv 0$ and need not be retained within the formulation. Only the next order corrections to the eigenvalue ω_k^2 are included through the time variation of A_k and σ_k. Collecting together the remaining terms the Lagrangian becomes,

$$\mathcal{L}_w = \sum_k \frac{A_k^2}{4\mu_0} \int_V \frac{1}{v_A^2} \left\{ \nabla_\perp \frac{\partial \chi_k}{\partial t} \cdot \nabla_\perp \frac{\partial \chi_k^*}{\partial t} - \omega_k^2 \nabla_\perp \chi_k \cdot \nabla_\perp \chi_k^* \right\} d^3x,$$

which is equivalent to the wave Lagrangian given by Breizman and Sharapov [39],

$$\mathcal{L}_w = \sum_k \frac{A_k^2 \dot{\sigma}_k}{2\mu_0 \omega_k} \int_V \frac{\left| \nabla_\perp \tilde{\Phi}_k \right|^2}{v_A^2} d^3x,$$

which when written in terms of what may be referred to as the 'wave energy' becomes

$$\mathcal{L}_w = \sum_k \frac{E_k}{\omega_k} \left[A_k^2 \dot{\sigma}_k \right], \qquad \text{with} \qquad E_k = \frac{1}{2\mu_0} \int_V \frac{\left| \nabla_\perp \tilde{\Phi}_k \right|^2}{v_A^2} d^3x.$$

From the above definitions,

$$\begin{aligned} A_k^2 = \mathcal{X}_k^2 + \mathcal{Y}_k^2 \qquad \text{and} \qquad \sigma_k &= \arctan\left(\frac{\mathcal{Y}_k}{\mathcal{X}_k}\right) \\ \Rightarrow \qquad \dot{\sigma}_k &= \frac{\mathcal{X}_k \dot{\mathcal{Y}}_k - \dot{\mathcal{X}}_k \mathcal{Y}_k}{A_k^2}, \end{aligned}$$

allowing $\mathcal{L}_w$ to be written in the final form,

$$\mathcal{L}_w = \sum_{k=1}^{n_w} \frac{E_k}{\omega_k} \left[\mathcal{X}_k \dot{\mathcal{Y}}_k - \dot{\mathcal{X}}_k \mathcal{Y}_k \right]. \tag{3.28}$$

As indicated at the beginning of this section, the relevant Lagrangian to vary to obtain the wave evolution equations is $\mathcal{L}_{int} + \mathcal{L}_w$, which from equations (3.27) and (3.28) becomes

$$\mathcal{L} = \sum_{k=1}^{n_w} \frac{1}{\omega_k} \left\{ \sum_{j=1}^{n_p} \sum_m (k_{\|m} v_{\|j} - \omega_k) \left[\mathcal{X}_k C_{jkm} + \mathcal{Y}_k S_{jkm} \right] + E_k \left[\mathcal{X}_k \dot{\mathcal{Y}}_k - \dot{\mathcal{X}}_k \mathcal{Y}_k \right] \right\}. \tag{3.29}$$

Varying with respect to $\mathcal{X}_k$ and $\mathcal{Y}_k$ gives

$$\dot{\mathcal{X}}_k = \frac{1}{2E_k} \sum_{j=1}^{n_p} \sum_m (k_{\|m} v_{\|j} - \omega_k) S_{jkm}, \tag{3.30a}$$

$$\dot{\mathcal{Y}}_k = -\frac{1}{2E_k} \sum_{j=1}^{n_p} \sum_m (k_{\|m} v_{\|j} - \omega_k) C_{jkm}, \tag{3.30b}$$

which forms a set of $2 \times n_w$ first order differential equations for the time evolution of the waves present.

3.3.2 Calculation of Scalar Potential

The scalar potential used in the model may be calculated directly from the perturbed fluid velocity eigenfunction obtained from the MHD code, CASTOR. In ideal MHD the fluid velocity is related to the field variables through Ohm's law,

$$\mathbf{E} + \mathbf{v} \wedge \mathbf{B} = 0 \quad \Rightarrow \quad \mathbf{v} = \frac{\mathbf{E} \wedge \mathbf{B}}{B^2}.$$

Writing the electric field in terms of the vector and scalar potentials,

$$\mathbf{E} = -\nabla\Phi - \frac{\partial \mathbf{A}}{\partial t}$$

this becomes

$$\mathbf{v} = -\frac{\nabla\Phi \wedge \mathbf{B}}{B^2} - \frac{1}{B^2}\frac{\partial \mathbf{A}}{\partial t} \wedge \mathbf{B}.$$

In the low-β limit pressure effects can be ignored and the field perturbations are almost transverse. An easy way of ensuring this ($\delta \mathbf{B}_{\|} \approx 0$) is by setting $\mathbf{A}_{\perp} = 0$. Thus $\mathbf{A} \wedge \mathbf{B} = 0$ and the second term in this expression may be neglected. Substituting for $\mathbf{B}$, expanding $\nabla\Phi$, recalling the ansatz $\Phi = \sum_{km} \phi_{km} e^{i(n_k\zeta - m\theta - \omega t)}$ and restricting attention to the radial component gives,

$$\phi_{km} = -i\,\frac{I + qg}{mg + n_k I}\, v^{\psi},$$

providing a simple closed expression for the scalar potential. The magnetic perturbation parameter, α, is simply related to ϕ through

$$\tilde{\alpha}_{km} = \frac{k_{\|m}}{\omega_k B_0}\tilde{\phi}_{km}.$$

3.4 δf method

Having derived the equations describing the motion of energetic ions in the presence of a spectrum of wave perturbations it is now possible to develop a model to perform simulations of realistic situations. To obtain a specific particle distribution several approaches have been identified. The first approach is to initialise the ensemble of particles with the desired initial distribution. This has the obvious disadvantage of requiring large computing resources since many simulation particles are needed to adequately fill the 5-D phase-space. The second approach makes an effort to prevent the number of differential equations that need to be solved spiralling into computational unfeasibility by reducing the number of particles that need to be followed. This is achieved by uniformly weighting each particle and represents a significant step forward, since now many more particles can be represented than are actually followed. Obviously the dynamics of

these weighted particles, or 'markers', remains unaltered from their unweighted counterparts, with the only change being the inclusion of the constant weighting factor in the wave-particle interaction. Allowing markers to have different weights, and therefore represent different numbers of particles, removes the initialisation constraint that markers must be loaded with the same distribution as required for the fast particles. This enables more markers to be loaded around the regions where the wave-particle interaction is the strongest, thereby improving the resolution whilst still representing the required fast particle distribution. Such a procedure assumes however that the regions of resonant interaction are known *a-priori*, which is generally not the case.

To resolve small fluctuations in the energetic ion density it becomes necessary to use very large numbers of simulation particles [64]. The desire to improve the resolution of such simulations, and therefore reduce the number of particles required, was the driving impetus behind the development of a new class of techniques now know as δf methods. Early attempts at improving numerical resolution made use of techniques such as 'quiet starts' [65], and also by using linearization techniques [66] to track the perturbed quantities in terms of the equilibrium trajectories. The δf algorithm was first conceptualized by Tajima and Perkins [67] and has been further developed by many others. Dimits and Lee [66] successfully implemented the first 'partially linear' gyro-kinetic δf algorithm, whilst Kotschenreuther independently developed a similar algorithm [16]. Parker and Lee [15] developed the first fully nonlinear gyro-kinetic method in connection with their simulations of drift-waves, which Candy [68] refined and went on to make more generally applicable.

In a conventional particle code using the first initialisation technique outlined above, the real particle density is related to the density of the simulation particles. In the δf algorithm each 'particle' is a marker at which the value of the distribution function is known. The method becomes analogous to the solution of the Vlasov equation using a fluid model on a Lagrangian grid. The value of the distribution function for each marker is evolved according to the method of characteristics. The position of each marker is the tip of each characteristic of the distribution function, that is, the latest position of one of the natural paths for the solution of the equations. The markers are like particles in that they move in space with the same equations of motion. However, rather than representing single particles, they represent evolving values of the distribution function.

The step from which the δf method takes it's name is the decomposition of the fast particle distribution function f into two parts, an analytically described background component f_0, and the remaining component δf,

$$f = \underbrace{f_0(\Gamma^{(p)})}_{\text{analytic}} + \underbrace{\delta f(\Gamma^{(p)}, t)}_{\text{markers}}$$

where $\Gamma^{(p)}$ represents the physical phase-space comprised of the six components of space and velocity. The key element of the δf method is that only the change in the distribution function is represented by the markers. Since the initial distribution is only expected to be weakly distorted through it's interaction with the waves present,

choosing f_0 to represent this initial distribution allows the finite lattice of markers to represent the small change δf and affords a favourable reduction in numerical noise in the system of the order $|\delta f/f|^2$ [69]. Note that the separation of f into an analytically described component f_0 and a numerically described component δf is formally valid in all cases and makes no assumptions regarding the fact that the latter be much smaller than the former. However, it is only for the case where $\delta f \ll f_0$ that substantial reductions in simulation noise are expected.

The decomposition of the fast particle distribution function suggests the following transformation rule for integral operators:

$$\int f(\Gamma^{(p)},t)\, g(\Gamma^{(p)},t)\, d\Gamma^{(p)} \longleftrightarrow \int f_0(\Gamma^{(p)})\, g(\Gamma^{(p)},t)\, d\Gamma^{(p)} + \sum_{j=1}^{n_p} \delta f_j(t)\, g(\Gamma_j^{(p)}(t),t)\, \Delta\Gamma^{(p)},$$

where $\Delta\Gamma^{(p)}$ is the finite physical phase-space volume element associated with each marker. If f_0 is specified such that it is toroidally symmetric then upon applying this transformation rule to the wave equations (3.30) it is found that the term containing f_0 is identically zero, leaving only the contribution from the perturbed part of the distribution function, δf. To exploit this property, f_0 is chosen to be independent of ζ, and since in the absence of any plasma waves f_0 is expected to be invariant it is defined in terms of the *unperturbed* constants of the motion,

$$f_0 = f_0(P_\zeta^{(0)}, \mathcal{E}^{(0)}; \mu),$$

where,

$$\begin{aligned} P_\zeta^{(0)} &= P_\zeta - \tilde{\alpha} g, \\ \mathcal{E}^{(0)} &= \mathcal{E} - \tilde{\Phi}. \end{aligned}$$

This ensures that f_0 does not contribute to the wave growth and allows the statistical noise which would otherwise result from representing f_0 by a finite number of markers to be reduced. By demanding that f_0 is an analytical function of the unperturbed constants of the motion, $P_\zeta^{(0)}$, $\mathcal{E}^{(0)}$ and μ, ensures that in the absence of any waves the initial number of particles,

$$n_0 = \int_V f_0(P_\zeta^{(0)}, \mathcal{E}^{(0)}; \mu)\, d\Gamma^{(p)},$$

is time-invariant since f_0 has no explicit time dependence. It follows then, that in the absence of any particle sources and sinks the change in the number of particles,

$$\delta n = \int_V \delta f\, d\Gamma^{(p)} = 0.$$

The use of the δf method imparts an additional attribute to each marker, namely the *change* in the value of the distribution function at that point. The evolution of

this quantity is given by the relevant kinetic equation which in the absence of sources or sinks becomes $\dot{f} = 0$ and can be rearranged to give

$$\dot{\delta f}_j = -\dot{P}_{\zeta j}^{(0)} \frac{\partial f_0}{\partial P_{\zeta j}^{(0)}} - \dot{\mathcal{E}}_j^{(0)} \frac{\partial f_0}{\partial \mathcal{E}_j^{(0)}}, \tag{3.31}$$

where j is the index identifying each marker. This may be related to the more intuitive notion of the change in the number of particles represented by each marker δn_j through,

$$\delta n_j(t) \equiv \delta f_j(t)\, \Delta\Gamma_j^{(p)}(t). \tag{3.32}$$

It is reassuring to note that by specifying $f_0 \equiv 0$ so that $\delta f = f$, then the model regresses to a conventional particle simulation with fixed weight markers, $\dot{\delta f} \equiv 0$.

In terms of the formulation adopted within this thesis it is necessary to express the volume element $\Delta\Gamma_j^{(p)}$ in terms of the Boozer magnetic coordinate system introduced in §3.1 and spherical coordinates for the velocity components as depicted in Fig. 3.3. These are the most appropriate velocity variables to use since they naturally allow the

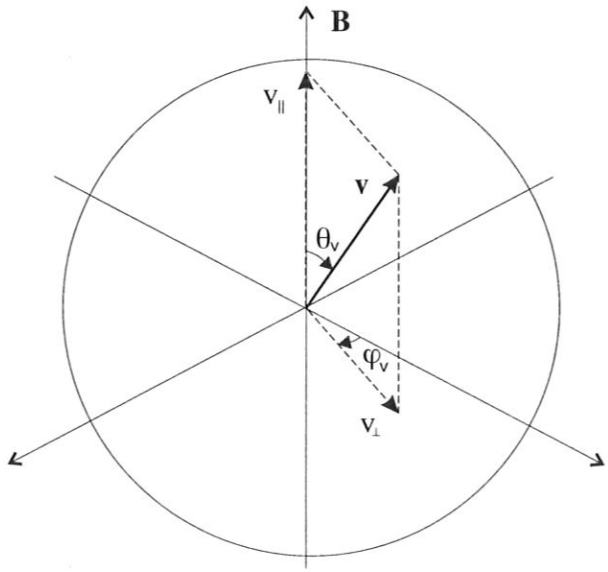

Figure 3.3: Spherical coordinates used to represent the velocity components.

degeneracy associated with the guiding centre motion to be exploited to reduce the number of dimensions of the problem. The velocity volume element expressed in these coordinates is

$$d^3v = dv\,(v\,d\theta_v)\,(v\,\sin\theta_v\,d\varphi_v),$$

where φ_v is the velocity azimuthal angle and the velocity polar angle θ_v is referred to as the pitch angle since it represents the angle between the particle motion and the

local magnetic field lines. Defining λ to be the cosine of the pitch angle,

$$\lambda = \cos\theta_v = \frac{v_\parallel}{v},$$

allows the velocity volume element to be written as

$$d^3v = v^2\, dv\, d\lambda\, d\varphi_v.$$

In §3.2 it was indicated that once μ is specified, the only velocity dimension required is $v_\parallel$. Since $\mu = mv_\perp^2/2B$ the direction of $v_\perp$ is not required, just the magnitude. Hence the azimuthal velocity angle φ_v is irrelevant and can be integrated out to give the reduced phase-space form,

$$d^3v = 2\pi\, v^2\, dv\, d\lambda.$$

The infinitesimal physical phase-space volume element is thus,

$$d\Gamma^{(p)} \equiv d^3v\, d^3x = \underbrace{2\pi\, v^2\, dv\, d\lambda}_{\substack{\text{velocity}\\ \text{element}}}\ \underbrace{\mathcal{J}\, d\psi_p\, d\theta\, d\zeta}_{\substack{\text{spatial}\\ \text{element}}},$$

where $\mathcal{J}$ is the Jacobian given in equation (3.13).

Evaluating $\Delta\Gamma^{(p)}$ at each marker location is not an easy task since the volume elements $d\Gamma_j^{(p)}$ are compressible and therefore change with the marker flow. However, their calculation is facilitated by the fact that the flow in canonical space is incompressible (a consequence of Liouville's theorem) and that therefore the canonical volume element associated with each marker is independent of time and need only be calculated once. The relationship between the canonical and physical phase-space elements is described by the Jacobian $\mathcal{J}^{(pc)}(t)$ and provides an elegant way of obtaining the physical phase-space volume elements at any time during the simulation. The caveat is however, that it is necessary to determine the canonical phase-space volume element associated with each marker.

Uniformly loading some chosen phase-space $\mathcal{U}$ offers a simple solution to this problem since providing the total phase-volume is known, the volume associated with each marker $\Delta\mathcal{U}$ is trivially calculated. This may then be related to the canonical volume element through the relevant Jacobian, $\mathcal{J}^{(cu)}$. Choosing $\mathcal{U}$ to consist of physically more familiar variables, rather than the canonical variables, allows the problem to become more intuitively transparent and avoids difficulties associated with inverting the canonical variables into the physical ones.

The infinitesimal canonical volume element is

$$d\Gamma^{(c)} \equiv d\xi\, d\mu\, d\theta\, dP_\theta\, d\zeta\, dP_\zeta \equiv 2\pi\, d\mu\, d\theta\, dP_\theta\, d\zeta\, dP_\zeta,$$

where as before the factor 2π has arisen from an integration over the gyro-phase, ξ. This volume element is related to the physical phase-space element through

$$d\Gamma^{(p)} = \mathcal{J}^{(pc)}\, d\Gamma^{(c)},$$

where

$$\mathcal{J}^{(pc)} \equiv \frac{\partial \Gamma^{(p)}}{\partial \Gamma^{(c)}} = v^2 \mathcal{J} \begin{vmatrix} \frac{\partial \theta}{\partial \theta} & \frac{\partial \theta}{\partial \zeta} & \frac{\partial \theta}{\partial P_\theta} & \frac{\partial \theta}{\partial P_\zeta} & \frac{\partial \theta}{\partial \mu} \\ \frac{\partial \zeta}{\partial \theta} & \frac{\partial \zeta}{\partial \zeta} & \frac{\partial \zeta}{\partial P_\theta} & \frac{\partial \zeta}{\partial P_\zeta} & \frac{\partial \zeta}{\partial \mu} \\ \frac{\partial \psi_p}{\partial \theta} & \frac{\partial \psi_p}{\partial \zeta} & \frac{\partial \psi_p}{\partial P_\theta} & \frac{\partial \psi_p}{\partial P_\zeta} & \frac{\partial \psi_p}{\partial \mu} \\ \frac{\partial v}{\partial \theta} & \frac{\partial v}{\partial \zeta} & \frac{\partial v}{\partial P_\theta} & \frac{\partial v}{\partial P_\zeta} & \frac{\partial v}{\partial \mu} \\ \frac{\partial \lambda}{\partial \theta} & \frac{\partial \lambda}{\partial \zeta} & \frac{\partial \lambda}{\partial P_\theta} & \frac{\partial \lambda}{\partial P_\zeta} & \frac{\partial \lambda}{\partial \mu} \end{vmatrix} = v^2 \mathcal{J} \begin{vmatrix} 1 & 0 & 0 & 0 & 0 \\ 0 & 1 & 0 & 0 & 0 \\ 0 & 0 & \frac{\partial \psi_p}{\partial P_\theta} & \frac{\partial \psi_p}{\partial P_\zeta} & 0 \\ \frac{\partial v}{\partial \theta} & 0 & \frac{\partial v}{\partial P_\theta} & \frac{\partial v}{\partial P_\zeta} & \frac{\partial v}{\partial \mu} \\ \frac{\partial \lambda}{\partial \theta} & 0 & \frac{\partial \lambda}{\partial P_\theta} & \frac{\partial \lambda}{\partial P_\zeta} & \frac{\partial \lambda}{\partial \mu} \end{vmatrix}$$

$$= v^2 \mathcal{J} \left\{ \frac{\partial \lambda}{\partial \mu} \begin{vmatrix} \frac{\partial \psi_p}{\partial P_\theta} & \frac{\partial \psi_p}{\partial P_\zeta} \\ \frac{\partial v}{\partial P_\theta} & \frac{\partial v}{\partial P_\zeta} \end{vmatrix} - \frac{\partial v}{\partial \mu} \begin{vmatrix} \frac{\partial \psi_p}{\partial P_\theta} & \frac{\partial \psi_p}{\partial P_\zeta} \\ \frac{\partial \lambda}{\partial P_\theta} & \frac{\partial \lambda}{\partial P_\zeta} \end{vmatrix} \right\}$$

with

$$\begin{aligned}
\frac{\partial \lambda}{\partial \mu} &= -\frac{\lambda B}{v^2} \\
\frac{\partial v}{\partial \mu} &= \frac{B}{v} \\
\frac{\partial \psi_p}{\partial P_\theta} &= \frac{g}{D} \\
\frac{\partial \psi_p}{\partial P_\zeta} &= -\frac{I}{D} \\
\frac{\partial v}{\partial P_\theta} &= \frac{1}{vD}\left[\rho_{\|} B^2 (1 - \rho_c g' - g\tilde{\alpha}') + g\left\{(\rho_{\|}^2 B + \mu) B' + \tilde{\Phi}'\right\}\right], \\
\frac{\partial v}{\partial P_\zeta} &= \frac{1}{vD}\left[\rho_{\|} B^2 (\rho_c I' + q + I\tilde{\alpha}') - I\left\{(\rho_{\|}^2 B + \mu) B' + \tilde{\Phi}'\right\}\right], \\
\frac{\partial \lambda}{\partial P_\theta} &= \frac{\mu B}{2\lambda D E^2}\left[\rho_{\|} B^2 (1 - \rho_c g' - g\tilde{\alpha}') + g\left\{\left(\frac{1}{2}\rho_{\|}^2 B - \frac{\tilde{\Phi}}{B}\right) B' + \tilde{\Phi}'\right\}\right], \\
\frac{\partial \lambda}{\partial P_\zeta} &= \frac{\mu B}{2\lambda D E^2}\left[\rho_{\|} B^2 (\rho_c I' + q + I\tilde{\alpha}') + I\left\{\left(\frac{1}{2}\rho_{\|}^2 B + \frac{\tilde{\Phi}}{B}\right) + \tilde{\Phi}'\right\}\right],
\end{aligned}$$

and

$$D = \rho_{\|}[gI' - g'I] + I + qg.$$

After a little algebraic manipulation $\mathcal{J}^{(pc)}$ is obtained in the form,

$$\mathcal{J}^{(pc)} = \frac{\mathcal{J} B^2}{D},$$

implying that

$$d\Gamma^{(p)} = \frac{\mathcal{J} B^2}{D}\, d\Gamma^{(c)}. \tag{3.33}$$

The choice of the uniformly loaded phase-space, $\mathcal{U}$, is not unique and is chosen here such that

$$d\mathcal{U} \equiv dv\, d\lambda\, ds\, d\theta\, d\zeta,$$

where $s = \sqrt{\psi_p/\psi_p(a)}$ is a normalized radial coordinate having the dimensions of length and $\psi_p(a)$ is the value of ψ_p at the plasma edge. The volume element of $\mathcal{U}$ associated with each marker, $\Delta\mathcal{U}_j$ is given by

$$\Delta\mathcal{U}_j = \frac{V(\mathcal{U})}{n_p}, \text{ with } V(\mathcal{U}) = \int d\mathcal{U} = (2\pi)^2(v_{max} - v_{min})(\lambda_{max} - \lambda_{min})(s_{max} - s_{min}),$$

and is related (at $t = 0$) to the corresponding canonical phase-space volume element, $\Delta\Gamma_j^{(c)}$ through the relation,

$$\Delta\Gamma_j^{(c)} \equiv \mathcal{J}_j^{(cu)}\,\Delta\mathcal{U}_j,$$

where $\mathcal{J}^{(cu)}$ is found through an analogous procedure to that used to find $\mathcal{J}^{(pc)}$ to be,

$$\mathcal{J}^{(cu)} = 4\pi\frac{s\psi_p(a)Dv^2}{B^2}.$$

The relationship between the various phase-space elements, $\Delta\Gamma_j^{(p)}$, $\Delta\Gamma_j^{(c)}$ and $\Delta\mathcal{U}_j$ can be summarized as

$$\Delta\Gamma_j^{(p)} \equiv \mathcal{J}_j^{(pc)}(t)\,\underbrace{\mathcal{J}_j^{(cu)}(0)\,\Delta\mathcal{U}_j}_{\Delta\Gamma_j^{(c)}(0)},$$

and is schematically depicted in Fig. 3.4.

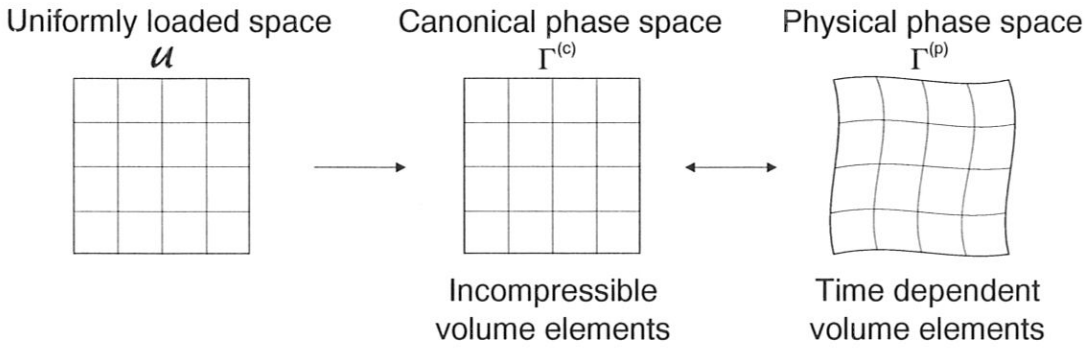

Figure 3.4: Markers are uniformly loaded throughout some arbitrary phase space $\mathcal{U}$ and the volume element $\Delta\mathcal{U}_j$ associated with each calculated. These elements are then related to the incompressible canonical volume elements $\Delta\Gamma_j^{(c)}$ which are subsequently related to the physical phase-space volume elements $\Delta\Gamma_j^{(p)}$ at all later times.

The programme described above is suitable for use with an arbitrary analytic distribution function f_0, however in special cases where f_0 is highly anisotropic in one of the dimensions then additional simplification becomes possible. The fast particle distribution that arises as a result of neutral beam injection (NBI) can be highly anisotropic with all the injected particles' velocity vectors distributed within a narrow cone around

$\lambda = 1$. The assumption that the velocity distribution is uni-directional permits one of the velocity dimensions to be integrated out, with the consequence that the phase-spaces required to describe the distribution become 4-D. The volume elements and Jacobians used to represent general and uni-directional velocity distributions are summarized in Table 3.1.

Quantity	General	Uni-directional
$d\mathcal{U}$	$dv\, d\lambda\, ds\, d\theta\, d\zeta$	$dv_{\|\|}\, ds\, d\theta\, d\zeta$
$d\Gamma^{(c)}$	$2\pi\, d\mu\, d\theta\, dP_\theta\, d\zeta\, dP_\zeta$	$2\pi\, d\theta\, dP_\theta\, d\zeta\, dP_\zeta$
$d\Gamma^{(p)}$	$2\pi\, v^2\, dv\, d\lambda\, \mathcal{J}\, d\psi_p\, d\theta\, d\zeta$	$2\pi\, v_{\|\|}^2\, dv_{\|\|}\, \mathcal{J}\, d\psi_p\, d\theta\, d\zeta$
$\mathcal{J}^{(cu)}$	$4\pi\, s\psi_p(a) D v^2/B^2$	$4\pi\, s\psi_p(a) D/B$
$\mathcal{J}^{(pc)}$	$\mathcal{J}B^2/D$	$v_{\|\|}^2 \mathcal{J}B/D$

Table 3.1: Volume elements and Jacobians used to represent general and beam-like ($\lambda \equiv 1$) distributions of fast particles.

The inclusion of the δf formalism into the model modifies the wave equations derived in §3.3.1 such that they become,

$$\dot{\mathcal{X}}_k = \frac{1}{2E_k} \sum_{j=1}^{n_p} \delta f_j \Delta\Gamma_j^{(p)} \sum_m (k_{\|m} v_{\|j} - \omega_k) S_{jkm}, \tag{3.34a}$$

$$\dot{\mathcal{Y}}_k = -\frac{1}{2E_k} \sum_{j=1}^{n_p} \delta f_j \Delta\Gamma_j^{(p)} \sum_m (k_{\|m} v_{\|j} - \omega_k) C_{jkm}. \tag{3.34b}$$

As can be seen the only difference from equations (3.30) is the inclusion of the additional weighting factor $\delta f_j \Delta\Gamma_j^{(p)} = \delta n_j$, representing the change in the distribution function at each marker location.

3.4.1 Loading Phase-space $\mathcal{U}$

Perhaps the most common way to initialise a uniform distribution of n_p markers over each of the dimensions of the hyperspace $\mathcal{U}$ is to use a pseudo-random number generator to produce a uniform distribution over the interval (0,1) and then to map this to the desired interval. Intuitively, this approach models the random distribution of actual plasma particles and has the advantage of being convenient since pseudo-random number generators are widely available. However, random starts such as these have the disadvantage of introducing noise levels that are often too large to permit the observation of subtle physical effects such as wave growth. In what have become known as 'quiet starts', an effort is made to eliminate this noise by achieving a distribution that is closer to a uniform distribution. An elementary way of achieving this is by regularly loading the particles upon a regular lattice, however, this creates problems of

it's own since regular patterns of beams are produced in each of the dimensions leading to aliasing errors. This problem can be overcome by staggering each layer of the lattice, although for the full physical 6-dimensional case this in itself is not trivial.

There are many ways of approximating a continuous distribution function over a phase-space Γ by a finite set of n_p points, $\omega_{n_p} \equiv \{(\mathbf{x}_1, \mathbf{v}_1), \ldots (\mathbf{x}_{n_p}, \mathbf{v}_{n_p})\}$ such that the number of points σ, in any region of phase-space $\mathcal{R}$ tends, in the limit of an infinite number of points, to the integrated distribution function. i.e.

$$\lim_{n_p \to \infty} \sum_{\mathcal{R}} \frac{f(x_i, v_i)}{n_p} = \int_{\mathcal{R}} f \, d\mathbf{x} \, d\mathbf{v},$$

where f is normalized such that

$$\int_{\Gamma} f \, d\mathbf{x} \, d\mathbf{v} = 1.$$

From a physical point of view, proof of convergence as $n_p \to \infty$ is not actually needed, since plasmas are themselves discrete. Indeed, the whole argument can be turned around to prove the validity of the continuous Vlasov formulation for discrete plasmas!

A convenient approach is to make use of an analytically defined, multi-dimensional, low-discrepancy[1] sequence, an example of which is Hammersley's sequence [70]. This is an N-dimensional sequence generated using radical-inverse functions $\phi_r(i)$, where r is a prime number: if the integer i is written in base r,

$$i = a_0 + a_1 r + a_2 r^2 + \cdots$$

then

$$\phi_r(i) = a_0 r^{-1} + a_1 r^{-2} + a_2 r^{-3} + \cdots$$

Hammersley's sequence is given by

$$x_i = \{i/n_p, \phi_2(i), \ldots, \phi_{P(N-1)}\},$$

where $2, \ldots, P(N-1)$ denote the first $N-1$ primes and in order to make these distributions symmetric over the interval $(0, 1)$ in each of the dimensions, $1/2n_p$ is added to each of the coordinates. This method of loading achieves a discrepancy $\propto 1/n_p$, whereas a random distribution has a discrepancy $\propto 1/\sqrt{n_p}$, indicating faster convergence to a uniform continuum of markers than random methods [71].

Each of the radical-inverse functions, $\phi_r(i)$, has a periodicity associated with it that is equal to it's associated base, r. Hence, in order to fill an N-dimensional hypercube, the number of points chosen should be a multiple of K, where

$$K = \prod_{n=1}^{N} P(n-1).$$

[1] This is a measure of the departure from uniform using measure and number theory methods [71].

Thus for the general case where the phase-space $\mathcal{U}$ is 5-D, it should be ensured that a multiple of 210 markers is selected to fill the phase-space. The actual number of particles required for a given simulation depends upon the accuracy of the answer required and the computational time available. In practice several different runs are compared to demonstrate that convergence with respect to particle number has taken place. An example of this bit-reversal loading scheme is illustrated in Fig 3.5 where 210 markers have been uniformly loaded within a 5-D hypercube. For comparison, Fig. 3.6

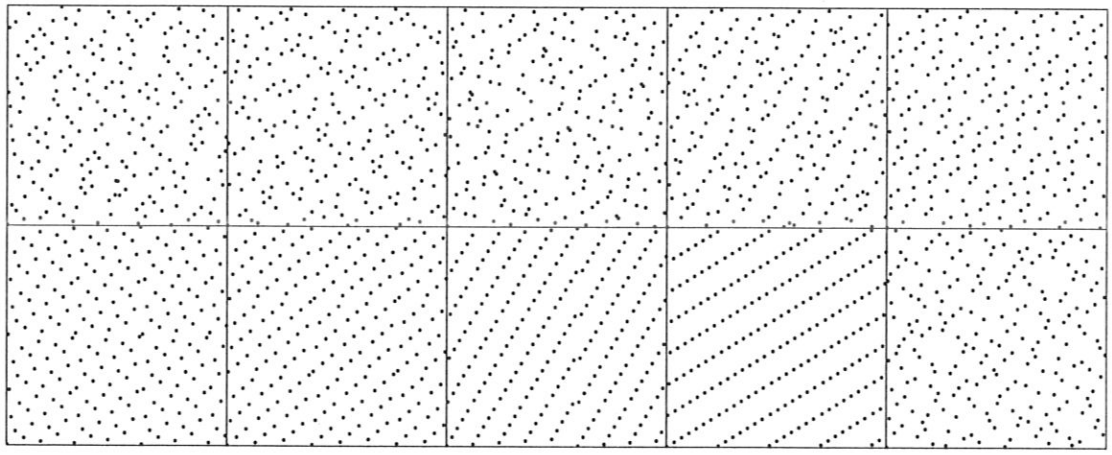

Figure 3.5: 2-D projections of a uniformly loaded 5-D hypercube with 210 markers.

depicts the same hypercube uniformly distributed with markers using a pseudo-random number generator.

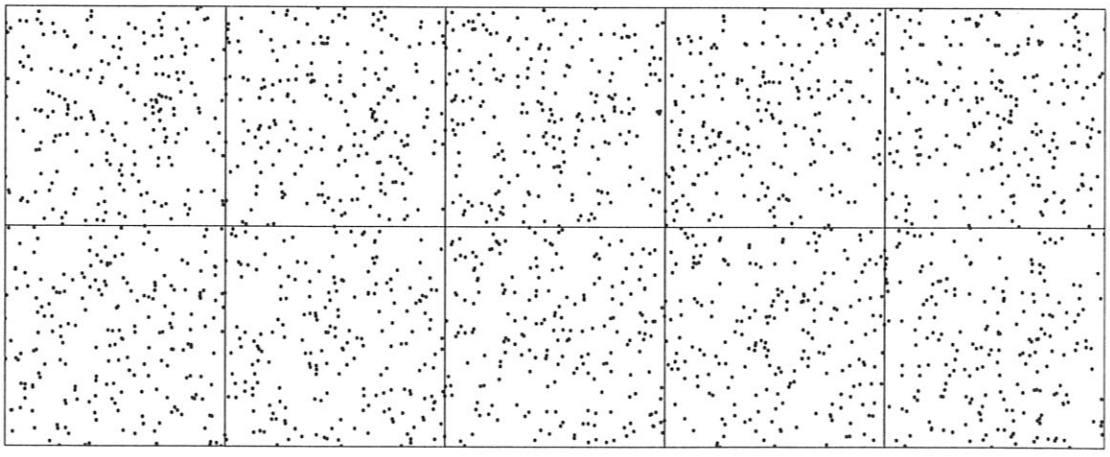

Figure 3.6: 2-D projections of a pseudo-randomly loaded 5-D hypercube with 210 markers.

3.4.2 Representation of Particle Distributions

The distribution of fast particles is specified through the analytic distribution function f_0, which as indicated above is defined in terms of the unperturbed constants of the motion. In general however, it is more natural to specify the distribution function in terms of a radial flux function and the particle energy. This can be achieved by constructing an expression representing an averaged radial flux value $\langle\psi_p\rangle$ in terms of the constants of the motion, allowing f_0 to be written as,

$$f_0 = f_0(\langle\psi_p\rangle, \mathcal{E}^{(0)}; \mu).$$

Clearly the best choice for $\langle\psi_p\rangle$ is the time-averaged ψ_p value but to avoid the computational overhead associated with calculating $\langle\psi_p\rangle$ for each particle it is more convenient to construct an approximate prescription for it in terms of the constants of the motion. This will necessarily depend upon the orbit topology of the particle under consideration. The definition, $P_\zeta^{(0)} = g\rho_{||} - \psi_p$, allows the averaged value of $\langle\psi_p\rangle$ to be written as,

$$\langle\psi_p\rangle = \left\langle \frac{\sigma g(\psi_p)}{B(\psi_p,\theta)} \sqrt{2\left[\mathcal{E} - \mu B(\psi_p,\theta)\right]} \right\rangle - P_\zeta^{(0)},$$

where σ is the sign of $v_{||}$. For trapped particles it is sufficient to define $\langle\psi_p\rangle$ as the values of ψ_p at the tips of their orbits where $v_{||} = 0$, since this is where the particles spend the majority of their time. To lowest order in an inverse-aspect-ratio expansion the definitions covering all classes of particle may be summarized as,

$$\langle\psi_p\rangle = \begin{cases} \sqrt{2(\mathcal{E}-\mu)} - P_\zeta^{(0)}, & \text{for } \mathcal{E} > \mu \quad \text{(Co-passing)} \\ -P_\zeta^{(0)}, & \text{for } \mathcal{E} < \mu \quad \text{(Trapped)} \\ -\sqrt{2(\mathcal{E}-\mu)} - P_\zeta^{(0)}, & \text{for } \mathcal{E} > \mu \quad \text{(Counter-passing)} \end{cases}$$

which corresponds to the $\langle\psi_p\rangle$ surfaces indicated in Fig. 3.7. A simple form for f_0 ex-

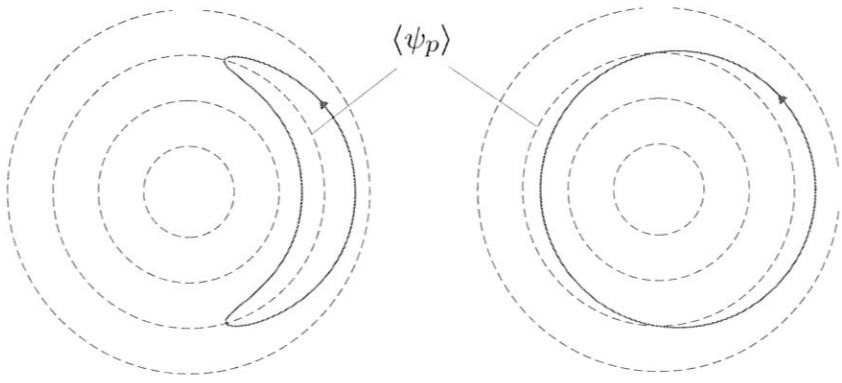

Figure 3.7: Characteristic ψ_p values, $\langle\psi_p\rangle$, for trapped and passing particles.

ploiting these definitions is to specify f_0 as the product of a radial distribution function $h_1(\psi_p)$ and an energy distribution function $h_2(\mathcal{E})$:

$$f_0 = C\, h_1(\psi_p)\, h_2(\mathcal{E}), \tag{3.35}$$

where C is determined by specifying a global parameter such as the volume averaged fast particle beta $\langle \beta_f \rangle$, or the ratio of the number of fast ions to the number of background ions, n_f/n_i. The form used in equation (3.35) is sufficient to represent the main types of energetic particle distributions typically found in tokamaks such as those classified in Table 3.2. These distributions are found by solving the Fokker-Planck equation [17, 18]

Source	**Physical Mechanism**	**Spatial Distribution**	**Angular Distribution**	**Initial Energy**
α-particles	Fusion reactions	Centrally peaked	Isotropic	3.52 MeV
Neutral beam injection	Charge exchange, electron impact ionization	Depends upon energy and line density	Anisotropic (depends upon injection angle)	Injection energies
ICRF minority heating	Cyclotron damping	Peaked near resonance layer	Anisotropic (perpendicular)	—

Table 3.2: Principal sources of fast ions.

with each identified by the particle heating method used since they lead to very different particle distributions. In a realistic device, the actual distribution would generally be some combination of these three forms, with the external heating methods dominating the distribution until sufficient levels of fusion power were produced that they could be turned off. Even in this idealistic scenario it may be advantageous to retain some sources of external heating as a method of helium ash control.

3.5 Summary

In this chapter all the components necessary to construct the model describing the interaction of a distribution of fast particles with a set of AE have been derived. In §3.1 and §3.2 the Boozer coordinate system defined by the magnetic field structure was introduced and shown to lead to a simple Hamiltonian guiding centre description of the fast particle motion. The response of the AE present to their interaction with the distribution of fast particles was formulated in §3.3, whilst in §3.4 it was demonstrated how the whole model may be cast in terms of the δf formalism to enhance it's numerical properties.

Chapter 4

Implementation of Model

The model developed in the preceding chapter forms an initial value problem comprised of a system of $5 \times n_p + 2 \times n_w$ first order ordinary differential equations together with appropriate initial conditions. The code written to perform the task of solving them is HAGIS, (HAmiltonian GuIding centre System.) It takes the specified initial conditions together with equations (3.26), (3.31) and (3.34) to simultaneously advance the spatial location of each marker, its parallel velocity, and the change in the distribution function at that position, as well to update the amplitude and phase of each wave present. The input data required by the HAGIS code consists of three parts; the equilibrium field data, the perturbed field data, and the fast particles' initial conditions. The first of these, the equilibrium data is supplied by the HELENA code [48] by solving the Grad-Shafranov equation [3] and the second by the MHD stability code CASTOR [49]. The initial distribution of energetic ions and the initial amplitude and phase of each of the waves are specified in an input data file supplied by the user. An overview of the data handled by the HAGIS code and the other codes which supply it is shown in Fig. 4.1.

All values and derivatives of the plasma equilibrium required by the code are calculated by splining the equilibrium data using standard finite difference approximations. Since the equilibrium is toroidally symmetric this is only necessary over the poloidal plane; 1-D data using radial cubic spline interpolation, and 2-D data using bi-cubic splines with appropriate boundary conditions in the poloidal direction. The HAGIS code uses a 4th order Runge-Kutta integration algorithm chosen in preference to more sophisticated adaptive methods since if the phase-space is properly loaded there is a homogeneity associated with the differential equations that must be advanced at each time step and there is no advantage in making modifications to the step size. Higher order methods were rejected upon performance grounds. The accuracy achievable by the model is shown to scale correctly with the integrator step size used and is ultimately limited by the accuracy of the spline representation.

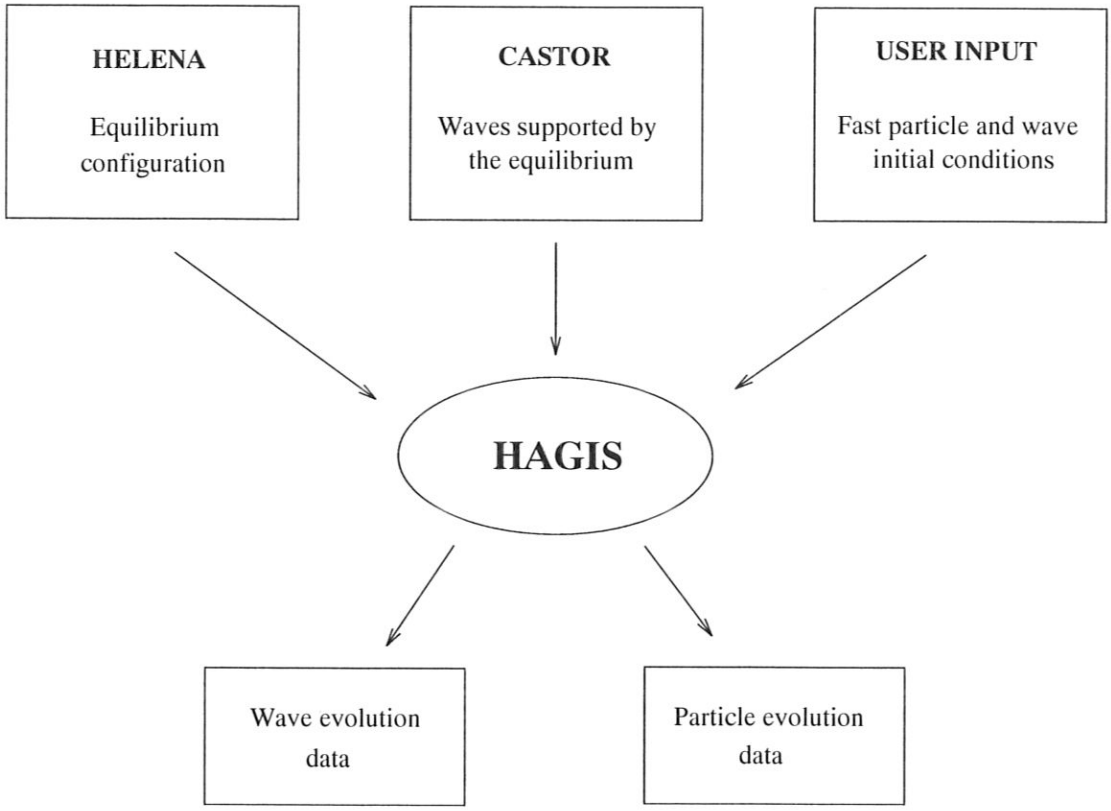

Figure 4.1: Overview of the HAGIS code showing flow of data.

4.1 Code Validation

To verify the computational implementation of the numerical model and assess its accuracy, the HAGIS code has been extensively tested and validated. In this section the details of these tests and comparisons with previous numerical and analytic results are presented.

In the first section the accuracy of the integration algorithm used is assessed by examining the conservation of various system invariants. This is followed by an examination and comparison of various particle trajectories for which the exact orbits are known, allowing the implementation of equations (3.26) that describe the particle motion to be verified. From a consideration of the behaviour of a single particle in the presence of a fixed amplitude single harmonic wave, it is then possible to test that the correct wave-particle interaction is taking place. The final tests performed were benchmark comparisons with other codes. These represented the ultimate testing ground since they covered the full spectrum of the codes abilities and proved invaluable for detecting subtle coding errors that had eluded detection during previous tests.

4.1.1 Integrator Performance and System Invariants

The integrator used within the HAGIS model determines the evolution of all the quantities advanced within the model. Consequently a stringent examination of its performance was paramount before any further tests of the code were made. One of the easiest tests to achieve this goal is to examine how well the code conserves various system invariants. In the absence of any field perturbations all the particles can be expected to conserve both energy and toroidal angular momentum since a stationary magnetic field can do no work upon the particles and the equilibria are toroidally symmetric. However, in the presence of a single distinct toroidal eigenfunction with label k,

$$\phi_{jkm} \sim e^{i(n_k\zeta_j - m\theta_j - \omega_k t)},$$

particle energy is no longer conserved since $d\mathcal{E}/dt = \partial\mathcal{H}/\partial t \neq 0$. Similarly, ζ_j is no longer a cyclic coordinate and the toroidal component of canonical angular momentum is also not conserved. Thus particle energy and angular momentum can no longer be used as a measure of the code's performance. However due to the use of the above ansatz, the field perturbation rotates around the equilibrium field's axis of symmetry and a new constant of the motion exists. This can be seen be observing that for a single particle j, the differential operator

$$\partial_t + (\omega_k/n_k)\partial_{\zeta_j} \equiv 0,$$

from which the result

$$\frac{d}{dt}\left(\mathcal{E}_j - \frac{\omega_k}{n_k}P_{\zeta j}\right) = 0$$

follows by acting on the particle Hamiltonian with the above operator. Hence for each particle,

$$\mathcal{E}_j - (\omega_k/n_k)P_{\zeta_j} = K_j,$$

where K_j is some constant. The additional rotation of the field perturbation in the poloidal direction does not give rise to further constants of the motion due to the inhomogeneity of the equilibrium field with respect to the poloidal angle.

Simulations with a single co-passing ($\lambda = 1$) α-particle in the JET equilibrium summarized in Table 4.1 have been performed in the presence of a single fixed amplitude

Parameter	Value
ε	0.334
R_0	3.0 m
B_0	2.87 T
q_0	0.87

Table 4.1: JET equilibrium parameters used for examination of integrator performance

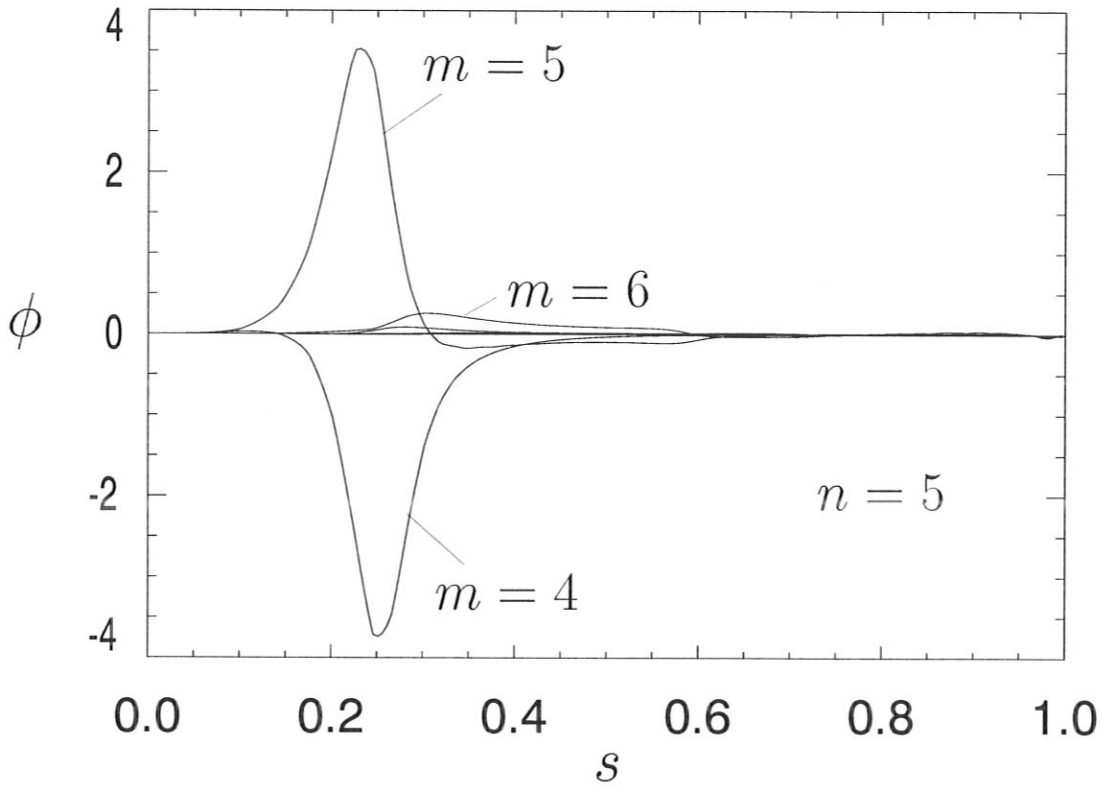

Figure 4.2: Principle poloidal harmonics of the $n = 5$ KTAE eigenfunction in JET.

($\delta B/B = 10^{-4}$) $n = 5$ KTAE shown in Fig. 4.2. The scaling of $\mathcal{E}_j - \frac{\omega_k}{n_k} P_{\zeta j}$ with the integrator step size used (measured in terms of the number of steps per wave period) is as shown in Fig. 4.3, showing convergence down to the accuracy of the spline representation which is close to machine precision. The HAGIS code employs a fixed time step 4th order Runge-Kutta integration algorithm and as expected the error scales as approximately $\mathcal{O}(h^5)$, where h is the time step size. The run time of a particular simulation is inversely proportional to the size of h chosen. Thus as a compromise between run time and accuracy, h is typically chosen such that the integrator makes 64 steps per wave period.

Despite the fact that the energy and the toroidal component of canonical angular momentum is not conserved for individual particles, the total energy and angular momentum of the wave-particle system is still conserved as it must be for any isolated system. By considering the variation in P_ζ for a single particle j due to a single toroidal harmonic k as described by equation (3.29),

$$\dot{P}_{\zeta jk} = -\frac{\partial \mathcal{L}}{\partial \zeta_j} = -\frac{\partial \mathcal{H}}{\partial \zeta_j}$$

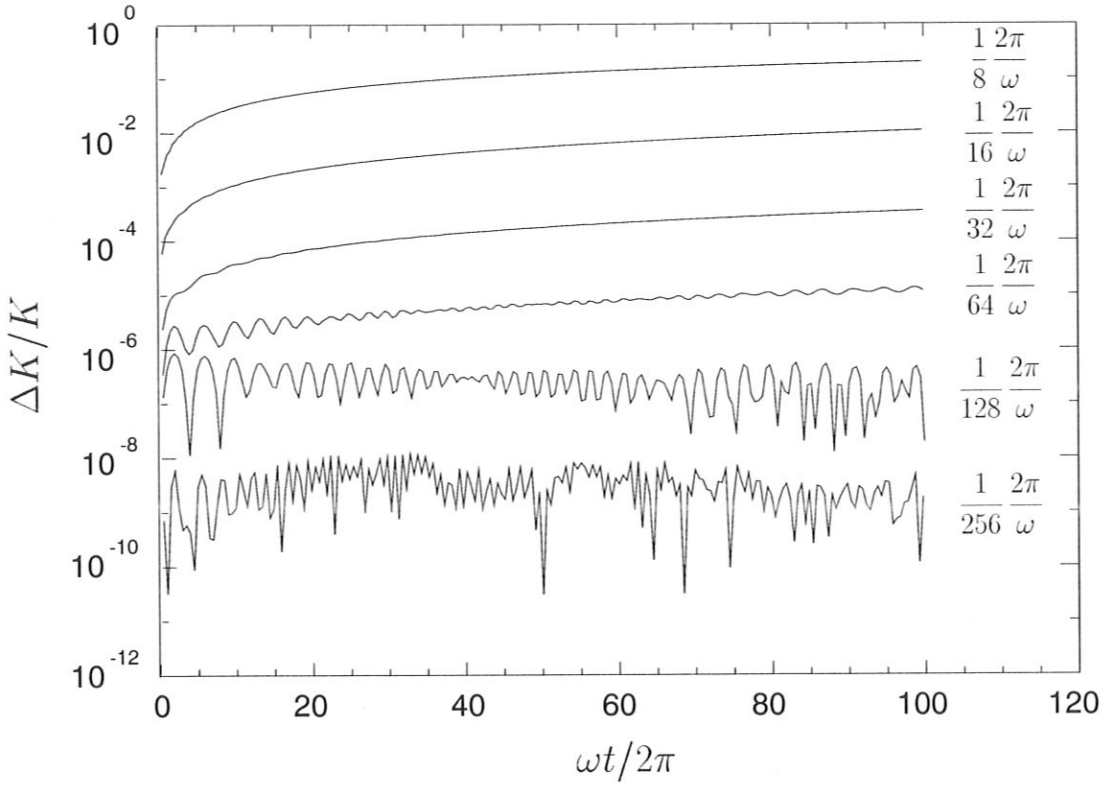

Figure 4.3: Plot showing the scaling of the conservation of $\mathcal{E}_j - (\omega_k/n_k)P_{\zeta j} = K$ with time measured in terms of the number of wave periods, for various integrator step sizes, h.

$$= -\frac{n_k}{\omega_k}\sum_m \left(k_{\|m}v_{\|j} - \omega_k\right)\left[\mathcal{X}_k S_{jkm} - \mathcal{Y}_k C_{jkm}\right]$$

it follows that in the presence of a spectrum of waves the total rate of change of canonical toroidal momentum for a particle j may be written as

$$\dot{P}_{\zeta j} = \sum_{k=1}^{n_w} \dot{P}_{\zeta jk}.$$

Now, the rate of change of particle energy,

$$\begin{aligned}
\dot{\mathcal{E}}_j &= \frac{\partial \mathcal{H}_j}{\partial t} = -\frac{\partial \mathcal{L}_j}{\partial t} = -\frac{\partial \mathcal{L}_{int_j}}{\partial t} \\
&= -\sum_{k=1}^{n_w}\sum_m \left(k_{\|m}v_{\|j} - \omega_k\right)\left[\mathcal{X}_k S_{jkm} - \mathcal{Y}_k C_{jkm}\right] \\
&= \sum_{k=1}^{n_w} \frac{\omega_k}{n_k}\dot{P}_{\zeta jk}
\end{aligned}$$

Thus the total rate of change of particle energy is

$$\dot{\mathcal{E}}_p = \sum_{j=1}^{n_p} \sum_{k=1}^{n_w} \frac{\omega_k}{n_k} \dot{P}_{\zeta jk}$$

which may be written as,

$$\dot{\mathcal{E}}_p = -\sum_{j=1}^{n_p} \sum_{k=1}^{n_w} \sum_{m} \left(k_{\|m} v_{\|j} - \omega_k \right) \left[\mathcal{X}_k S_{jkm} - \mathcal{Y}_k C_{jkm} \right].$$

The energy of a single wave $\mathcal{E}_k$ is given by

$$\mathcal{E}_k = A_k^2 E_k,$$

from which it follows using equations (3.30) that

$$\begin{aligned} \dot{\mathcal{E}}_k &= 2E_k \left(\mathcal{X}_k \dot{\mathcal{X}}_k + \mathcal{Y}_k \dot{\mathcal{Y}}_k \right) \\ &= \sum_{j=1}^{n_p} \sum_{m} \left(k_{\|m} v_{\|j} - \omega_k \right) \left[\mathcal{X}_k S_{jkm} - \mathcal{Y}_k C_{jkm} \right]. \end{aligned}$$

Summing over all the waves in the system gives the total change in the wave energy as,

$$\begin{aligned} \dot{\mathcal{E}}_w &= \sum_{k=1}^{n_w} \dot{\mathcal{E}}_k \\ &= \sum_{k=1}^{n_w} \sum_{j=1}^{n_p} \sum_{m} \left(k_{\|m} v_{\|j} - \omega_k \right) \left[\mathcal{X}_k S_{jkm} - \mathcal{Y}_k C_{jkm} \right] \\ &= -\sum_{j=1}^{n_p} \frac{\omega_k}{n_k} \dot{P}_{\zeta jk} \\ &= -\dot{\mathcal{E}}_p. \end{aligned}$$

Hence,

$$\frac{d}{dt} \left(\mathcal{E}_p + \mathcal{E}_w \right) = 0$$

and the conservation of system energy is demonstrated. The analogous relation for the conservation of system momentum follows in a similar manner. It is apparent from the above derivation that Fig. 4.3 may be equivalently viewed as a plot showing the conservation of the total system energy with integrator step size.

4.1.2 Particle Trajectories

With the successful implementation of the integrator demonstrated, the next tests undertaken compare various particle trajectories in an equilibrium field with those

predicted by theory. These tests confirm that the equilibrium field has been correctly represented and that the equations of motion correctly describe the particles spatial trajectories. To aid comparisons with theoretical predictions they were performed in a large aspect ratio tokamak possessing circular flux surfaces and with the parameters as in Table 4.2.

Parameter	Value
ε	0.01
R_0	3.0 m
B_0	2.87 T
q_0	0.87

Table 4.2: Equilibrium parameters used for particle comparisons

Theoretical predictions of the particle trajectories are obtained by eliminating $\rho_{||}$ from the conservation relations for energy and momentum, $\mathcal{E} = 1/2\rho_{||}^2 B^2 + \mu B$ and $P_\zeta = g\rho_{||} - \psi_p$ to obtain an equation for $\psi_p = \psi_p(\theta)$. Whilst this is an easy way to obtain the orbit topology, no time evolution is given. This is analogous to the consideration of a pendulum where obtaining the time evolution requires the integration of an elliptic function, whilst the range over which the particle will swing is immediately obvious from a consideration of the energy in the system.

Three particles were selected for these tests, chosen because of the unusual topology of their trajectories enabling deviations in their orbits to be immediately identified. All of the test particles were launched at a major radius $R = 3.025$ m upon the out-board mid-plane ($\theta = 0$) with their energy components as described in Table 4.3. Each of the

Particle	$\mathcal{E}$	$\mathcal{E}_\perp$
I	170 eV	40 eV
II	50 eV	49.585 eV
III	164 eV	161.832 eV

Table 4.3: Parameters used for comparing particle orbits

particles was followed for a period of 1 second during which time they made 234, 479, and 63 complete poloidal transits respectively.

The trajectory I is a very fat banana orbit close to the trapped/passing boundary. That is, as the particle moved poloidally around the magnetic axis it entered the stronger field region on the inboard side, and was reflected due to the mirror force as shown in Figs. 4.4 and 4.5. The orbits are visually indistinguishable even when overlaid, indicating that the particle has bounced in the same location.

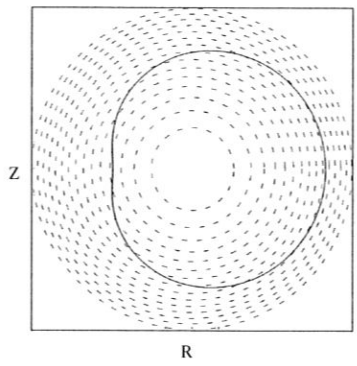

Figure 4.4: HAGIS trajectory I

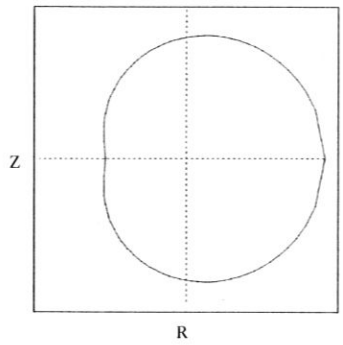

Figure 4.5: Analytic trajectory I

Trajectory II is that traced out by a particle with energy and magnetic moment chosen such that it is reflected at the vertical surface passing through the magnetic axis. Particles with trajectories such as these are sometimes referred to as 'potato' orbits and as before, the orbit shown in Fig. 4.6 is visibly indistinguishable from the analytical trajectory shown in Fig. 4.7.

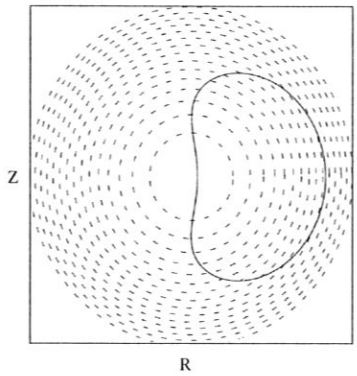

Figure 4.6: HAGIS trajectory II

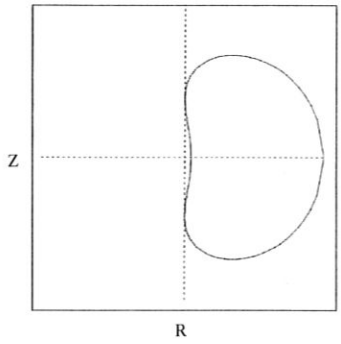

Figure 4.7: Analytic trajectory II

The final trajectory analysed is that of the pathological banana orbit known as the 'pinch' orbit and is shown in Figs. 4.8 and 4.9. This type of orbit constitutes a particularly difficult test of the code's abilities since the particle spends a long time at the tips of this rather extreme banana and any error would visibly modify the particle orbit such that it either becomes more deeply trapped, or so that it became an axis-encircling passing particle.

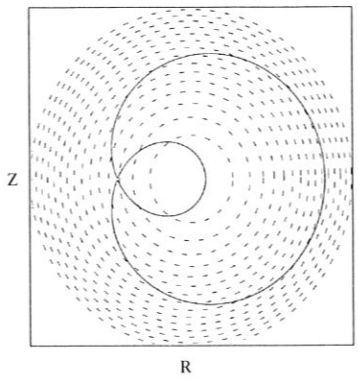

Figure 4.8: HAGIS trajectory III

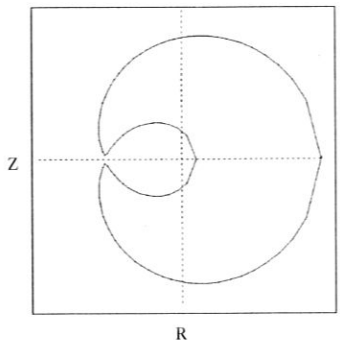

Figure 4.9: Analytic trajectory III

These tests have demonstrated that the HAGIS code accurately reproduces single particle trajectories. The results are visually indistinguishable from analytical predictions and integration errors are negligible.

4.1.3 Magnetic Island Formation

The inclusion of a small helical magnetic perturbation changes the topology of the magnetic field structure such that it no longer possesses nested flux surfaces. In particular, magnetic islands may form upon the flux surfaces for which the field lines are orthogonal to the wave vector of the perturbation since no energy is required to bend the magnetic field lines. In this section an expression for the width of these island is derived which is used to compare with the islands found using the HAGIS code.

To illustrate the destruction of nested flux surfaces, consider a small time independent perturbation of the poloidal flux function described by the perturbation parameter $\tilde{\alpha}$. When decomposed into Fourier harmonics and written in terms of the unperturbed toroidal flux, ψ this becomes,

$$\Psi_p = \int \frac{1}{q} d\psi - \sum_{m,n} \alpha_{mn} e^{i(n\zeta - m\theta)}.$$

From equations (3.2) this implies that the field lines are described by the equations,

$$\frac{d\psi}{d\zeta} = \sum_{m,n} im\alpha_{mn} e^{i(n\zeta - m\theta)}, \qquad \frac{d\theta}{d\zeta} = \frac{1}{q},$$

and from equation (3.1) that

$$\mathbf{B} \cdot \nabla\psi = \frac{1}{\mathcal{J}} \sum_{m,n} im\alpha_{mn} e^{i(n\zeta - m\theta)},$$

indicating that the perturbation has introduced a small component of $\mathbf{B}$ across the original flux surfaces. If α_{mn} is finite and q is not close to a rational surface $q = m/n$, then q may be approximated by a constant and the equations integrated to give,

$$\theta = \frac{\zeta}{q} + \theta_0,$$

and

$$\psi = -\sum_{m,n} \frac{m\alpha_{mn} q e^{i(n\zeta - m\theta)}}{m - nq} + \psi_0.$$

The flux surfaces are thus distorted but remain topologically nested. If $m - nq(\psi) \approx 0$ however, the resonant denominator creates large excursions in ψ and this solution is not valid.

Restricting attention to a single harmonic described by the mode numbers m and n, it is seen from above that this will be resonant upon the surface where $q = m/n$. Field lines upon this surface define a helix and $\chi = \theta - n\zeta/m$ is a convenient angular coordinate orthogonal to this helix (parallel to $\mathbf{k}_\perp$ upon this surface). Expanding q around ψ_0 such that

$$q(\psi) = \frac{m}{n} + \frac{dq}{d\psi}(\psi - \psi_0)$$

gives

$$\frac{d\chi}{d\zeta} = -\left(\frac{n^2 q'}{m^2}\right)(\psi - \psi_0), \qquad \text{and} \qquad \frac{d\psi}{d\zeta} = im\alpha e^{-im\chi},$$

where $q' = dq/d\psi$. These equations may be integrated to give,

$$(\psi - \psi_0)^2 = \frac{2m^2}{n^2 q'}\alpha\left[e^{-im\chi} + c\right],$$

where c is a constant determined by the initial position. A useful plot often made when examining island structures is the Poincaré puncture plot. This is formed by plotting the position of a field line in the ψ, θ plane at a particular toroidal angle ζ at successive transits of the device. For such a plot at $\zeta = 0$, it is seen from the definition of χ that $\chi = \theta$. Expanding near $\theta = l\pi/m$, $l \in \mathcal{Z}$ it is found that

$$(\psi - \psi_0)^2 + \frac{\alpha m^2}{n^2 q'}(m\theta)^2 = constant,$$

which for $\alpha/q' > 0$ and $c < 1$ describes elliptical surfaces, whilst for $c > 1$ describes hyperbolic surfaces. As shown in Fig. 4.10 a chain of 'magnetic islands' is formed along the $q = m/n$ surface which is separated from the toroidally nested surfaces by a separatrix. The width of this separatrix is found by choosing $c = 1$ above to give,

$$\Delta\psi = \frac{4m}{n}\sqrt{\left(\frac{\alpha}{q'}\right)}. \tag{4.1}$$

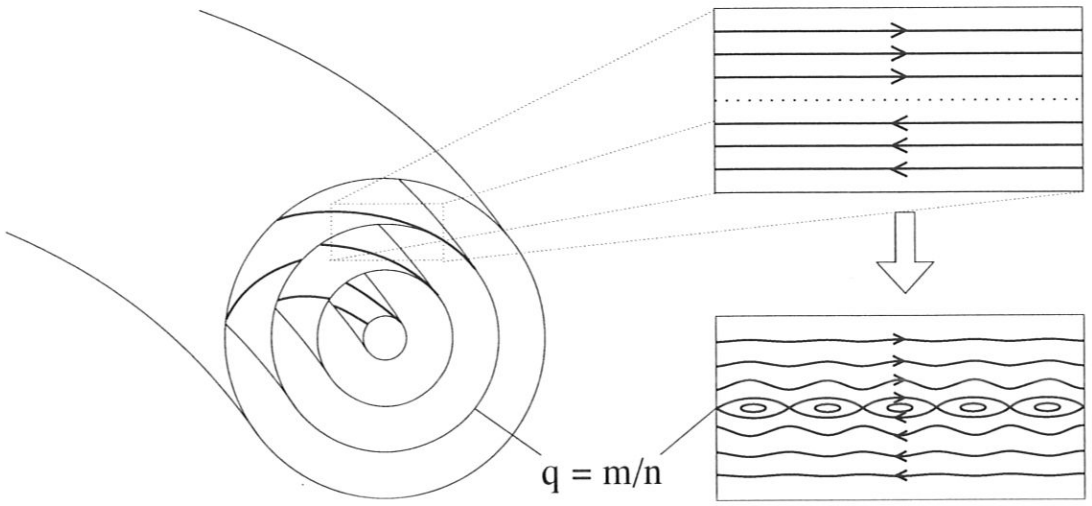

Figure 4.10: Magnetic field structure due to a perturbation described by the mode number m, n showing the chain of islands formed.

To compare numerically obtained island widths using the HAGIS code with theoretical estimates found using equation (4.1), a relatively large aspect ratio $\varepsilon = 0.1$ circular boundary equilibrium is employed, to which an $n = 3$ wave is applied with magnitude $\delta B/B = 2.5 \times 10^{-4}$ at the $q = 4/3$ surface. By using very low energy (1 eV) deeply passing particles for which the adiabatic invariant, μ, was zero, it was possible to obtain particles that, to a good approximation, effectively followed the field lines. By launching particles close to the $q = 4/3$ surface, and using the HAGIS code to calculate their trajectories, it was possible to produce a Poincaré puncture plot which allowed the island structure formed to be easily seen, as in Fig. 4.11. In real space, this island had a width of 2.0 cm, which was in good agreement with that calculated analytically using equation (4.1) which predicted a width of 2.2 cm.

In the presence of many different Fourier harmonics m and n the magnetic flux surfaces break up into islands at each rational surface where $q = m/n$. The nonlinear interaction of two island chains with $q = m_1/n_1$ and m_2/n_2 produces a smaller island chain at the surface $q = (m_1 + m_2)/(n_1 + n_2)$. This leads to a Fibonacci sequence of surfaces at which islands form, generated by the original mode numbers. As the perturbation size increases the island widths grow until neighbouring chains start to overlap and the field becomes stochastic. Field lines within a stochastic region wander around throughout some volume forming a region with very poor confinement properties.

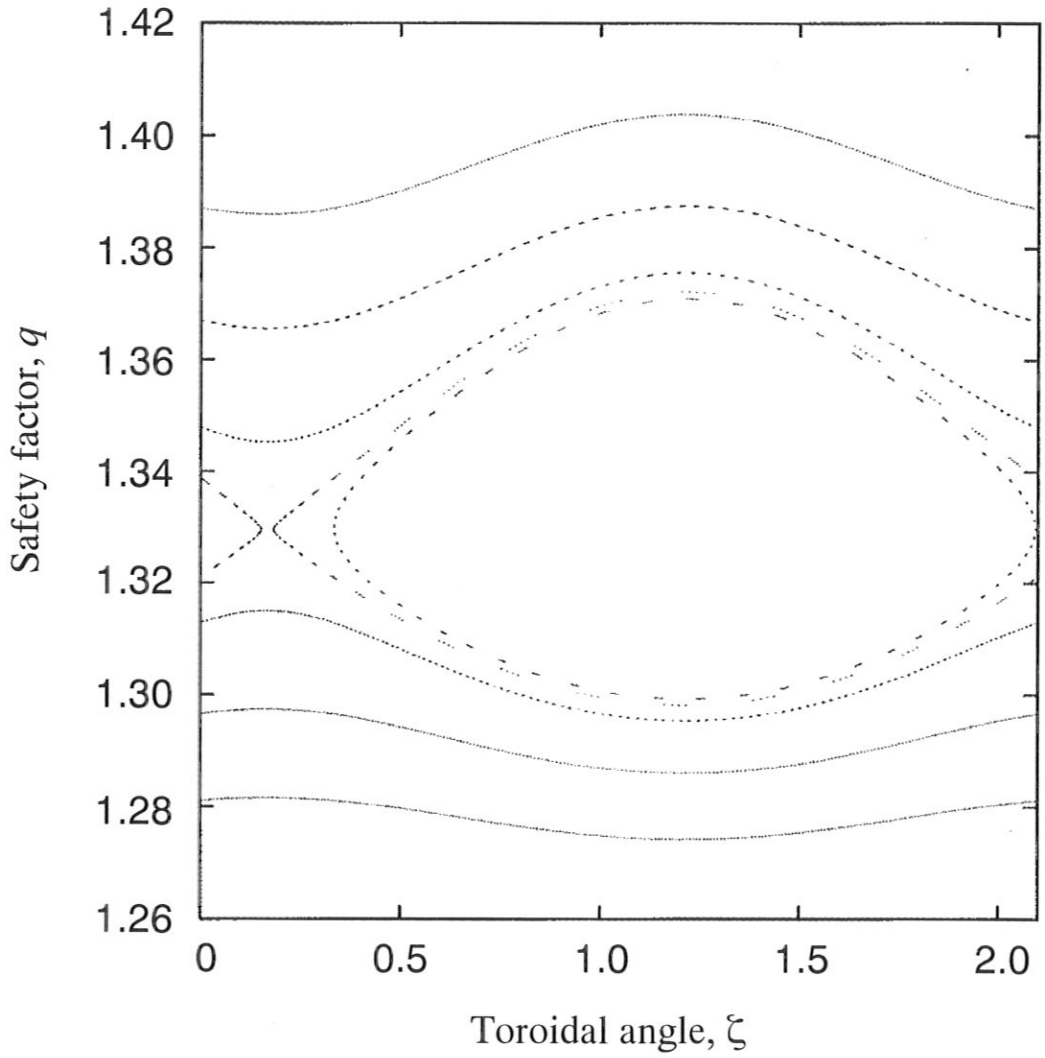

Figure 4.11: Magnetic island in the $\theta = 0$ plane at $q = 4/3$.

4.1.4 Side-band Resonances

Particles with higher energies and pitch angles experience increased drifts and their motion is no longer coincident with a single flux surface. If the excursion in safety factor, Δq, is large enough it is possible to obtain resonant island structures shifted away from the original resonant surfaces known as side-band resonances.

The resonance condition that the particle always sees the same phase of the perturbing wave is described by equation (2.14). In the large aspect ratio, circular flux surface limit this defines the radial position of an island as,

$$q(\psi_p) = \frac{m+l}{n} \frac{1}{1-\omega R/nv_{||}}, \tag{4.2}$$

where $v_{||}$ is the particle's velocity parallel to the magnetic field, R is the major radius, m and n are the poloidal and toroidal mode numbers, l is an integer value corresponding to the different side-band resonances arising from the radial drift of the particle and ω is the wave frequency.

To test for the presence of main and side-band resonances, the circular boundary equilibrium used in the above tests was used in conjunction with a single harmonic ($n = 3, m = 5$) of a TAE perturbation. The TAE had a frequency of $\omega = 2.7 \times 10^4$ rad/s and Fig. 4.12 shows the structure of this harmonic.

Particles were launched from a range of radii and with $\mu = 18$ eV/T and $\mathcal{E} - (\omega/n)P_\zeta = 3.661$ keV such that at the position of the primary resonance these particles had a total energy of $\mathcal{E}_{tot} = 3$ keV, and $\mathcal{E}_\perp = 50$ eV. The maximum variation of energy experienced by these particles is shown in Fig. 4.13. The energy variation due to the particle-wave interaction can be seen to increase strongly when close to a resonance and allows the radial locations of the resonances to be deduced. The q at resonance calculated using equation (4.2), and the average q, $\bar{q}$, seen by the resonant particles calculated using the HAGIS code, agree to within 0.8%.

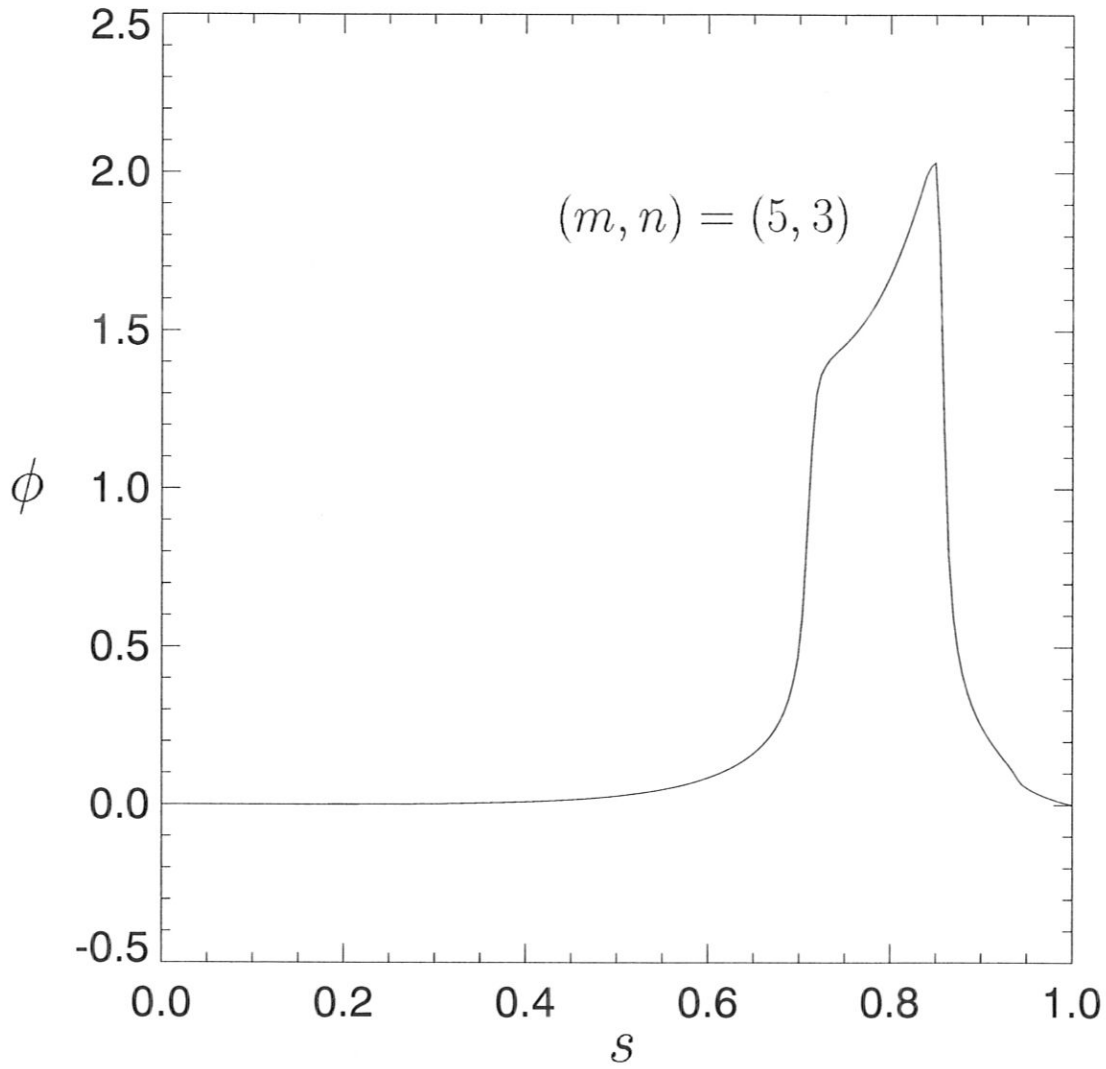

Figure 4.12: $m = 5, n = 3$ harmonic of a TAE perturbation for the aspect ratio 10 equilibrium.

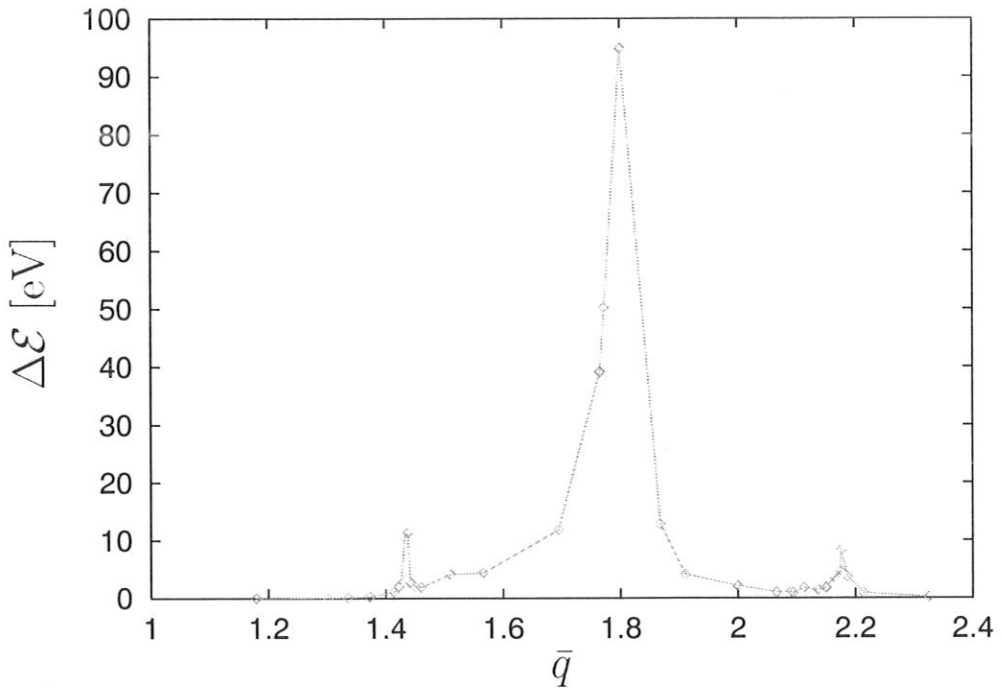

Figure 4.13: Variation of particle energy with average safety factor showing the location of the primary and side-band resonances.

4.1.5 System Convergence

For any simulation there are two primary factors that dictate how well converged the model's answer is. These are the number of simulation markers used n_p, and the integrator time step taken, h. It important to have a quantitative understanding of how the accuracy of any results is affected by these fundamental parameters, since there is a trade-off between accuracy and computational time required.

To demonstrate convergence, scans were made in n_p and h for a simulation demonstrating saturation of the $n = 5$, $m = 4, 5$ KTAE shown in Fig. 4.2 through its interaction with an isotropic centrally peaked slowing-down distribution of α-particles. The number of markers used was increased in factors of 2 from an initial 210, and the results presented in Fig. 4.14. For this scan h was held fixed such that the integrator made

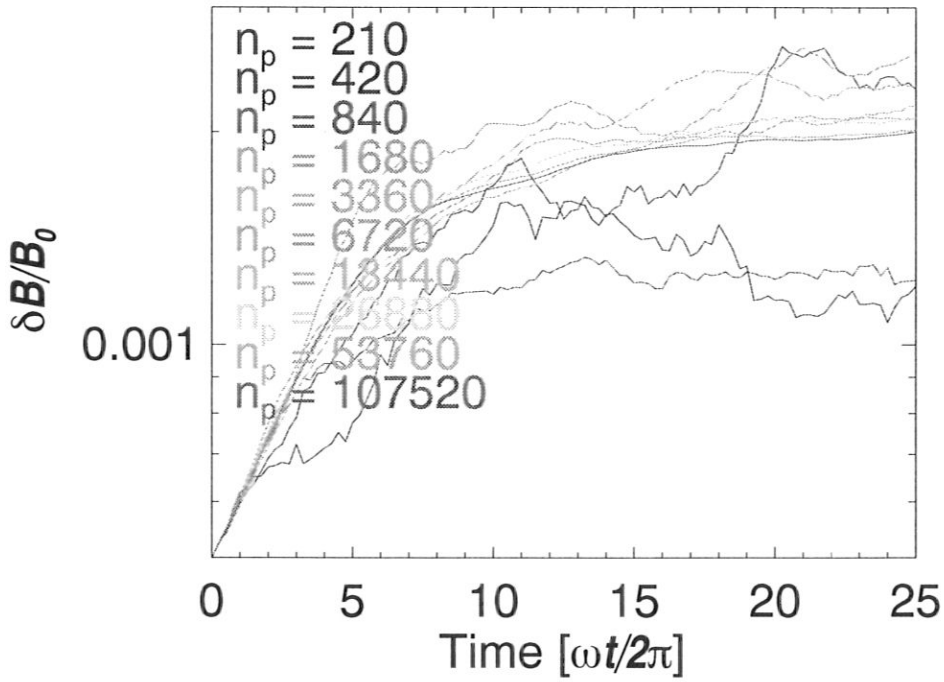

Figure 4.14: Convergence of wave evolution with respect to the number of simulation markers used n_p.

64 steps per wave period, $h = 2\pi/64\omega$. As is clearly seen, rapid convergence occurs to the linear growth phase of the evolution occurring before ~ 5 wave periods. The convergence to the saturated state takes slightly more particles to resolve, although this too is reasonably well converged with only $n_p = 6720$.

For this sequence of runs it is also possible to examine the conservation of the number of simulation markers, $n = n_0 + \delta n$. This information is summarized through an examination of the standard deviation of δn in Fig. 4.15. The plots show the oscillatory

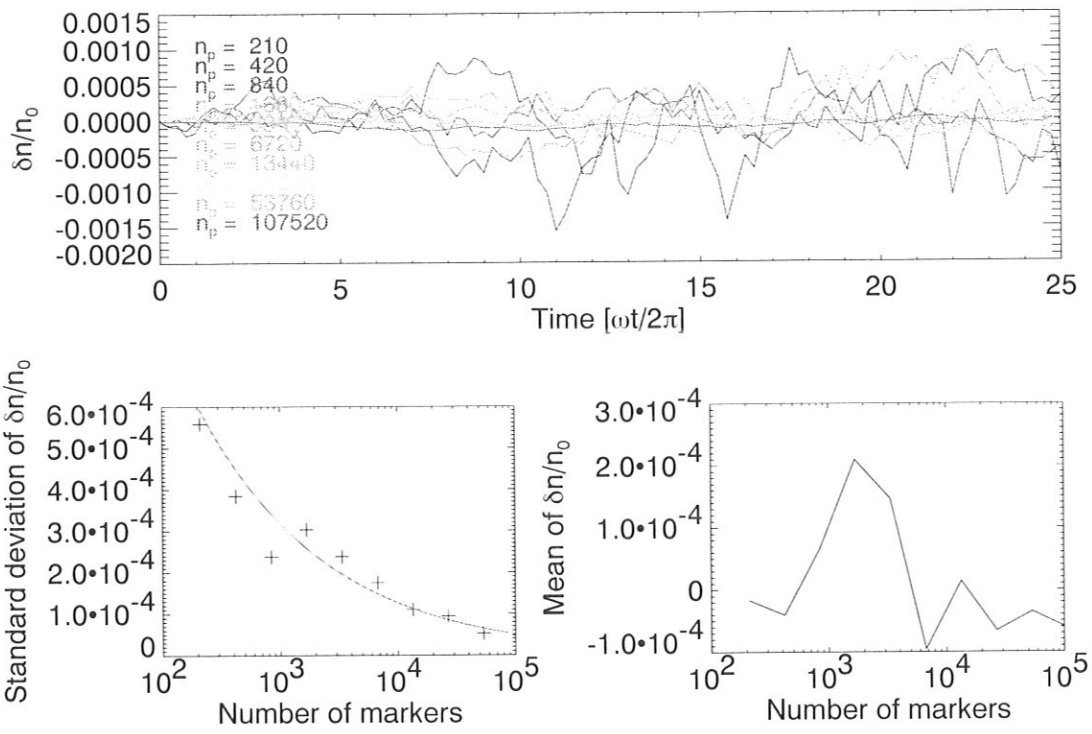

Figure 4.15: Plots showing the improvement in the conservation of particles with respect to the number of simulation markers used.

fluctuations in $\delta n/n_0$ around a mean value close to 0 for increasing particle number and the scaling of the standard deviation with respect to the number of simulation markers used, n_p. These latter data points are fitted using a least-squares procedure to a curve of the form a/n_p^b to give $a = 0.005$ and $b = 0.41$ indicating that the convergence is slightly slower than that for a random distribution of points for which it is expected that $b = 0.5$.

To examine the convergence with respect to the integrator time step used, h was decreased in factors of 2 down to a minimum such that the integrator was making 512 steps per wave period, $h = 2\pi/512\omega$. The results of this scan are presented in Fig 4.16. The plot shows that even for the largest integrator time step used[1] the wave evolution

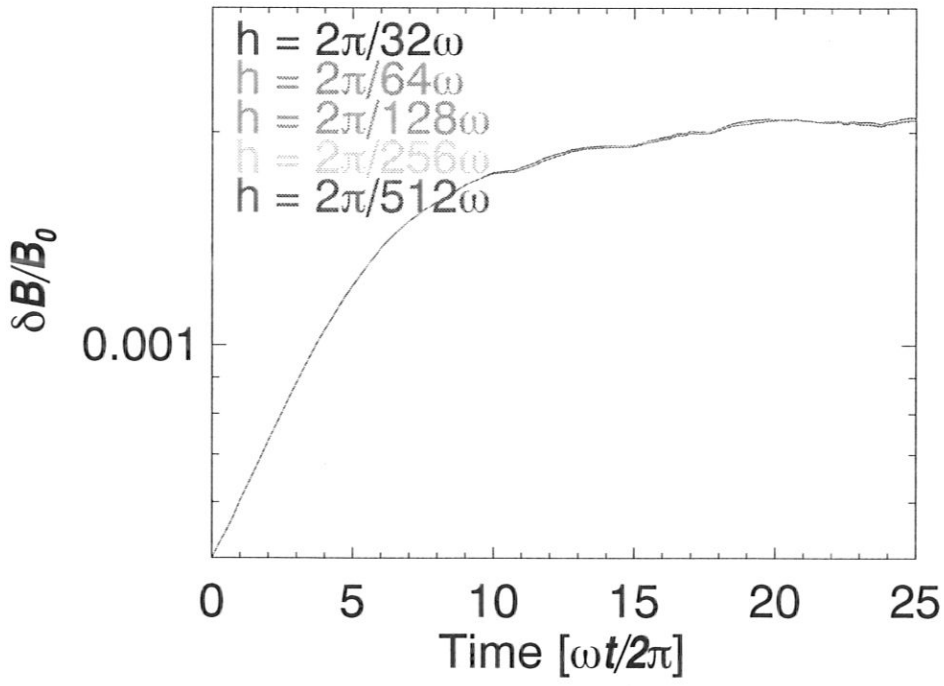

Figure 4.16: Convergence of wave evolution with respect to size of integrator time step h.

is already well converged.

[1]This particular simulation failed to run for $h \geq 2\pi/16\omega$.

4.1.6 Benchmarking

Due to the complexity of making analytic estimates of quantities associated with the interaction of fast particles with AE, comparisons with other codes are invaluable. They avoid the need to perform simulations within restrictive regimes such as at large aspect ratio ($\varepsilon \ll 1$) and often provide the only indicators of subtle coding errors. For these reasons the HAGIS code has been extensively benchmarked against many other codes including the FAC and CASTOR-K codes.

The FAC code [72] is a Monte-Carlo δf code independently developed in parallel with the HAGIS code. The CASTOR-K code [73] is a linearized δW code that uses unperturbed guiding centre orbits. Due to the completely different approach used by this code comparisons with it represent a particularly good test.

Beam-driven TAE

The parameters used for the first comparison are summarized in Table 4.4 and were

Parameter	Value
ε	0.1
R_0	8.011 m
B_0	10 – 50 T
q_0	1.25
n	5
m	7
ω	3.131×10^5 rads/s
f	49.83 kHz
${}^z_n A$	^{4}He
n_i	1×10^{20} m^{-3}
$\langle m_i \rangle$	2.0 m_H
$\langle \beta_f \rangle$	5×10^{-7}
n_p	60000
$\hat{\psi}_{pj}$	(0.02, 0.98)
$\mathcal{E}_j$	(10 keV, 3.8 MeV)
Δt	$2\pi/80\omega$

Table 4.4: Simulation parameters for beam-driven TAE

chosen such that the simulations fell into the category of small-orbit-width and large-aspect-ratio, allowing additional comparisons with analytical estimates.

The beam distribution used was

$$f_0 = C \exp(-2.5\hat{\psi}_p) \exp\left(-\frac{2\mathcal{E}}{\mathcal{E}_0}\right) \delta(\Lambda),$$

where $\Lambda = \mu B_0/\mathcal{E}$, $\mathcal{E}_0 = 3.52$ MeV and the field perturbation used consisted of a single $(m, n) = (7, 5)$ harmonic. The results of scanning in magnetic field intensity are shown in Fig. 4.17, where the dashed line represents the analytic prediction, whilst the points

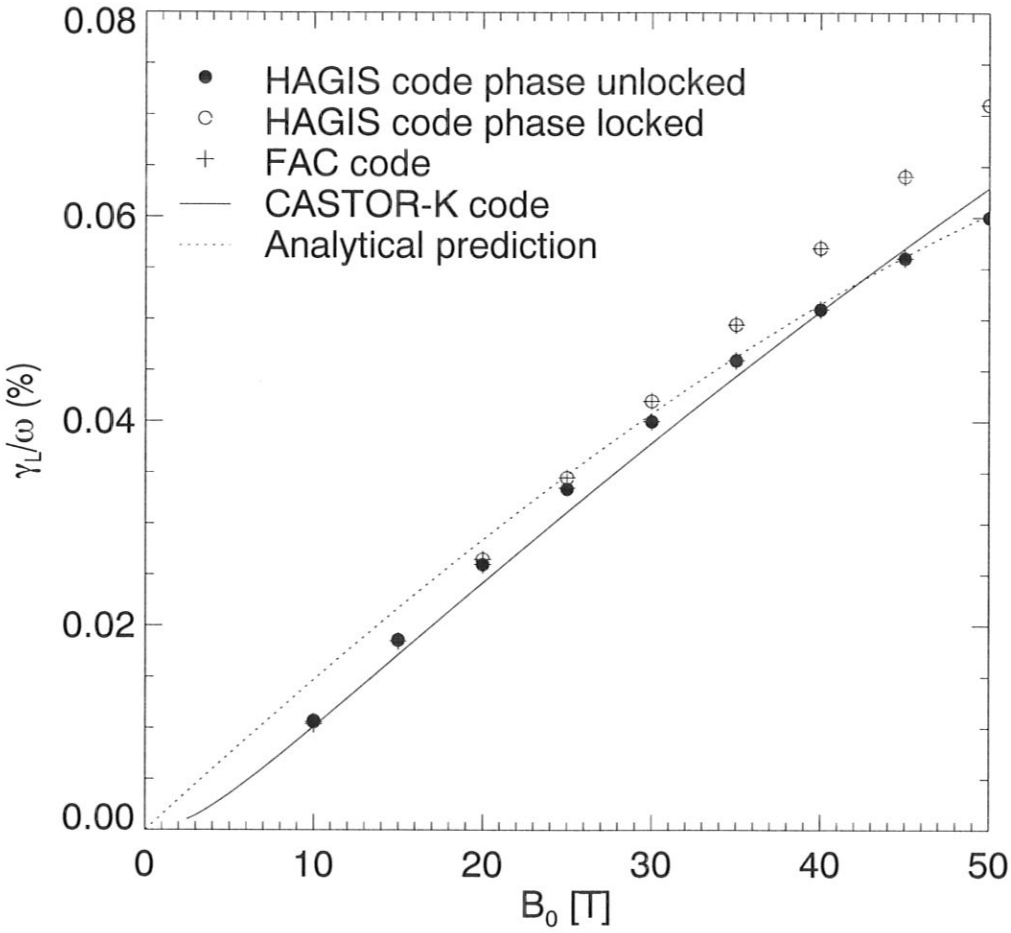

Figure 4.17: Variation of linear growth rate with magnetic field intensity.

represent simulations performed by the author using the HAGIS and FAC codes as indicated. The solid line represents results from the CASTOR-K code. The agreement is good, with small differences expected since the CASTOR-K code and the theoretical estimate assumed that the particles had zero orbit width (ZOW) whilst the full orbit width effects were retained within the HAGIS and FAC codes.

For the cases where the phase of the wave was unlocked and allowed to vary self-consistently in time, an additional comparison of the reactive frequency shift with time was possible between that HAGIS and FAC codes. This is presented in Fig. 4.18 where again good agreement is observed. This plot also suggests a mechanism for the

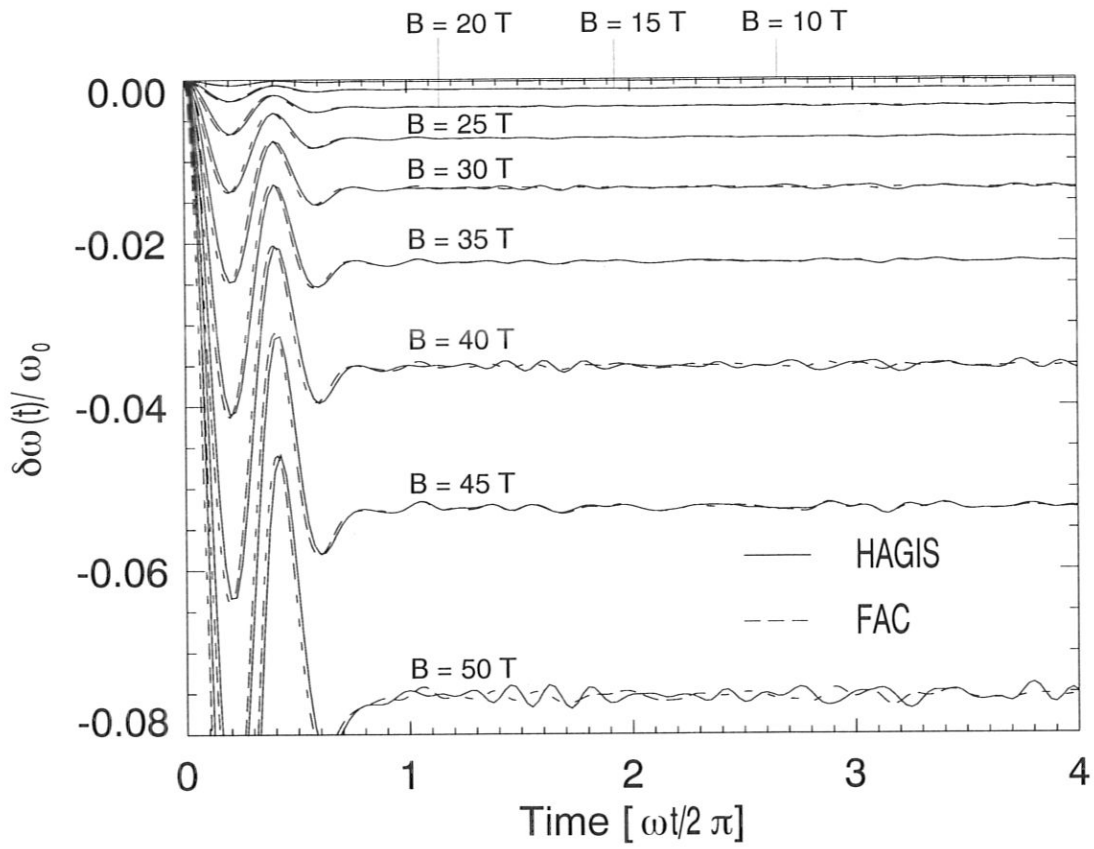

Figure 4.18: Comparison of frequency shift for various magnetic field intensities.

enhanced growth rate observed when the phase of the wave is allowed to vary self-consistently as compared to the locked phase case. As can be seen, the frequency shifts are always downwards to lower frequencies allowing lower energy particles to become resonant. Since there are more lower energy particles because of the use of a slowing-down energy distribution, an increased fast particle drive is obtained.

α-particle driven TAE in ITER-like plasma

The next case compared was that of an isotropic distribution of α-particles in an ITER-like plasma interacting with an AE. The simulation parameters for this test are summarize in Table 4.5.

Parameter	Value
ε	0.375
R_0	8.0 m
B_0	6.0 T
q_0	0.8375
n	10
m	8, 9
ω	$5.0 \times 10^5 - 8.0 \times 10^5$ rads/s
${}^z_n A$	^{4}He
n_i	1.1×10^{20} m^{-3}
$\langle m_i \rangle$	2.5 m_H
$\langle \beta_f \rangle$	5×10^{-4}
T_e	25 keV
T_i	23 keV
n_p	60000
Δt	$2\pi/80\omega$

Table 4.5: Simulation parameters for α-driven TAE in ITER-like plasma

The distribution of α-particle used was chosen to represent the expected distribution within an ignited tokamak. The energy distribution of this so called 'slowing-down' distribution is determined by the effects of electron and ion drag upon the α-particle population. Assuming that the D-T reactants share a common temperature T_i, and that the α-particles are produced with a roughly Gaussian energy distribution,

$$S(\mathcal{E}) = S_0 \exp\left[-\frac{(\mathcal{E} - \mathcal{E}_0)^2}{\Delta\mathcal{E}^2}\right],$$

the solution of the Fokker-Planck equation is [74],

$$f(\mathcal{E}) = \frac{1}{v^3 + v_c^3} \mathrm{Erf_c}\left[\frac{\mathcal{E} - \mathcal{E}_0}{\Delta\mathcal{E}}\right], \tag{4.3}$$

where the cross over velocity, v_c, is the speed below which the α-particles feel the effect of electron drag and is given by

$$v_c = \left(\frac{3\sqrt{\pi} m_e Z_1}{4 m_\alpha}\right)^{\frac{1}{3}} v_{te}, \qquad \text{where} \qquad Z_1 = \sum_i \frac{n_i Z_i^2 m_\alpha}{n_e m_i},$$

v_{te} is the electron thermal velocity and Z_i the charge on the ith species of ion.

The spatial distribution used takes the form of a Fermi distribution function with the parameters chosen to fit those expected in ITER,

$$f(\psi) = \frac{1}{\exp[(\psi - \psi_0)/\Delta\psi] + 1}.$$

ψ_0 is chosen to lie near the $q = 1$ surface since $m = 1$ MHD instabilities (sawteeth) are expected to flatten the distribution within this region [75]. Thus the final distribution used is,

$$f_0 = C \left(\frac{1}{\exp[(\psi - \psi_0)/\Delta\psi] + 1} \right) \frac{1}{\mathcal{E}^{\frac{3}{2}} + \mathcal{E}_c^{\frac{3}{2}}} \mathrm{Erf_c} \left[\frac{\mathcal{E} - \mathcal{E}_0}{\Delta\mathcal{E}} \right]$$

with $\psi_0 = 0.2$, $\Delta\psi = 1/14$, $\mathcal{E}_0 = 3.52$ MeV, $\mathcal{E}_c = 329.6$ keV, $\Delta\mathcal{E} = 335.2$ keV.

For this comparison a scan was made in the wave frequency whilst the phase of the wave was held fixed. The results for the three models are presented in Fig. 4.19 and as can be seen the agreement is again very good. The non-smoothness of the

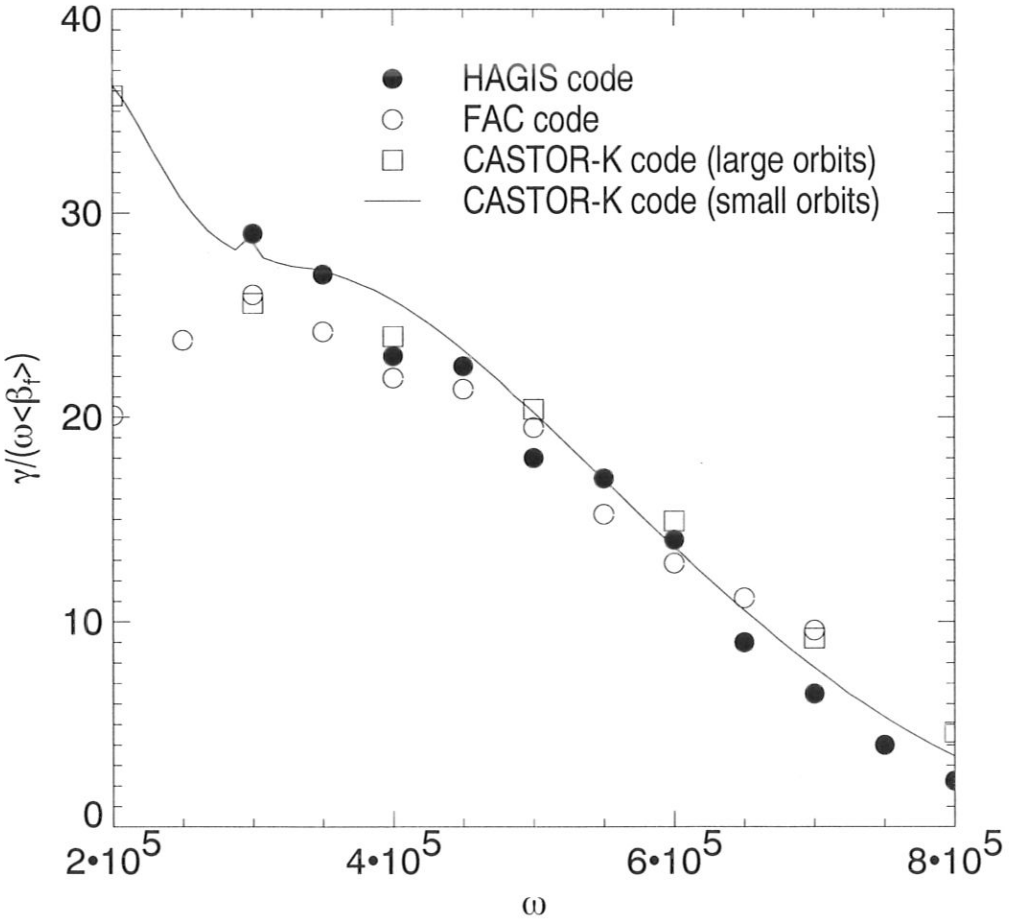

Figure 4.19: Comparison of growth rate variation with frequency.

curves is attributed to different classes of particles becoming resonant with different wave frequencies.

4.2 Summary

This chapter has outlined the computational implementation of the model developed in Chapter 3. The validity of the resulting code has been demonstrated through a series of tests that fall into two broad categories; those testing the numerical properties of the code and those testing the physical results the code produces. The first of these categories was satisfied by an examination of the code's convergence properties and the latter through a comparison with analytic results and other numerical work.

It has been shown that particles traverse the correct trajectories, and that system invariants scale correctly with parameters such as integrator step size and the number of markers employed.

There is a small overhead associated with the code's initialisation procedure but for realistic values the scaling of the run-time t with the number of markers used n_p, the number of AE present n_w, the number of integrator steps per wave period n_T and the simulation duration in wave periods T is approximately linear and given by the relation,

$$t \simeq c\, n_p n_w n_T T,$$

where the constant of proportionality $c \simeq 10^{-5}$ for an IBM RS6000 590 workstation. Hence for a run using 50,000 particles, two waves and running for 50 wave periods taking 64 steps per wave period, the run time is around 53 hrs of CPU time.

Chapter 5

Results

This chapter presents and discusses the results obtained by applying the HAGIS model to examine the interaction of a distribution of α-particles with discrete AE within the geometry of the JET tokamak.

5.1 Particle Prompt Loss Regions

In this first section the regions of phase-space where α-particles are unconfined even in the absence of a perturbative wave are considered. This information is important to avoid wastefully loading markers in those specific regions where they will be immediately lost during one poloidal transit period. These loss regions, known as prompt loss regions, generally depend upon the value of the toroidal current in the tokamak. In this chapter typical JET currents are considered in the range 1 – 3 MA. Losses due to the ripples in the toroidal magnetic field are not considered.

For a particle with known energy, its trajectory in real space is completely defined, up to the sign of $v_{\|}$, by the phase-space variables $\Lambda = \mu B_0/\mathcal{E}$, the normalized pitch angle, and P_ζ, the toroidal canonical momentum, which are constants of the motion in an axisymmetric equilibrium field. It is therefore convenient to examine the limiting case trajectories of 3.52 MeV α-particles in the (Λ, P_ζ) phase-plane. Fig. 5.1 shows the (Λ, P_ζ) phase-space topology of 3.5 MeV α-particles in JET, ($B = 2.87$ T, $I = 3$ MA). The curve AB in this diagram corresponds to the unconfined boundary for co-passing particle orbits. Those to the right of AB are confined, but become closer to intersecting the plasma edge as AB is approached.[1] The curve CD is the equivalent boundary for counter-passing particles, with the region to the left of the curve representing unconfined passing particles. BF represents the boundary between confined passing

[1]The terms 'co' and 'counter' are defined with respect to the plasma current which is directed into the paper for the diagrams illustrating Fig. 5.1.

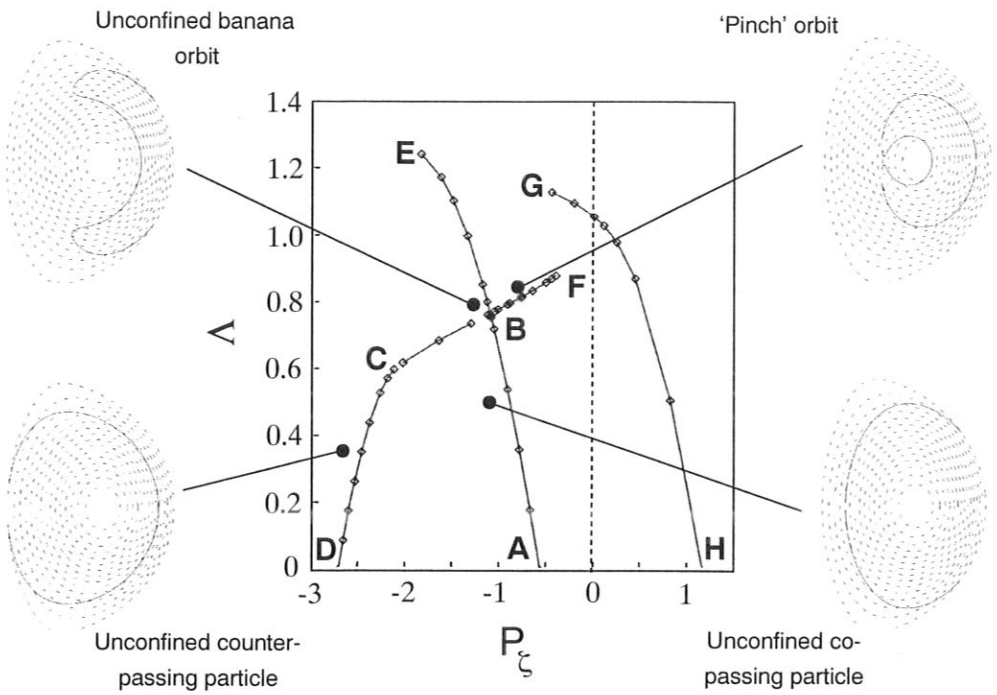

Figure 5.1: Boundaries between different orbit types for 3.5 MeV α-particles in JET.

particles and confined trapped particles (ie. banana orbits). The trapped particles becoming unconfined at the BE boundary. The curve BC is the phase-space boundary of counter-passing particles and trapped unconfined particles. Finally, the boundary depicted by GH represents co-passing stagnation points, these are positions where all the drift terms exactly cancel and the particle appears stationary in the poloidal plane while moving uniformly in the toroidal direction.

It is thus seen that in a JET equilibrium field, a co-passing particle is a prompt loss particle if it lies to the left of the phase-space boundary, ABE, and a counter-passing particle is a prompt loss particle if it lies in the phase-space region to the left of the curve EBCD.

The prompt loss markers that arise during a simulation form a localized zone just below the outer mid-plane of the tokamak. In the case shown in Fig. 5.2 all the markers have been loaded uniformly in s over the range $(0.0001, 0.8)$ and in energy over the range $(10\ \text{keV}, 3.8\ \text{MeV})$.

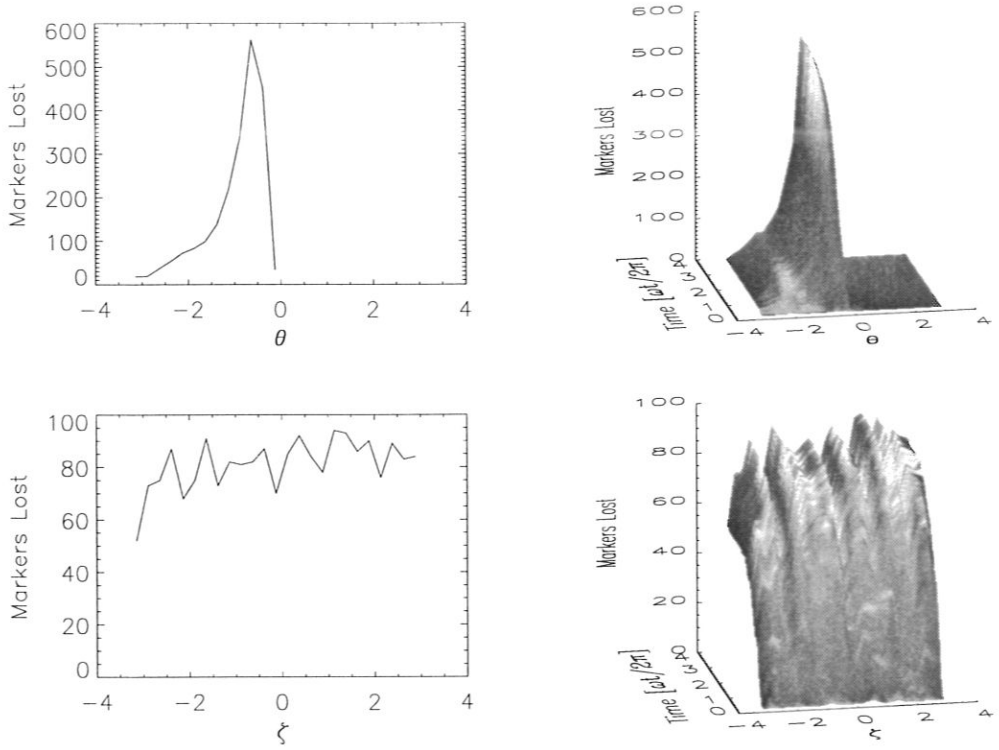

Figure 5.2: Distribution of lost markers as they pass through the last closed flux surface.

5.2 Enhancement of the Prompt Losses due to AE

The next step is to quantify the losses of α-particles near the prompt loss boundaries due to the effect of an AE upon them. The most sensitive region of the phase-space where AE can easily transform a confined particle into an unconfined one is the boundary between counter-passing confined particles and trapped-unconfined particles.

In the presence of an AE perturbation α-particles close to the prompt loss boundaries shown in Fig. 5.1 may lose toroidal angular momentum, or gain or lose energy, and cross over into the prompt loss region. The conversion of a counter-passing particle to a trapped unconfined particle through this process is illustrated in Fig. 5.3, where the

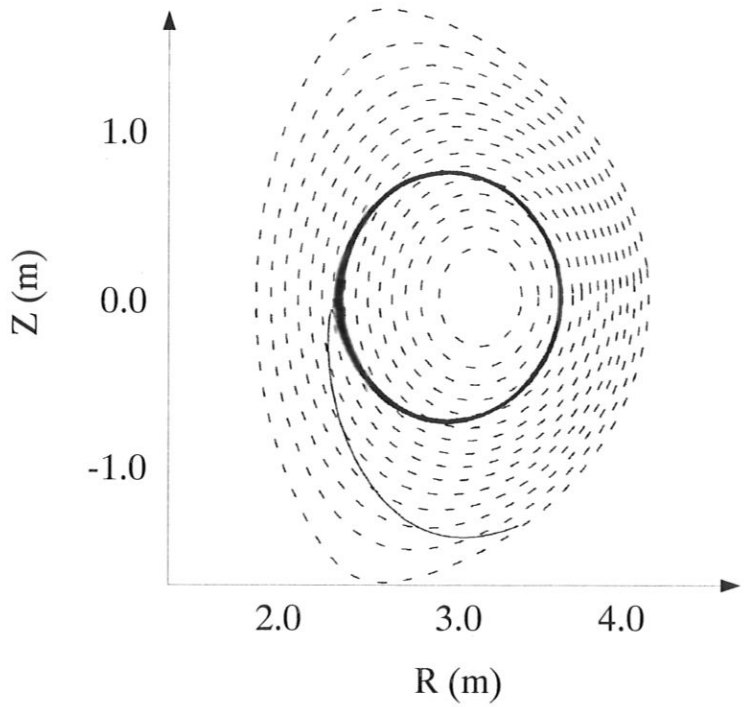

Figure 5.3: Conversion of counter passing particle to a trapped unconfined particle.

particle was launched close to the boundary BC in Fig. 5.1, with the launch location corresponding to a distance of 1cm from the prompt loss boundary in real space. The size of the perturbation was such that $\delta B^{\psi_P}/B = 3 \times 10^{-3}$ and the particle lost approximately 1% of its initial energy (3.5 MeV), and approximately 0.03% of its initial toroidal angular momentum, before passing through the last close flux surface.

Simulations with the HAGIS code [76] using a slowing down distribution in energy as described by equation (4.3), a radial distribution of the form,

$$f \sim (1 - \hat{\psi}_p)^3,$$

and a uniform distribution of α-particles in pitch angle, poloidal angle and toroidal angle indicate that in the presence of three $n = 3$ TAE an additional 1% of α-particles become prompt loss particles. Since these losses arise from the distortions of the flux surfaces due to the TAE modes, losses of this type scale as $\delta B/B$ in agreement with [55].

The regions of the phase-space where α-particles are promptly lost and the sensitivity of these boundaries with respect to the AE have therefore been established.

Note that in the case of toroidal field ripples, the prompt loss regions may become significantly larger and the AE effect upon the prompt loss boundaries may become much more pronounced. For the particular case of TFTR the AE induced ripple-like losses may be as high as 13% of the distribution [12], causing extensive damage to the first wall.

5.3 Resonant Particles and the Onset of Orbit Stochasticity

In this section the regions of the phase-space where α-particles experience the largest interaction with the AE are considered, in addition to the prompt loss regions discussed in §5.2. These regions of phase-space are governed by the resonance condition described by equation (2.14) and can be particularly complicated within realistic tokamak geometries with finite ellipticity and triangularity. If in addition the particle orbit requires higher Fourier harmonics for it's description due to the presence of a large amplitude AE perturbation, additional nonlinear resonances appear. To identify the resonance regions in arbitrary magnetic geometry and for finite amplitude perturbations it is therefore necessary to use a numerical approach to treat the resonance condition. One of the best ways to accomplish this is to analyse the wave to particle power transfer as a function of the initial particle conditions, amplitude and the structure of the wave. Performing a scan in initial α-particle energy and start location allows a figure to be constructed indicating those α-particles which interact most strongly.

As an example, one of the best performance deuterium pulses made in JET so far (shot #26087) is considered. An extensive study of TAE stability has been made for this case [77], and assuming that there is an equal mix of deuterium and tritium fuelling ions, it has been found that the $n = 3$ TAE modes are the most likely candidates for α-driven TAE instability. Accordingly, α-particle losses due to $n = 3$ TAE modes are focussed upon.

The equilibrium flux surfaces for this case (shot #26087) are shown in Fig. 5.4, whilst the $n = 3$ TAE eigenfunction harmonics corresponding to the $m = 3$ to 4

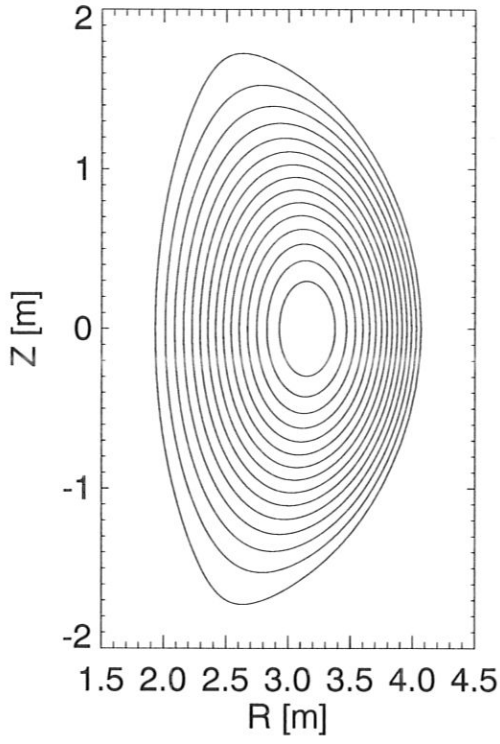

Figure 5.4: Flux surfaces for JET shot #26087.

gap and q-profile are shown in 5.5. As can be seen from the flux surface plot, the equilibrium JET configuration contains a certain amount of ellipticity and triangularity which may be expected to give rise to some additional coupling between non-adjacent poloidal harmonics. The inclusion of large amplitude TAE perturbations may also cause nonlinear resonances.

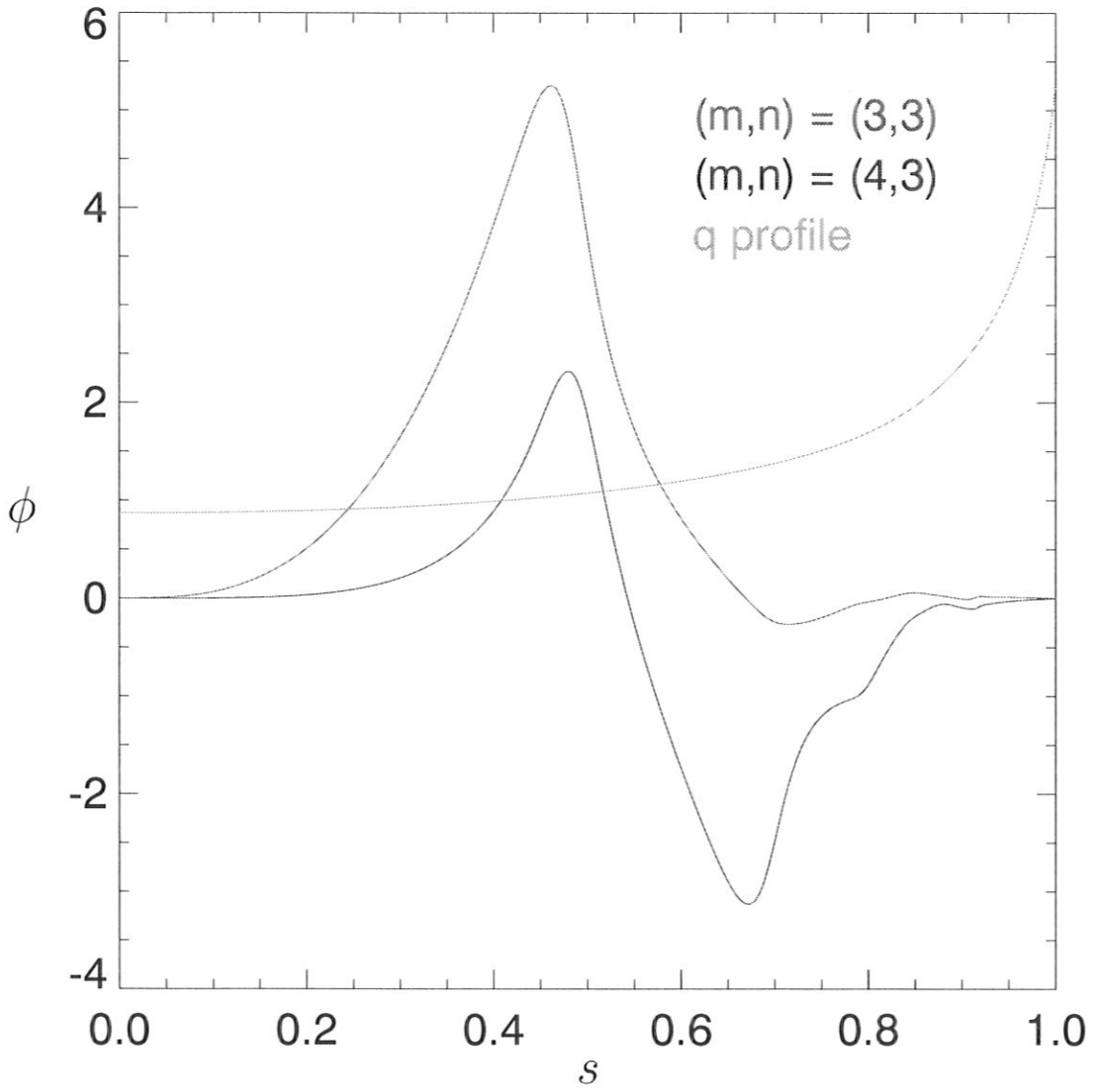

Figure 5.5: Harmonics of the perturbed scalar potential versus radius.

The variation in energy of deeply passing α-particles ($\lambda = 0$) that arises from their interaction with this TAE is shown in Fig. 5.6 where the wave amplitude was held fixed at $\delta B/B = 1.5 \times 10^{-3}$ whilst the initial launch radius was varied. The scan was performed for particles that were launched on the out-board mid-plane with the same initial energy, $\mathcal{E} = 2.2$ MeV, and shows the change in particle energy after 50 poloidal transits. The double peak of the primary resonance seen at $R = 3.52$ m occurs as the scan passes through the particle island which is formed as a result of the particle becoming trapped in the potential well of the $n = 3$ TAE. Examination of Fig. 5.6 shows that the number of resonances is larger than that obtained in a tokamak of

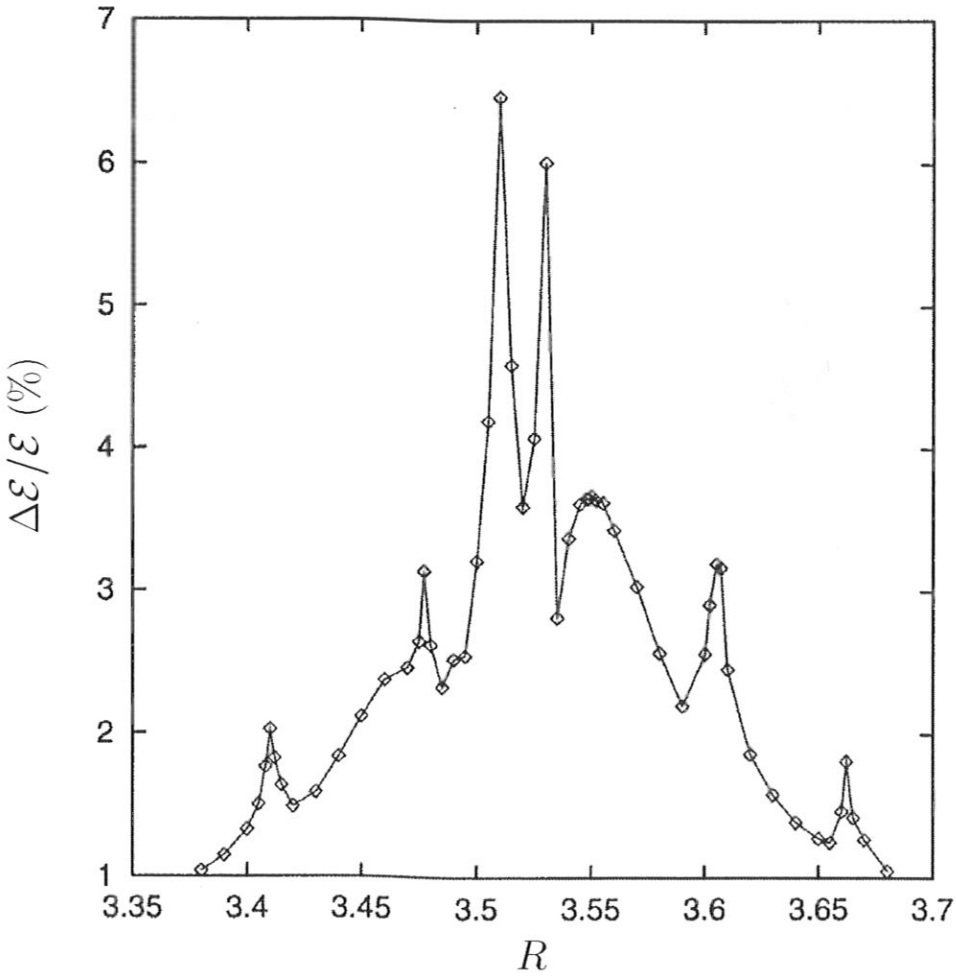

Figure 5.6: Fractional change in energy as a function of initial major radius for same case as Fig. 5.8 with $\delta B/B = 1.5 \times 10^{-3}$.

circular cross-section, where the $v_{\|} = v_A$ and $v_{\|} = v_A/3$ are the dominant resonances.

Additional side-band resonances are a result of the non-circularity and nonlinearity.

To analyse the structure of the resonances more thoroughly, a two dimensional scan has been performed in initial particle energy and launch radius for the case of a JET $n = 5$ AE of amplitude $\delta B/B = 10^{-4}$. The particles considered were deeply passing ($\lambda = 1$) α-particles that were launched up to a maximum energy of $\mathcal{E} = 1.5$ MeV, between $R = 3.1$ m and 3.6 m. Each of the particles were followed for 50 poloidal transits with the change of energy represented in terms of the intensity used in Fig. 5.7. The complex structure of the resonances (even for deeply passing particles with $\lambda = 1$)

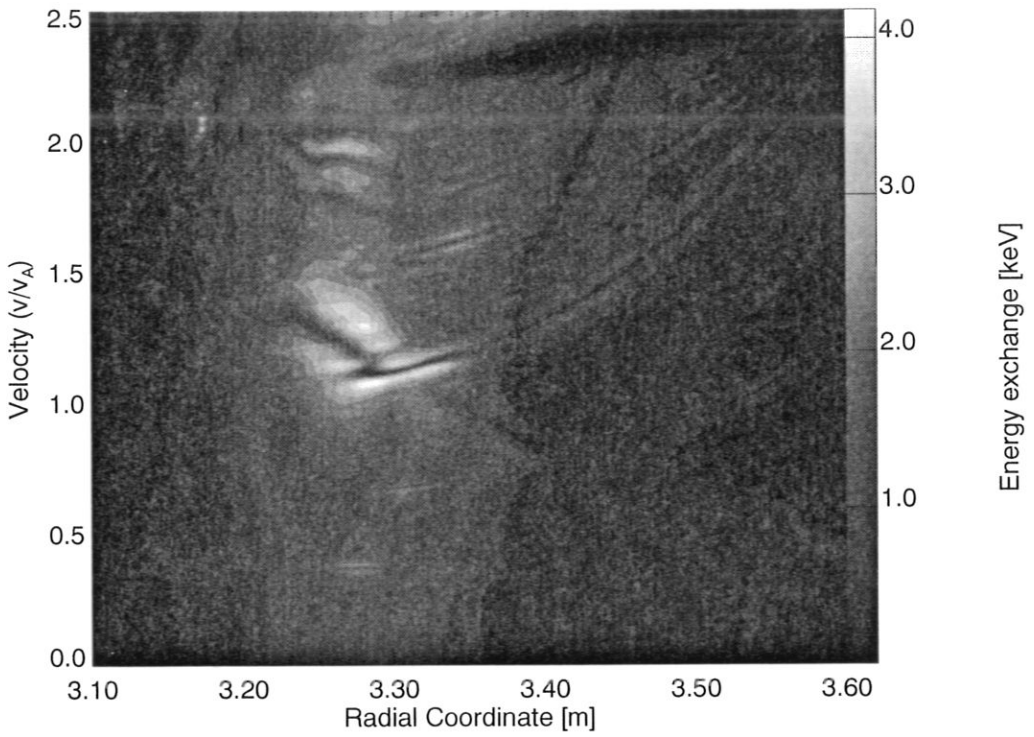

Figure 5.7: Wave-particle energy exchange between deeply passing α-particles and an $n = 5$, $p = 0$ KTAE. The primary resonance corresponding to particles moving at the Alfvén velocity ($E \simeq 1$ MeV) is clearly seen and is radially located near the peak in the eigenfunction. The $v_A/3$ sideband resonance is also discernable.

necessitates an accurate representation for the fast particle distribution, especially with respect to energy, since it is seen that there will still be a relatively strong exchange of wave-particle energy near the cut-off energy to which particles are loaded.

Particles that are close to the resonance regions of the phase-space become trapped in the potential well of the AE and the orbits of these particles form island structures.

As a particle's energy increases, so its orbit increasingly deviates from a flux surface, and Fourier analysing the magnetic field in the frame of reference of the particle one finds a main harmonic and side-band harmonics. Stochasticity arises when the particle islands, caused by the primary and side-band harmonics, overlap; this process differs from magnetic island stochasticity, in that a single harmonic can give rise to stochastic orbit motions. For deeply passing particles the location of the particle islands are determined from the resonance condition given by equation (4.2). The primary resonance is $l = 0$, and the side-bands $l = \pm 1$, etc. For a given TAE frequency, ω, the locations of the particle islands are determined by the q-values which are resonant (ie. satisfy equation (4.2)). Since for a TAE the eigenfunction harmonics peak at the gap, $q = (2m+1)/2n$ for the m to $m+1$ gap mode, the largest particle islands are obtained for resonance at the gap q-value.

It can be demonstrated that above a certain threshold amplitude of the AE perturbation, particle orbits first become stochastic at the separatrix of the island, before the stochasticity region increases to occupy a significant fraction of the plasma radius. In terms of the resonances shown in Fig. 5.7 the onset of stochasticity corresponds to the broadening of the resonance regions in the phase-space up to a coalescence of the neighbouring resonances. If the stochasticity region is much smaller than the radius of the plasma the stochasticity has a local character so that just an enhanced radial re-distribution of the particle orbits results. However, in the case of large amplitude AE, or in the case of multiple AE, the stochasticity regions can spread out across the whole plasma radius, so that the stochasticity takes a global character and particle losses follow.

As an example, we consider the JET case (#26087) described above. Fig. 5.8 shows the particle islands for a sequence of increasing amplitudes of a single TAE perturbation. These plots show the particle orbit intersections with the $\theta = 0$ plane. To ensure that a single particle class was followed the invariants $\mathcal{E} - (\omega/n)P_\zeta$ and μ were held constant for all the α-particles at $10^7\,\mathrm{eV}$ and $10^3\,\mathrm{eV/T}$, respectively. At $R = 3.67\,\mathrm{m}$ this gives $\mathcal{E}_{tot} = 2.2\,\mathrm{MeV}$ and $\mathcal{E}_\perp = 2.2\,\mathrm{keV}$ (ie a deeply passing particle). This particular energy for the α-particle was chosen in order to locate the primary resonance near the $m = 3$ to 4 gap location for the computed TAE frequency of $\omega = 9.77 \times 10^6\,\mathrm{rad/s}$. It can be seen that stochasticity occurs for a relatively large value of $\delta B/B \simeq 5 \times 10^{-3}$ at the gap. This large value is partly a consequence of the low magnetic shear in the gap region, since the required field for overlap is inversely proportional to the magnetic shear [78]. Consideration of a realistic spectrum of unstable TAE modes, as opposed to the single mode considered here, is expected to lower this stochasticity threshold by at least one, and probably two, orders of magnitude. The amplitudes quoted in the plots correspond to the maximum values of the perturbed radial field, $A = \delta B^{\psi_p}/B_0$.

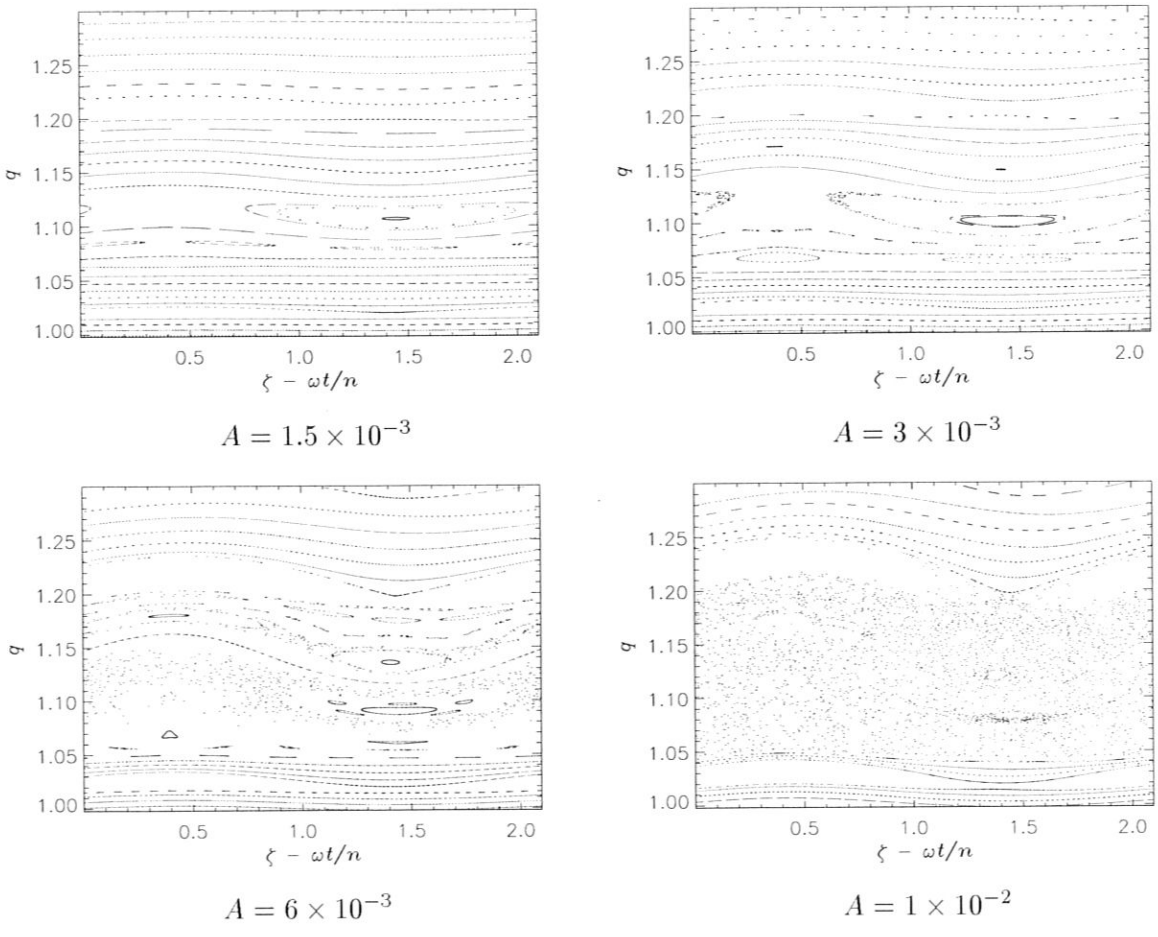

Figure 5.8: Particle islands in the $\theta = 0$ plane plotted versus the phase $(\zeta - \omega t/n)$ arising from an $n = 3$ TAE for various amplitudes.

5.4 Nonlinear Saturation of a Single α-Particle Driven KTAE

In the previous sections of this chapter the effects of finite fixed amplitude AE upon α-particles have been considered and in particular it was observed that particle stochasticity appears in the system above some threshold. To establish whether this threshold can be achieved due to the free energy source associated with the radial gradient of the α-particles, a self-consistent nonlinear treatment is needed. This section is devoted to the analysis of a KTAE interacting with a distribution of α-particles in JET. Mode damping due to the bulk plasma is neglected in this treatment, as are particle sources and sinks. Hence the case considered is an idealised scenario producing an approximate upper limit for the AE growth rate and saturation amplitude.

The simulations presented in this section address the nonlinear AE evolution by directly simulating the wave evolution and particle re-distribution arising from the interaction of a single $n = 5$ KTAE and the expected distribution of α-particles within a D-T JET plasma. The parameters used for this simulation are summarized in Table 5.1.

Parameter	Value
ε	0.334
R_0	3.0 m
B_0	3.0 T
q_0	0.87
n	5
m	4, 5
f	191.7 kHz
${}^{z}_{n}A$	^{4}He
n_i	4.8×10^{19} m^{-3}
$\langle m_i \rangle$	2.5 m_H
$\langle \beta_f \rangle$	2.5×10^{-3}
n_p	75000
Δt	$2\pi/64\omega$

Table 5.1: Simulation parameters for α-particle driven $n = 5$ KTAE in JET.

The distribution function was chosen to represent an isotropic slowing down distribution of α-particles,

$$f_0 = C\left(1 - \hat{\psi}_p\right)^3 \frac{1}{\mathcal{E}^{\frac{3}{2}} + \mathcal{E}_c^{\frac{3}{2}}} \mathrm{Erf_c}\left[\frac{\mathcal{E} - \mathcal{E}_0}{\Delta\mathcal{E}}\right]$$

where $\mathcal{E}_0 = 3.52$ MeV, $\mathcal{E}_c = 329.6$ keV and $\Delta\mathcal{E} = 335.2$ keV, and is shown in Fig. 5.9.

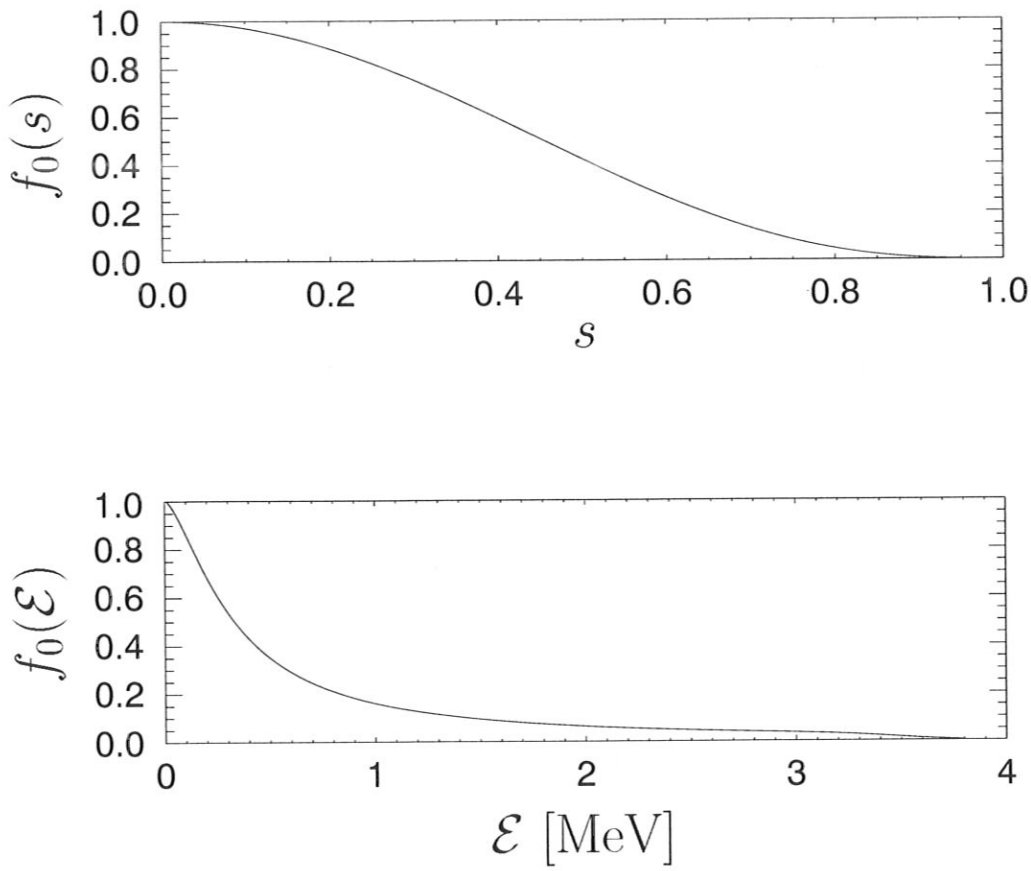

Figure 5.9: Slowing down distribution of α-particles.

The $n = 5$, $m = 4, 5$ eigenfunctions used for these simulations are shown in Fig. 5.10 along with the q-profile and the radial distribution of fast particles.

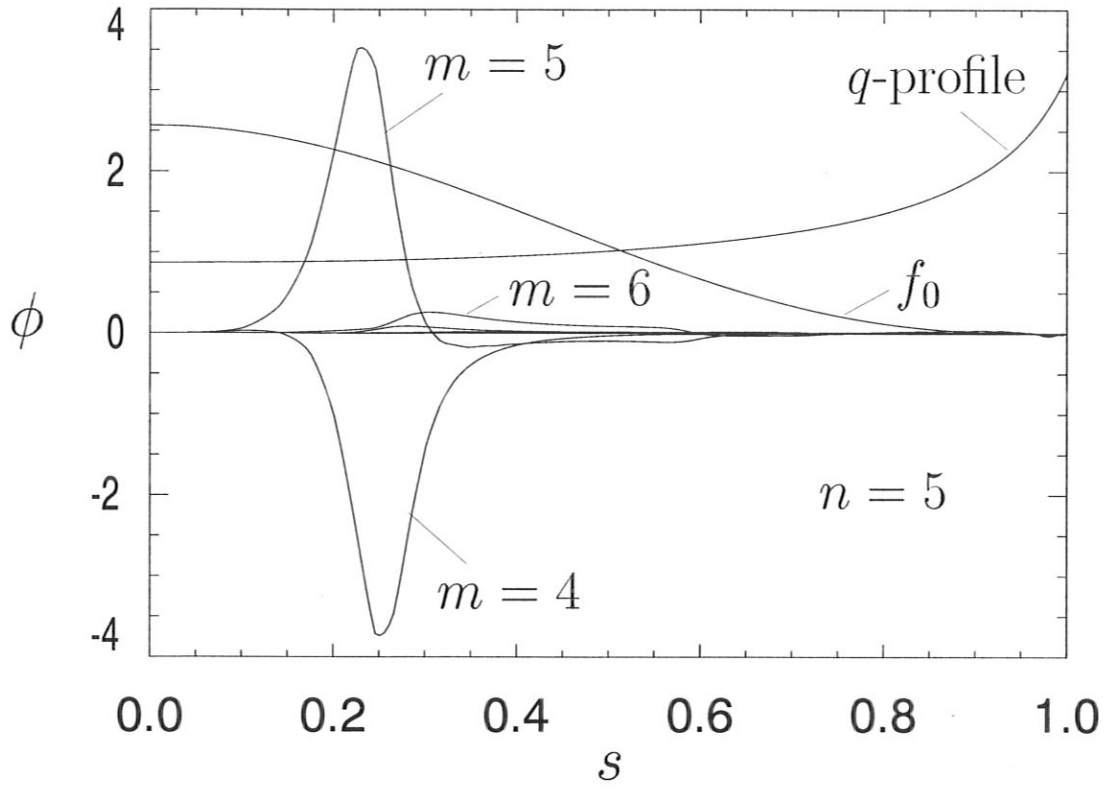

Figure 5.10: Plot showing the radial structure of the principle poloidal harmonics of the $n = 5$ KTAE together with the q-profile and the radial distribution of fast particles.

The evolution of the KTAE that resulted from it's interaction with this population of α-particles is shown in Fig. 5.11 depicting the AE amplitude and growth rate as

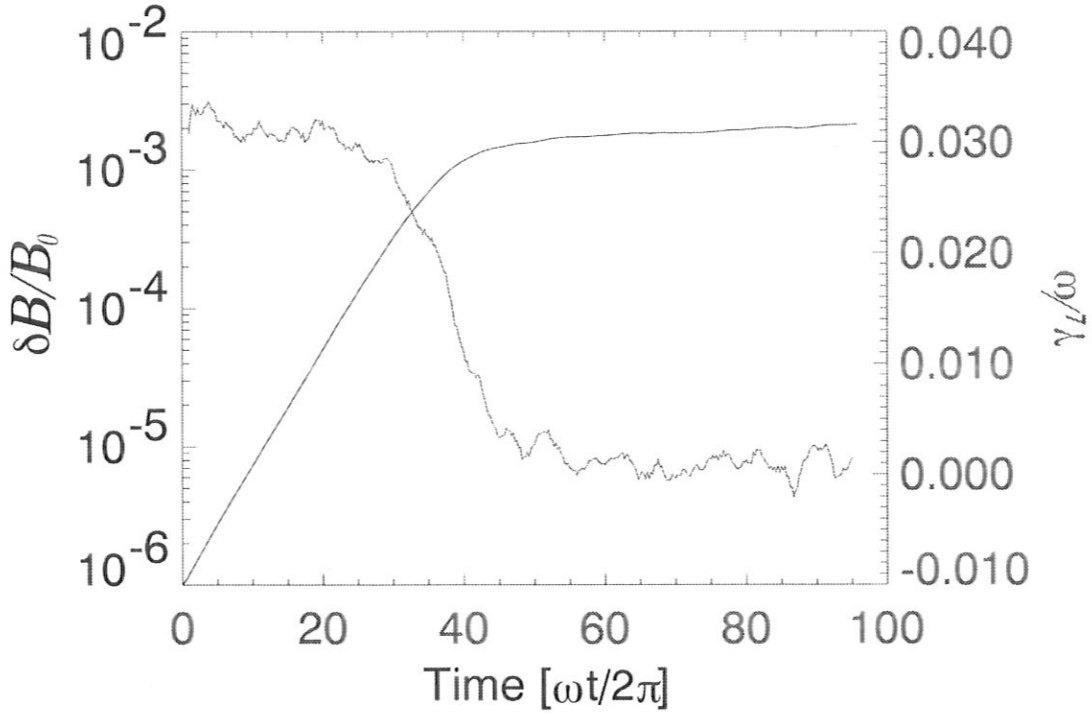

Figure 5.11: Evolution of an $n = 5$ KTAE in JET interacting with a slowing down distribution of α-particles.

a function of time. The diagram clearly indicates the two generic stages of the wave evolution that arise in simulations of this type. The first stage is the linear growth stage during which the wave amplitude increases exponentially with time. This behaviour may be understood by observing from equations (3.31) and (3.34) that for infinitesimally small δf,

$$\left.\begin{array}{l} \dot{A} \propto \delta f \\ \delta f \propto A \end{array}\right\} \dot{A} \propto A \Rightarrow A = A_0\, e^{\gamma t}.$$

The second stage in the wave evolution is a saturated state which may be understood by observing that the radial profile of α-particles has been significantly modified such that it no longer acts as a source of free energy, as in Fig. 5.12. The classes of particles

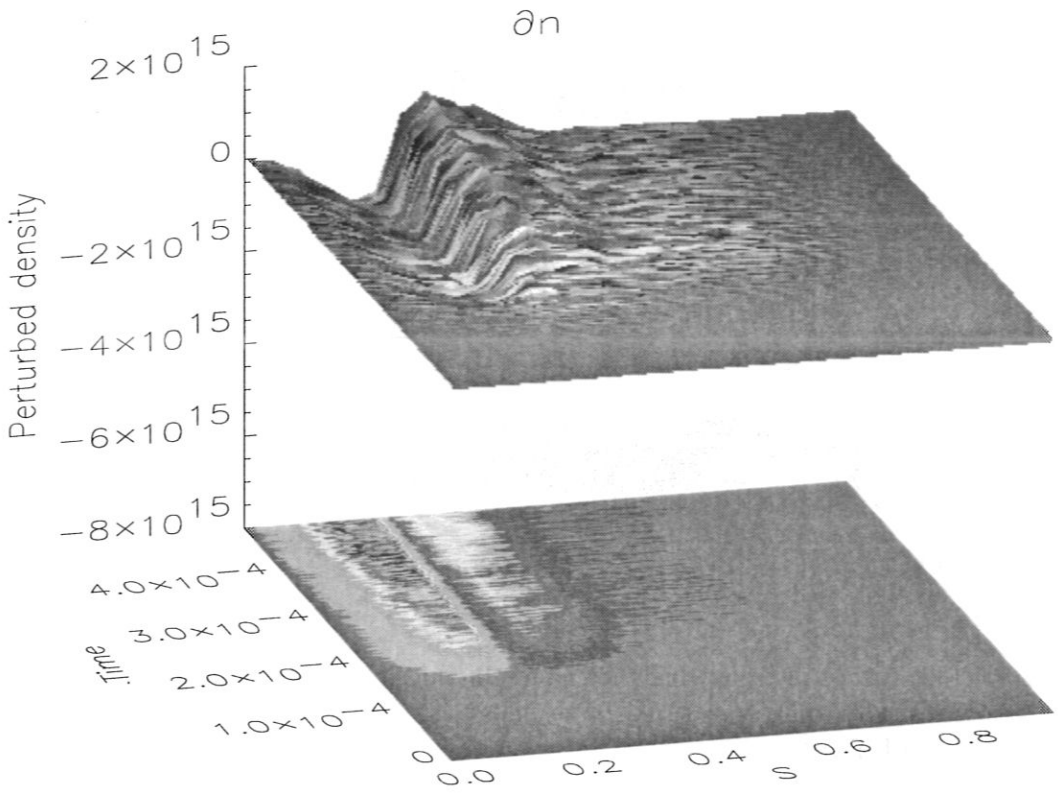

Figure 5.12: Plot showing the radial redistribution of α-particles by an $n = 5$ KTAE in JET with time (measured in seconds). The surface plot facilitates an intuitive understanding of the change in the fast particle density (particles/m^3), whilst the contour plot (depicting the same information) provides a clear overview of the regions affected.

which have interacted with the wave are revealed in the plot of the α-particle density fluctuations against particle energy, as in Fig. 5.13. In this plot the passing particle resonances, as well as the additional resonances due to the trapped particles resonating through their precession and bounce frequencies can be seen at $\mathcal{E} \simeq 150$ keV, $\mathcal{E} \simeq 750$ keV, and $\mathcal{E} \simeq 1.8$ MeV. The particle conservation for this simulation is presented in Fig. 5.14 showing the exceptional conservation of particles during the early linear stage and the characteristic oscillatory behaviour following the onset of saturation.

It can be seen from Fig. 5.11 that the saturated amplitude of the wave is related to

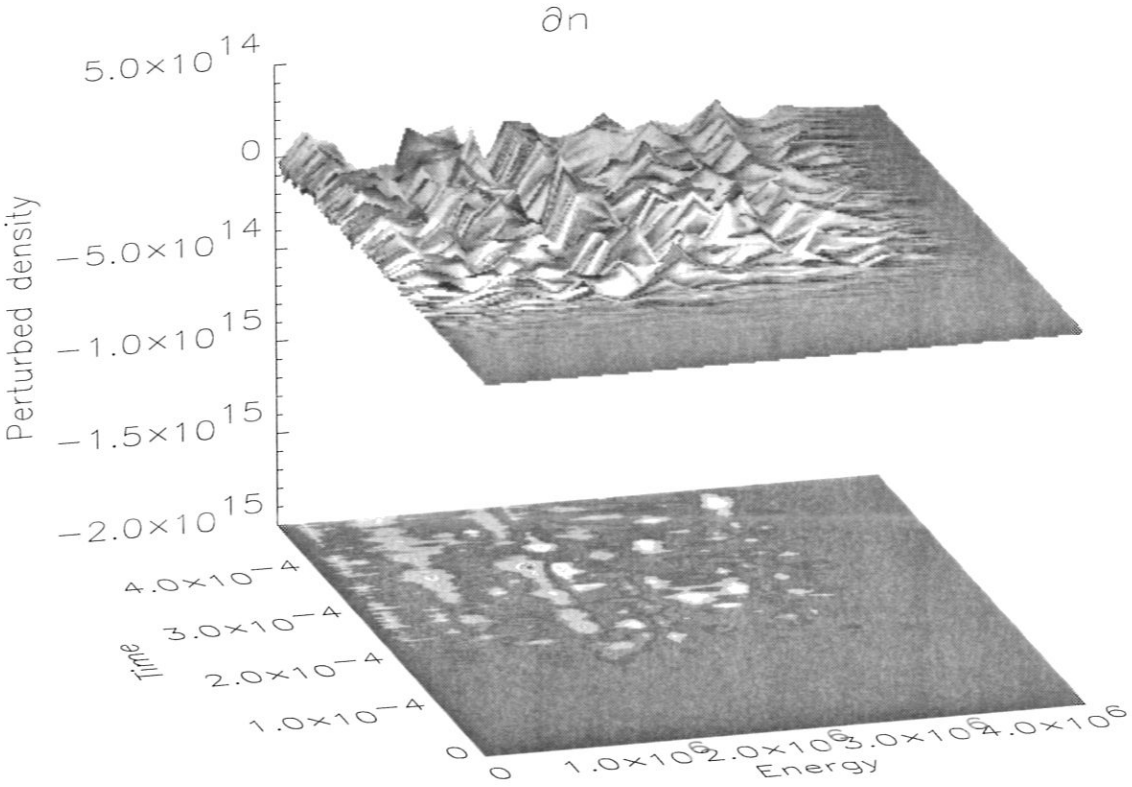

Figure 5.13: Surface plot showing the change in the slowing down energy distribution of α-particles with time (measured in seconds) that has arisen from the interaction with an $n = 5$ KTAE in JET. The contour plot (whilst showing the same data) allows the resonances to be clearly seen. The density change in this plot is measured in particles/m^3.

the linear growth rate through,

$$\frac{\delta B}{B} \simeq C \left(\frac{\gamma}{\omega}\right)^2, \quad \text{where} \quad C \approx 1.38, \tag{5.1}$$

which is in reasonable agreement with [41] and [42].

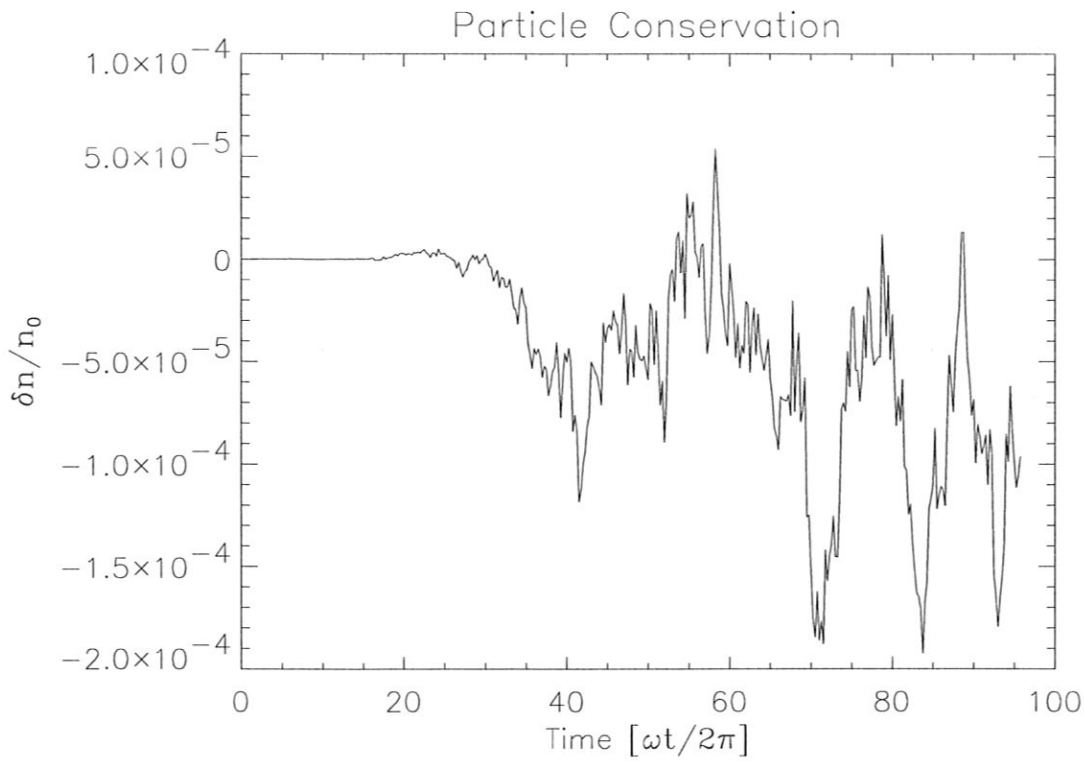

Figure 5.14: Conservation of α-particles interacting with $n = 5$ KTAE in JET.

The scalings of linear growth rate with volume averaged α-particle beta $\langle\beta_f\rangle$, is presented for this case in Fig. 5.15. As can be seen from this plot, the variation is approximately linear over this range of $\langle\beta_f\rangle$, with only a small departure when the phase of the wave is allowed to vary.

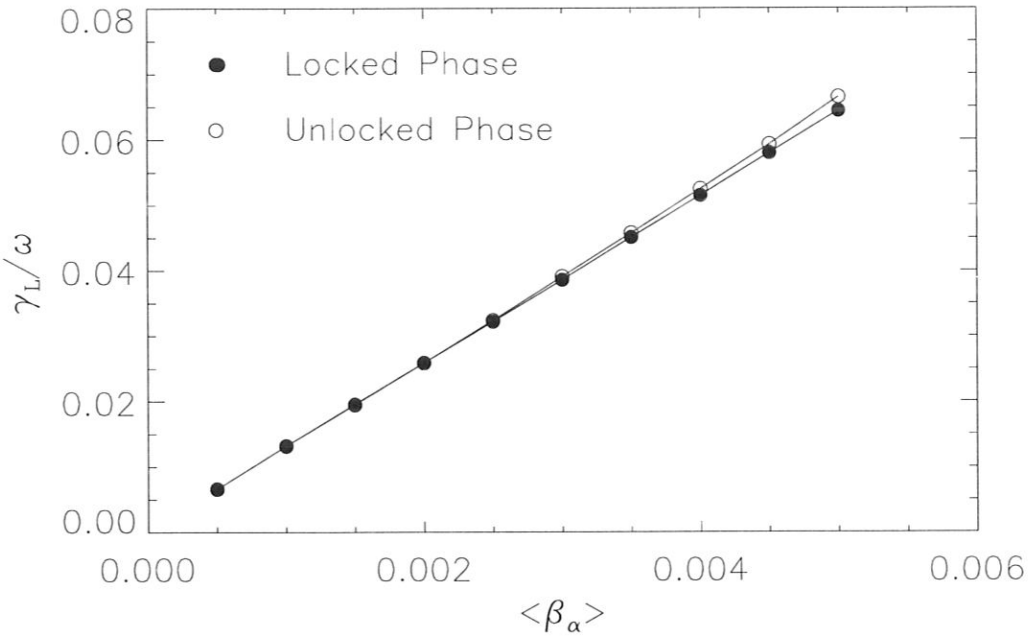

Figure 5.15: Variation of growth rate with respect to $\langle\beta_f\rangle$ for an $n = 5$ KTAE in JET driven by an isotropic slowing-down distribution of α-particles.

The variation of frequency shift with growth rate is shown in Fig. 5.16 where an approximately linear downward shift in frequency is found with increasing growth rate.

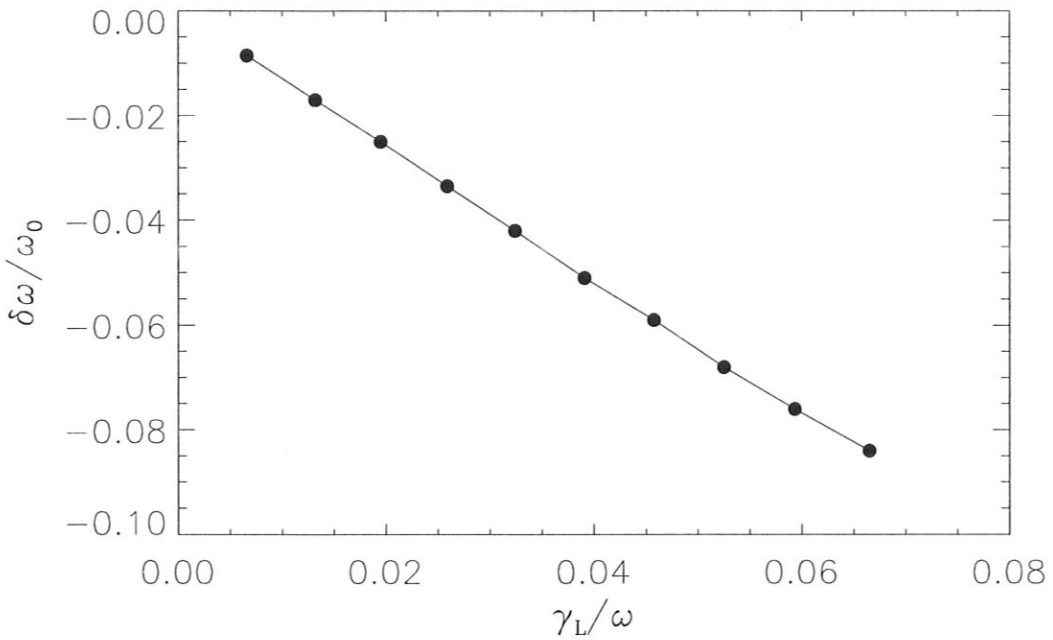

Figure 5.16: Variation of reactive frequency shift with growth rate for an $n = 5$ KTAE in JET driven by an isotropic slowing-down distribution of α-particles.

It is interesting to note that the case presented has a growth rate of $\sim 3\%$ and saturates by itself at $\delta B/B = 2 \times 10^{-3}$, in quantitative agreement with the results found in [42, see Fig. 11], where an analogous treatment of the wave-particle problem was performed without wave damping, particle sources or sinks.

5.5 Self-Consistent Evolution of α-Particles and Multiple KTAE

In the case of a system containing multiple KTAE the self-consistent dynamics of both the waves and particles can be very different from those described in the previous section.

In the first instance, even waves which are stable with respect to the initial distribution of α-particles may become unstable as a result of the particle re-distribution due to neighbouring waves. This secondary instability known as the 'domino effect' was considered in detail in [79, 80].

Secondly, for the case of several unstable waves of comparable wave energy, a nonlinear saturated phase may be significantly obscured, since the formation of a plateau on the distribution function which saturates the growth rate of one wave will not necessarily saturate the neighbouring wave as well.

Thirdly, as a result of several waves coupling through the energetic particle population every individual wave can be enhanced significantly by the other waves present and can reach higher amplitudes than it can alone. The strength of the wave coupling through the energetic particle population may be expected to depend upon the ratio of the growth rate and the eigenfrequency separation for different waves.

In this section a discrete spectrum of KTAE ($n = 5 - 9$) is simultaneously evolved with a slowing-down distribution of α-particles. The results of these simulations are then compared with those for each of the AE singly to identify the key features arising from the presence of multiple AE.

Due to the orthogonality of the KTAE eigenfunctions with different toroidal mode numbers n, the wave energy of the bunch of KTAE is a simple sum of the individual wave energies without any cross-terms. This fact allows an individual treatment of amplitude and phase variations for each KTAE to be used.

5.5.1 Non-Interacting and Interacting Waves

A realistic slowing-down distribution of α-particles which is centrally peaked is used, described by same form as used for the previous simulations in §5.4. Using this distribution, simulations have been performed showing the evolution of a spectrum of KTAE in JET. By running simulations with each of the modes separately as well as with the complete set at once, it is possible to examine the effect of the waves interacting with each other through the fast particles. The eigenfunctions generated for these simulations are shown in Fig. 5.17 together with the radial α-particle distribution and q-profile. Table 5.2 summarizes the eigenfrequencies for each of the waves and indicates the principle poloidal harmonics required for their description.

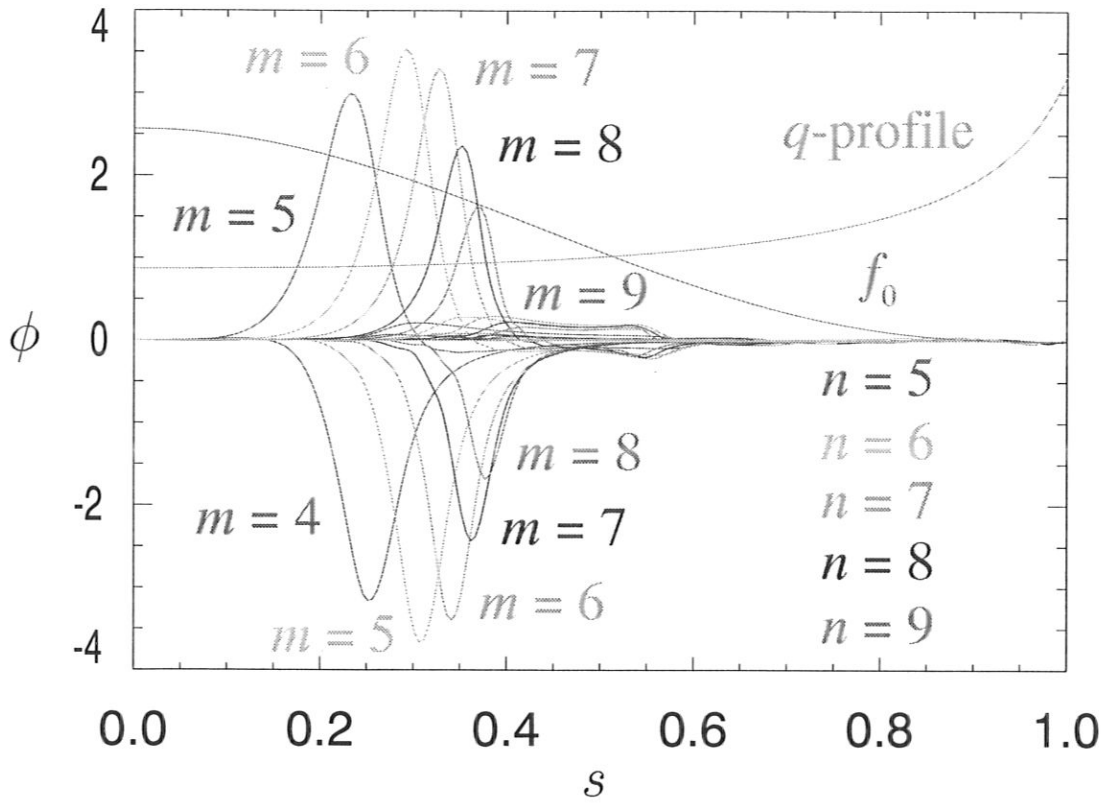

Figure 5.17: Eigenfunctions corresponding to $n = 5 - 9$ KTAE in JET. The relative sizes are accounted for through the normalization requirement that $(\delta B^{\psi_P}/B_0)_{\max} = 1$ for all modes with unit amplitude. Also shown in this plot is the radial distribution of fast particles and the q-profile.

Toroidal mode number, n	**Eigenfrequency,** f **[kHz]**	**Principle poloidal harmonics,** m
5	191.7	4, 5
6	195.4	5, 6
7	198.3	6, 7
8	200.9	7, 8
9	203.2	8, 9

Table 5.2: Parameters for each of the KTAE used.

The results of performing simulations with each of the eigenmodes separately is shown in Fig. 5.18. As can be see from this plot, each individual eigenmode has a clear

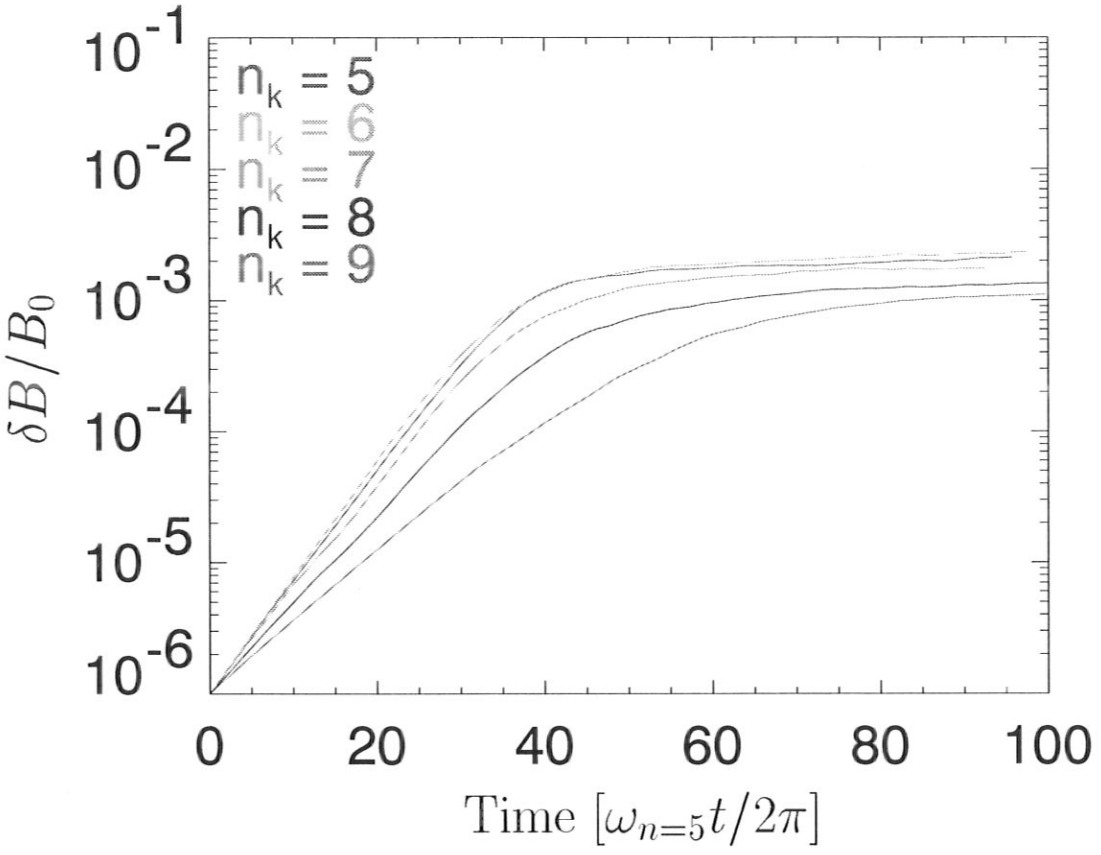

Figure 5.18: Evolution of each single (non-interacting) $n = 5 - 9$ KTAE in JET.

saturation at around $\delta B/B_0 \sim \mathcal{O}(10^{-3})$. Due to the comparable wave energies and regions of wave localisation for all the KTAE running individually, the condition given by equation (5.1) is fulfilled as expected. At such high wave amplitudes, the nonlinear interaction of multiple KTAE coupled together through the α-particles may no longer be negligibly small. As a result of the nonlinear coupling, Fig. 5.19 clearly shows that every KTAE can reach either a much smaller 'quasi-saturated' amplitude, or a much higher amplitude, than achieved alone.

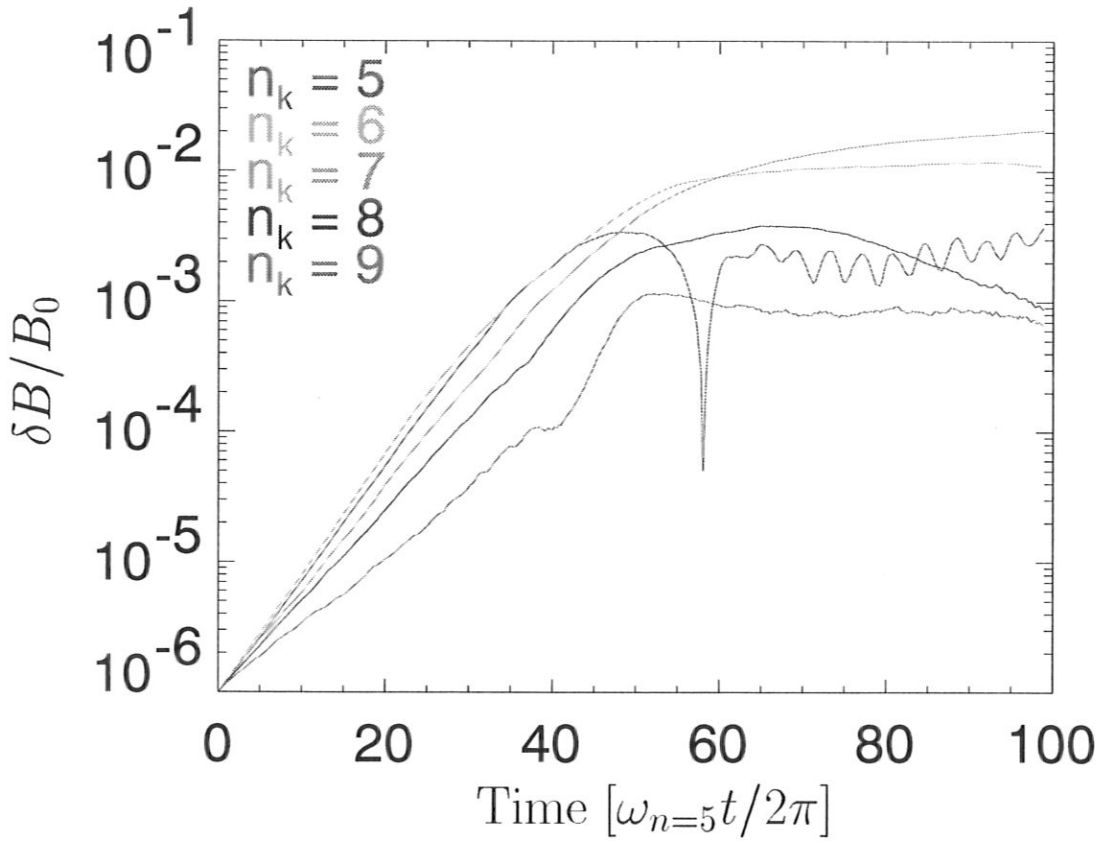

Figure 5.19: Evolution of $n = 5 - 9$ KTAE in JET interacting through a slowing-down distribution of α-particles.

The particle re-distribution that arises from the collective effect of these KTAE is shown in Fig. 5.20. As can be seen from a comparison with Fig. 5.12, α-particle re-

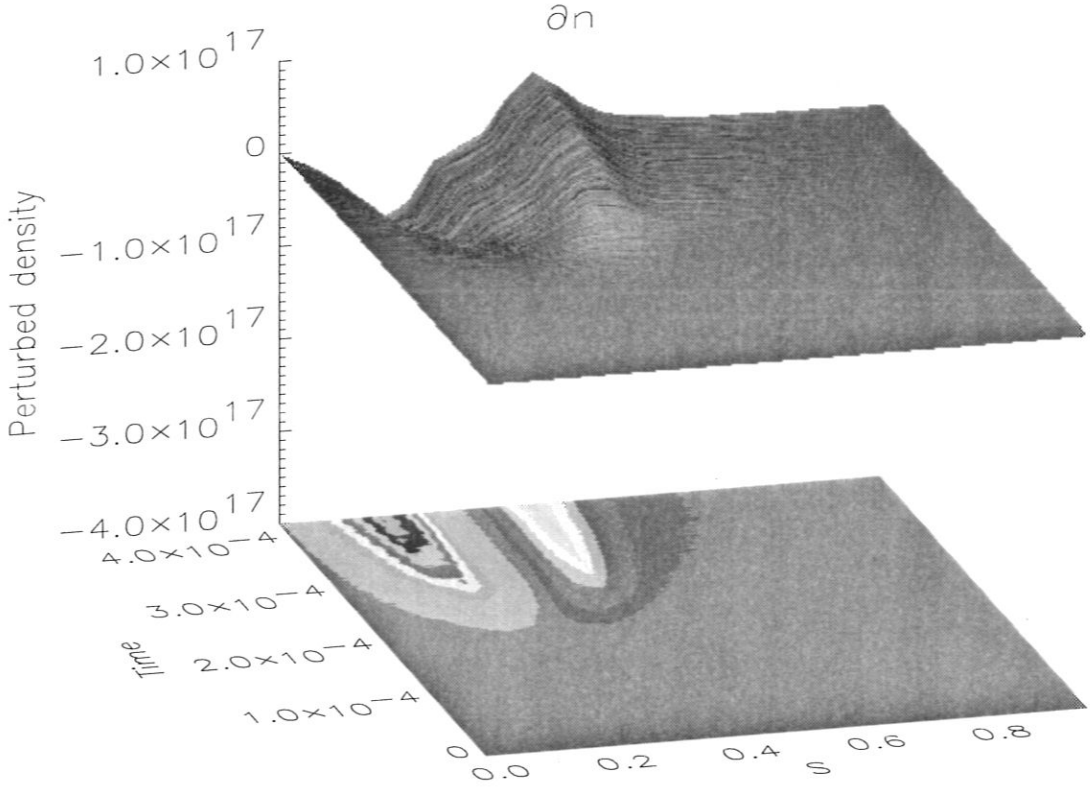

Figure 5.20: Plot showing the radial redistribution of α-particles caused by the collective effect of $n = 5 - 9$ KTAE in JET with time (measured in seconds). The surface plot facilitates an intuitive understanding of the change in the fast particle density (particles/m^3), whilst the contour plot (depicting the same information) provides a clear overview of the regions affected.

distribution has occurred over a much larger area and to a far greater extent than for that obtained through the interaction with a single eigenmode. An examination of the perturbed energy distribution shown in Fig. 5.21 indicates that the loss of energy from the α-particles to the waves has occurred across the whole of energy distribution.

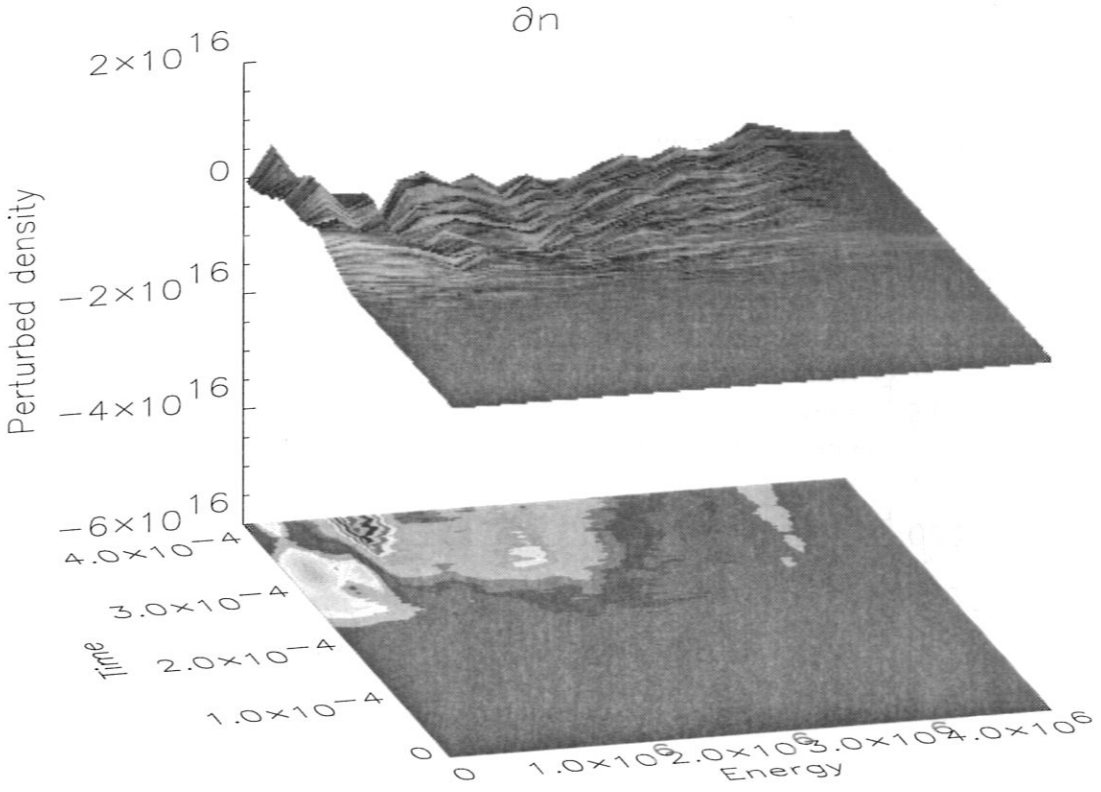

Figure 5.21: Plots showing the change in the slowing down energy distribution of α-particles with time (measured in seconds) that has arisen from the interaction with $n = 5 - 9$ KTAE in JET. The contour plot (whilst showing the same data) shows the extensive region over which particle energy has been transfered to the waves. The density change in this plot is measured in particles/m^3.

The conservation of particles for this simulation is presented in Fig. 5.22 where following the linear evolution regime, a linear degradation of particle conservation is observed.

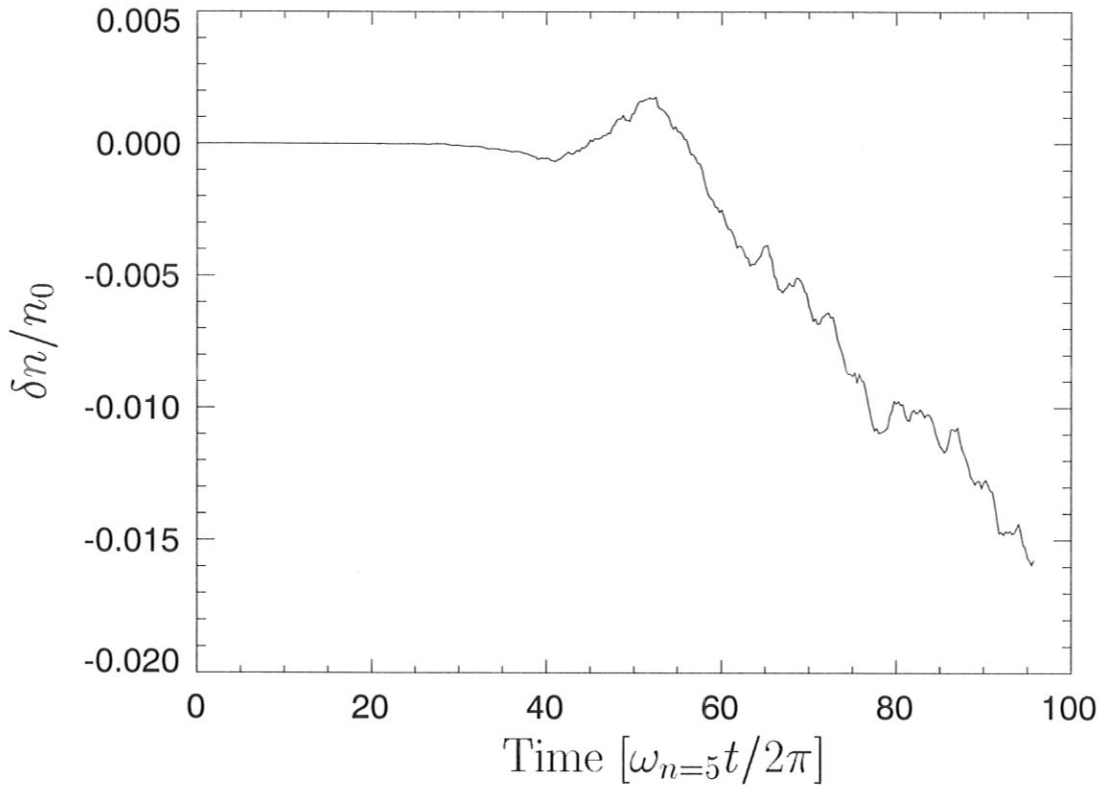

Figure 5.22: Conservation of α-particles interacting with $n = 5 - 9$ KTAE in JET.

At the higher amplitudes achieved in this simulation, the approximations made in the model may be violated. In particular, MHD nonlinearities may become important [81, 82, 83]. To overcome this possible violation of the model's approximations, future work may address the problem of multiple large amplitude AE coupled through the fast particles in two ways. Firstly, additional damping effects can be included into the model leading to far lower wave amplitudes, and secondly, the underlying physical model may be adapted to accommodate the wave-wave nonlinearities.

5.6 Summary

In this chapter the regions of phase-space corresponding to prompt-loss α-particles from a JET plasma have been identified and the effect of the presence of a TAE upon them quantified.

The effect of an AE upon the particle motion and the stochastic threshold for JET shot #26087 is obtained. The complex range of resonant α-particles for an $n = 5$ KTAE in JET has been quantified in terms of their initial conditions.

The self-consistent evolution of a single Kinetic TAE and the α-particle population in JET plasmas has been modelled in the absence of KTAE damping, sources and sinks of α-particles. The α-particle re-distribution that arises from the wave-particle interaction has been presented.

The self-consistent evolution of several unstable Kinetic TAE and the α-particles in JET plasmas have been modelled in the absence of KTAE damping, sinks and sources of alpha-particles. A much broader region of the α-particle phase-space is involved in the nonlinear evolution in the case of multiple KTAE, and a more extensive radial redistribution of alpha-particles is observed in this case. Due to the fact that all of the KTAE are coupled through the same α-particle population, some new nonlinear phenomena have been found in the case of multiple KTAE. In particular, due to the effective energy redistribution between different KTAE some of the KTAE can reach significantly higher amplitudes, whilst others are suppressed. Further development of the code is however needed in this case, as the wave amplitudes may exceed the approximations made in the current model.

Chapter 6

Summary and Conclusions

6.1 Summary

In this thesis the problem of weakly damped AE driven by populations of fast particles within tokamak plasmas as outlined in Chapter 1, has been addressed. This generally nonlinear problem has been approached by constructing a self-consistent model, the HAGIS code, that combines a perturbative wave approach with a Hamiltonian guiding centre treatment of the fast particles, as described in Chapter 3. The radial structure of each eigenmode has been assumed to remain invariant throughout the simulations, with each wave evolving through changes in its amplitude and phase. The variations in wave amplitude and phase are described by the same wave Lagrangian that describes the radial eigen-structure of the waves through the inclusion of higher order perturbing terms. The complete self-consistent model is formulated within a δf framework, enabling simulations to be performed with far lower noise levels than has previously been possible with conventional codes.

During the development of the HAGIS model it has been applied to study many different aspects of the wave-particle interaction. The first of these was an examination of the topology of different energetic particle orbits, and the establishment of the prompt loss regions of the particle phase-space. This was possible once the guiding centre trajectories of energetic particles in the presence of a discrete spectrum of Alfvén waves in arbitrary toroidally symmetric geometry had been developed, implemented and validated.

Two possible α-particle loss mechanisms arising from AE, and previously identified by [55], have been confirmed and quantified for a single TAE in JET. The first mechanism is due to the TAE-induced broadening of the prompt loss boundary and was found to scale as $\delta B/B$, whilst the second mechanism, due to the TAE-induced stochasticity of the particle orbits, scaled as $(\delta B/B_0)^2$. Both of these scalings are in agreement with [55]. However, the stochasticity threshold for this case (JET discharge

#26087) was found to be higher than in [55] due to the smaller magnetic shear in JET.

The structure of the wave-particle resonances has been analysed for the case of a single AE and passing α-particles in JET geometry. The model describes resonances arising from the non-circularity of the plasma cross-section and from perturbations of the particle orbits due to the finite amplitude of the AE (nonlinear resonances).

The onset of particle orbit stochasticity in the presence of fixed finite amplitude AE has been numerically studied using the HAGIS code and explained in terms of the wave-particle resonance overlap.

Further development of the HAGIS code towards a self-consistent wave-particle model has been made. Keeping the spatial structure of the AE fixed, the time evolution of the amplitude and phase of each AE present is described by a set of differential equations.

To overcome numerical noise in the self-consistent model, the δf formalism was implemented into the HAGIS code. The complete model was then validated through a comparison of conservation laws and analytical results, as well as through direct comparisons with other codes.

This model has been used to describe the self-consistent evolution of the Kinetic TAE and the expected distribution of α-particles in JET plasmas in the absence of KTAE-damping mechanisms and α-particles sources and sinks. The correct nonlinear behaviour of the coupled KTAE and the α-particles has been found in these runs; the saturated amplitude of the α-driven KTAE has been quantified as an upper estimate of the single KTAE instability. The α-particles were found to be radially re-distributed within a region close to the central region where the KTAE is localised.

The self-consistent evolution of several unstable Kinetic TAE and the expected distribution of α-particles in JET plasmas has been modelled in the absence of KTAE-damping mechanisms and sources or sinks of α-particles. A broader region of the α-particle phase-space was found to be involved in the nonlinear evolution in this case, and a more extensive radial redistribution of the α-particles was found. It was found that due to the energy redistribution between different KTAE coupled through the α-particle population, some of the KTAE reached significantly higher amplitudes, whilst others were suppressed.

6.2 Conclusions

The principle conclusion of this thesis is the demonstration that in the absence of any wave damping mechanisms, a single AE driven by a slowing-down distribution of α-particles can reach an amplitude as high as $\delta B/B \geq 10^{-3}$ for $\langle \beta_f \rangle = 2.5 \times 10^{-3}$. In systems with more than one AE present, even higher amplitudes are found to be achievable leading to an enhanced radial redistribution of α-particles. Whilst for these

simulations, wave damping mechanisms have been neglected, qualitatively the same plateau formation upon the radial α-particle distribution at lower wave amplitudes is expected within simulations in which wave damping is included.

In all of the cases considered the nonlinear redistribution of α-particles was in a relatively small central region close to where the AE eigenfunction was localised. Consequently, no significant α-particle losses to the first wall were found. However, the central redistribution of α-particles may be expected to cause a change in the heating profile which has important consequences for sustaining an ignited tokamak plasma. Indeed, the modification that this would cause to the current profile may be such as to drive current driven tearing modes leading to an enhanced radial transport of particles and an increased risk of disruption.

6.3 Further Work

Future work will be focussed upon the further development of the model, its application, and an analysis aimed at quantifying the effects of the redistribution of the fast particles upon the heating profile and confinement properties.

In order to treat self-consistent simulations in which large amplitude AE are currently obtained, it is first necessary to introduce into the current model the relevant AE damping mechanisms arising from the bulk plasma and as discussed in §2.2.1. Further dissipative effects, such as energetic particle sources and sinks, may also be incorporated into the Hamiltonian code through the additional freedom contained within the δf formalism's use of time-dependent weighting factors for each of the macro-particles, or markers.

Whilst the model developed in this thesis has been specifically devised to examine the nonlinear interaction of fast particles with AE in tokamaks, it could also be modified to describe perturbations to the fast particle distribution arising from other sources. Such effects that could be considered include other low-frequency ($\omega \ll \omega_{ci}$) wave phenomena, as well as kinetic effects such as particle collisions. Due to the use of a δf formalism, it is in principle possible to develop a Fokker-Planck-like code based upon the Monte-Carlo model developed in this thesis with significantly reduced noise levels.

Bibliography

[1] J. D. Lawson, *Proc. Roy. Soc. B*, **70** 6 (1958)

[2] L. A. Artsimovitch, Nuclear Fusion **12**, 215 (1972)

[3] J. A. Wesson, *Tokamaks,* Oxford University Press, 1987

[4] A. B. Mīkhaĭlovskii, Sov. Phys. JETP **41**, 890 (1975)

[5] M. N. Rosenbluth and P. H. Rutherford, Phys. Rev. Lett. **34**, 1428 (1975)

[6] C. Z. Cheng, Liu Chen and M. S. Chance, Ann. Phys. **161**, 21 (1985)

[7] C. Z. Cheng and M. S. Chance, Phys. Fluids **29**, 3695 (1986)

[8] W. W. Heidbrink et al., Nuclear Fusion **31**, 1635 (1991)

[9] K. L. Wong et al., Phys. Rev. Lett. **66**, 1874 (1991)

[10] R. Nazikian et al, submitted to Phys. Rev. Lett. (1996)

[11] H. H. Duong et al., Nuclear Fusion **33**, 749 (1993)

[12] R. B. White, E. Fredrickson, D. Darrow, M. Zarnstorff, R. Wilson, S. Zweben, K. Hill, Yang Chen and Guoyong Fu, Phys. Plasmas **2**, 2871 (1995)

[13] H. Alfvén, Ark. Mat. Astron. Fys. **27A**, 1 (1940)

[14] G. Y Fu and W. Park, Phys. Rev. Lett. **74**, 1594 (1995)

[15] S. E. Parker and W. W. Lee, Phys. Fluids B **5**, 77 (1993)

[16] R. D. Denton and M. Kotschenreuther, J.Comp.Phys 119, 283 (1995)

[17] M. R. O'Brien, M. Cox, C. A. Gardner and F. S. Zaitsev, Nucl. Fusion **35**, 1537 (1995)

[18] F. S. Zaitsev, M. R. O'Brien and M. Cox, Phys. Fluids B **5**, 509 (1993)

[19] C. Z. Cheng et al., Proc. 16 IAEA Conf., IAEA/CN/64/FP-23 (1996)

[20] I. B. Bernstein, E. A. Frieman, M. D. Kruskal R. M. Kulsrud, *Proc. Roy. Soc. (London)* **A244**, 17 (1958)

[21] A. V. Timofeev, Theory of Alfvén Oscillations of the Inhomogeneous Plasma. In: Rev. Plasma Physics, V.9, Consultants Bureau, (1965)

[22] J. Tataronis and W. Grossman, Z. Physik **261**, 203 (1973)

[23] K. Appert, R. Gruber, F. Troyon and J. Vaclavik, Plasma Physics, Vol. 24, No. 9, 1982

[24] D. W. Ross, G. L. Chen and S. M. Mahajan, Phys. Fluids **25**, (4) (1982)

[25] A. Hasegawa and L. Chen, Phys. Fluids, Vol 19, No. 12, 1924 (1976)

[26] G. Y. Fu and J. W. Van Dam, Phys. Fluids B **1** (10), 1949 (1989)

[27] G. Y. Fu and J. W. Van Dam, Phys. Fluids B, **1** (12), 2404 (1989)

[28] H. L. Berk, J. W. Van Dam, Z. Guo and D. M. Lindberg, Phys. Fluids **B4**, 1806 (1992)

[29] F. Zonca and L. Chen, Phys. Rev. Lett. **68**, 592 (1992)

[30] M. N. Rosenbluth, H. L. Berk, J. W. Van Dam and D. M. Lindberg, Phys. Rev. Lett. **68**, 596 (1996)

[31] A. B. Mikhailovskii and I. G. Shukhman, Sov. Phys. JETP. **44**, 952 (1976)

[32] R. Betti and J. P. Freidberg, Phys. Fluids **B4**, 1465 (1992)

[33] J. W. Connor, R. O. Dendy, R. J. Hastie, D. Borba, G. T. A. Huysmans, W. Kerner and S. Sharapov, Proceedings of XXI EPS Conf. on Contr. Fus. Plasma Phys., **18B**, Part III, 616, (1994)

[34] J. Candy, to be published in Plasma Phys. Contr. Fus. (1996)

[35] N. N. Gorelenkov and S. E. Sharapov, Physica Scripta, **45**, 163 (1992)

[36] R. Mett and S. M. Mahajan, Phys. Fluids **B4**, 2885 (1992)

[37] H. L. Berk, R. R. Mett, D. M. Lindberg, Phys. Fluids **B5**, 3969 (1993)

[38] J. Candy and M. N. Rosenbluth, Phys. Plasmas **1**, 356 (1994)

[39] B. N. Breizman and S. E. Sharapov, Plasma Phys. Contr. Fusion, **37**, 1057 (1995)

[40] H. L. Berk, B. N. Breizman and M. Pekker, Phys. of Plasmas **2**, 8 (1995)

[41] H. L. Berk, B. N. Breizman and M. Pekker, Simulation of Alfvén Wave-Resonant Particle Interaction, to be published.

[42] Yanlin Wu, Roscoe B. White, Yang Chen and M. N. Rosenbluth, Phys. Plasmas **2**, 4555 (1995)

[43] H. L. Berk, B. N. Breizman and H. Ye, Phys. Letters **162A**, 475 (1992)

[44] M. D. Kruskal and R. M. Kulsrud, Phys. Fluids **1**, 265 (1958)

[45] J. P. Freidberg, *Ideal Magnetohydrodynamics*, Plenum Press, 1987

[46] G. Bateman, *MHD Instabilities*, The MIT Press, 1980

[47] S. Hamada, Nucl. Fusion **2**, 23 (1962)

[48] G. T. A. Huysmans, J. P. Goedbloed and W. Kerner, Proc. CP90 Conf. Comp. Phys. 1990

[49] W. Kerner, S. Poedts, J. P. Goedbloed, G. T. A. Huysmans, B. Keegan and E. Schwarz, Proc. 18th European Conference on Controlled Fusion and Plasma Physics, Berlin (1991), Part IV, p.89–93

[50] A. H. Boozer, Phys. Fluids **24**, 1999 (1981)

[51] J. D. Jackson, *Classical Electrodynamics*, John Wiley & Sons, 1962

[52] H. Goldstein, *Classical Mechanics*, Second Edition, Addison-Wesley Publishing Company, 1980

[53] A. I. Morozov and L. S. Solov'ev, *Reviews of Plasma Physics 2*, Consultants Bureau, 1966

[54] R. B. White and M. S. Chance, Phys. Fluids **27**, 2455 (1984)

[55] D. T. Sigmar, C. T. Hsu, R. B. White and C. Z. Cheng, Phys. Fluids **B4**, 1506 (1992)

[56] R. G. Littlejohn, J. Plasma Phys. **29**, 111 (1983)

[57] A. H. Boozer, Phys. Fluids **26**, 5 (1983)

[58] Z. Yoshida, Phys. Fluids **1**, 1 (1994)

[59] J. M. Greene, Commun. Pure Appl. Math **36**, 537 (1983)

[60] J. B. Taylor, Phys. Fluids **7**, 767 (1964)

[61] R. B. White, A. H. Boozer and R. Hay, Phys. Fluids **25**, (3) (1982)

[62] R. B. White, Phys. Fluids **2**, (4) (1990)

[63] Landau & Lifshitz, *The Classical Theory of Fields*, Pergamon Press, (1975)

[64] W. W. Lee, J. Comput. Phys, **72**, 243 (1987)

[65] J. Denavit and J. M. Walsh, Plasma Phys. Contr. Fusion, 1981, Vol.6, No.6 pp. 209–223.

[66] A. M. Dimits and W. W. Lee, J. Comput. Phys. 107, 309 (1993)

[67] T. Tajima and F. W. Perkins, Sherwood Theory Meeting, 1983, Paper 2P9 (unpublished)

[68] J. Candy, Submitted to J. Comput. Phys, (JET Preprint JET-P(95) 56)

[69] G. Hu and J. A. Krommes, Phys. Plasmas **1**, 863 (1994)

[70] J. H. Halton, Numer. Math. **2** (1960), 84–90 and 196.

[71] H. Neunzert and J. Wick, "The Convergence of Simulation Methods in Plasma Physics," Proceedings of the Oberwolfach Conference on Mathematical Methods of Plasma Physics, *Methoden und Verfahren der mathematischen Physik* (Verlag Peter Lang, 1980). Vol. 20, pp. 272–286.

[72] J. Candy, to be submitted to J. Comput. Phys.

[73] D. Borba, J. Candy, W. Kerner and S. E. Sharapov, Proceed. Inter. Workshop on Fusion Theory, Varenna, (1996) (JET Preprint JET-P(96) 35)

[74] J. D. Gaffey, J. Plasma Phys. **16**, 149 (1976)

[75] Proc. Plasma Phys. Workshop on Plasma Theory, Varenna, August 1996

[76] L. C. Appel, S. D. Pinches et al., Nucl. Fusion **35**, 1697 (1995)

[77] W. Kerner et al., JET preprint, JET-P(93)100

[78] H. L. Berk, B. N. Breizman and H. Ye, Phys. Fluids **B5**, 1506 (1993)

[79] H. L. Berk, B. N. Breizman and M. S. Pekker, Phys. Rev. Lett. **76**, 1256 (1996)

[80] H. L. Berk, B. N. Breizman, J. Fitzpatrick and H. V. Wong, Line-Broadened Quasi-linear Burst Model, Preprint IFSR-712 (1995)

[81] G. Vlad, C. Kar, F. Zonca and F. Romanelli, Phys. Plasmas **2**, 418 (1995)

[82] D. A. Spong, B. A. Carreras and C. L. Hedrick, Phys. Plasmas **1**, 1503 (1994)

[83] T. S. Hahm and L. Chen, Phys. Rev. Lett. **74**, 266 (1995)

[84] W. Kerner, L. C. Appel, M. Cox, T. C. Hender, G. T. A. Huysmans, M. R. O'Brien, S. D. Pinches, S. E. Sharapov, and F. S. Zaitsev, IAEA Conference, Seville 1994, IAEA-CN-60/D-P-II-4

Publications

I Conference Presentations

'Nonlinear interaction of Alfvén waves with fast particles' (Poster)
Pinches S. D., Candy J., Sharapov S. E., Appel L. C., Breizman B. N., Hender T. C., Hopcraft K. I., Huysmans G. T. A., Kerner W.
1996 International Sherwood Fusion Theory Conference.

'Nonlinear interaction of Alfvén waves with fast particles' (Oral)
Pinches S. D., Candy J., Sharapov S. E., Appel L. C., Breizman B. N., Hender T. C., Hopcraft K. I., Huysmans G. T. A., Kerner W.
23rd IOP Annual Plasma Physics Conference (1996)

'Fast Particle Transport due to Alfvén Instabilities in Tokamaks' (Oral)
Pinches S. D., et. al.
22nd IOP Annual Conference on Plasma Physics (1995)

II Other Publications

'Alfvén eigenmodes and fast particle physics in JET reactor relevant plasmas'
JET team et. al. (presented by D. Start)
IAEA-CN-64/A2-6, IAEA Conference, Montreal 1996.

'Redistribution of Fast Ions by the Sawtooth Crash'
Appel L. C., Hender T. C., Pinches S. D., et al.
Plasma Physics Workshop on Plasma Theory, Verena, August 1996

'Alfvén eigenmode induced energetic particle transport in JET'
Appel L. C., Berk H. L., Borba D., Breizman B., Hender T. C., Huysmans G. T. A., Kerner W., Pekker M., Pinches S. D., Shaparov S. E.
Nuclear Fusion, **35** p.1697 (1995)

'Fast Ion Transport Arising From TAE modes in JET'
Appel L. C., Hender T. C., Pinches S. D., et al.
The 6th European Fusion Theory Conference, Utrecht, The Netherlands, October 1995.

'TAE-induced diffusion of fast particles in JET'
Appel L. C., Berk H. L., Borba D., Breizman B., Eriksson L. G., Fasoli A., Hender T. C., Huysmans G., Kerner W., Monticelli E., Pekker M., Pinches S. D., Sharapov S.
22nd European Physical Society Conference on Controlled Fusion and Plasma Physics, Bournemouth, 3rd-7th July 1995, Contributed papers. Part 2. p.261.

'Alfvén Eigenmode Induced Energetic Particle Losses in JET'
Appel L. C., Hender T. C., Kerner W., Pinches S. D., et al. (Presented by W. Kerner)
4th IAEA Workshop on Alpha-Particles in Fusion Research, PPPL, April 25-28, 1995

'Fast particle losses due to TAE-modes in JET'
Sharapov S., Appel L. C., Borba D., Hender T. C., Huysmans G. T. A., Kerner W., Pinches S. D.
Bulletin of the American Physical Society, vol.39 no.7 November 1994 (Abstracts of the Thirty-Sixth Annual Meeting of the Division of Plasma Physics, 7-11 November 1994, Minneapolis). p.1566.

'Alfvén Eigenmodes and Alpha-Particle Losses in JET'
W. Kerner, L. .C. Appel, M. Cox, T. C. Hender, G. T. A. Huysmans, M. R. O'Brien, S. D. Pinches, S. E. Sharapov, and F. S. Zaitsev.
IAEA Conference, Seville 1994, IAEA-CN-60/D-P-II-4

Glossary

I Greek Symbols

$\tilde{\alpha}$	Perturbation parameter, $A_{\|\|} = \alpha B_0$
β	Plasma beta (Ratio of particle energy density to magnetic energy density)
δ	Covariant ψ_p component of $\mathbf{B}$
$\mathcal{E}_j$	Energy of jth particle
ε_0	Permittivity
ε	Inverse aspect ratio, $\varepsilon = a/R_0$
η	Resistivity
γ	Adiabaticity index
γ_L	Linear growth rate of instability $A_k \sim e^{\gamma_L t}$
$\Gamma^{(c)}$	Canonical phase-space
$\Gamma^{(p)}$	Physical phase-space
λ	Cosine of the pitch angle, $\lambda = \cos\theta_v = v_{\|\|}/v$
Λ	Normalised pitch angle, $\Lambda = \mu B_0/\mathcal{E}$
μ_j	Magnetic moment of jth particle
μ_0	Permeability
$\tilde{\Phi}$	Scalar potential
φ	Geometric toroidal angle
ρ	Plasma mass density
ρ_c	Canonical variable used in guiding centre description
ρ_i	Larmor radius
$\rho_{\|\|}$	Useful guiding centre variable, $\rho_{\|\|} = v_{\|\|}/B$
ψ	Toroidal flux which acts like a radial variable
ψ_p	Poloidal flux which acts like a radial variable
$\psi_p(a)$	Poloidal flux at edge of plasma
$\hat{\psi}_p$	Normalized poloidal flux, $\hat{\psi}_p = \psi_p/\overline{\psi}_p$
σ_k	Phase of kth wave
θ	Poloidal coordinate
θ_v	Pitch angle, see Fig. 3.3
ω_{ce}	Electron cyclotron frequency
ω_{ci}	Ion cyclotron frequency

ω_k	Angular frequency of kth wave
$\boldsymbol{\xi}$	Fluid displacement
ξ_j	Gyro-phase of jth particle
ζ	Toroidal coordinate

II Roman Symbols

a	Minor radius at edge of plasma
A_k	Amplitude of kth wave
$\mathbf{A}$	Vector potential
$\mathbf{A}^*$	Modified vector potential
B	Magnetic field strength (Magnetic inductance)
$\mathbf{B}$	Magnetic field vector
$\hat{\mathbf{B}}$	Unit vector in direction of $\mathbf{B}$
$d\Gamma^{(c)}$	Infinitesimal volume element of canonical phase-space
$\Delta\Gamma_j^{(c)}$	Finite volume element of canonical phase-space associated with jth fast particle
$d\Gamma^{(p)}$	Infinitesimal volume element of physical phase-space
$\Delta\Gamma_j^{(p)}$	Finite volume element of physical phase-space associated with jth fast particle
$d\mathcal{U}$	Infinitesimal volume element of uniformly loaded phase-space
$\Delta\mathcal{U}_j$	Finite volume element of uniformly loaded phase-space associated with jth fast particle
e	Charge of fast particle
E	Electric field strength
$\mathbf{E}$	Electric field vector
$\mathcal{E}_j$	Energy of jth particle
E_k	Wave energy of kth wave
g^{ij}	Metric tensor element
g	Covariant ζ component of $\mathbf{B}$
$\mathcal{H}$	Hamiltonian
I	Covariant θ component of $\mathbf{B}$
$\mathbf{j}$	Current density
$\mathcal{J}$	Jacobian
$\mathbf{k}$	Wave Vector
$\mathcal{L}$	Lagrangian
m	Poloidal mode number/Mass of fast particle
n_e	Electron number density
n_i	Ion number density
n_k	Toroidal mode number of kth wave
n_p	Number of markers
n_w	Number of waves

P	Plasma pressure
q	Safety factor
R	Major radius
R_0	Major radius at geometric axis of tokamak
R_{mag}	Major radius at magnetic axis
s	Normalized radial variable, $s = \sqrt{\psi_p/\overline{\psi}_p}$
$\mathcal{U}$	Uniformly loaded phase-space
v_A	Alfvén speed
$v_{\|\|}$	Component of fast particle velocity parallel to magnetic field
$\mathcal{X}_k$	Real part of complex wave amplitude for kth wave
$\mathcal{Y}_k$	Imaginary part of complex wave amplitude for kth wave
Z	Vertical distance from mid-plane/Charge in units of electron charge

III Acronyms

AE	Alfvén Eigenmode
DIII-D	Doublet III-D (San Diego, USA)
EAE	Ellipticity induced Alfv'en Eigenmode
FLR	Finite Larmor Radius
HAGIS	Hamiltonian Guiding Centre System
ICRH	Ion Cyclotron Resonance Heating
ITER	International Thermonuclear Experimental Reactor
JET	Joint European Torus (Culham, UK)
KAW	Kinetic Alfvén Wave
KTAE	Kinetic TAE
MHD	Magnetohydrodynamics
NBI	Neutral Beam Injection
START	Small Tight Aspect Ratio Tokamak (Culham, UK)
TAE	Toroidicity Induced Alfvén Eigenmode
TFTR	Tokamak Fusion Test Reactor (Princeton, USA)
ZOW	Zero Orbit Width